Title
Radiation Transfer through Droplet-Covered Substrates: Simulations, Experiments, and Applications

Author
Simsek Turan, Eylul

Publication Date
2021

Peer reviewed|Thesis/dissertation

UNIVERSITY OF CALIFORNIA
Los Angeles

Radiation Transfer through Droplet-Covered Substrates: Simulations, Experiments, and Applications

A dissertation submitted in partial satisfaction
of the requirements for the degree
Doctor of Philosophy in Mechanical Engineering

by

Eylul Simsek Turan

2021

ABSTRACT OF THE DISSERTATION

Radiation Transfer through Droplet-Covered Substrates: Simulations, Experiments, and Applications

by Eylul Simsek Turan

Doctor of Philosophy in Mechanical Engineering

University of California, Los Angeles, 2021

Professor Laurent G. Pilon, Chair

Water droplets are commonly observed on the inner or outer surface of covers of solar energy conversion systems such as greenhouses, solar collectors, and solar stills as a result of dropwise condensation and/or rain. These systems have an operating temperature ranging from 280 K to 320 K and emit infrared thermal radiation while being exposed to solar radiation. The presence of such droplets can reduce the solar transmittance and alter the thermal load on the solar energy conversion systems. In addition, radiative cooling surfaces used for building cooling and water harvesting applications also collect dew and these condensed droplets can alter the emittance and selectivity of radiative cooling surfaces. This dissertation aims (i) to investigate both numerically and experimentally visible and infrared radiation transfer through surfaces supporting polydisperse droplets on their front or back side and (ii) to assess experimentally the effect of droplets in important applications including photovoltaic solar cells and water production using radiative cooling surfaces.

First, light transfer through soda-lime glass windows supporting acrylic droplets on its back side was investigated. For contact angle θ_c smaller than the critical angle θ_{cr} for total internal reflection at the droplet/air interface, the presence of droplets did not significantly affect the transmittance and reflectance. However, for droplet contact angle $\theta_{cr} \leq \theta_c < 90°$, the transmittance

decreased significantly with increasing droplet contact angle and/or surface area coverage while the reflectance increased. Second, infrared radiation transfer through glass windows covered with droplets on their front or back sides was examined. The transmittance of windows with slightly absorbing droplets on the front increased while the reflectance decreased with increasing contact angle and surface coverage due to antireflection effects. For droplets on the back with contact angles larger than the critical angle for total internal reflection at the droplet/air interface, the transmittance decreased with increasing contact angle and surface coverage. For strongly absorbing droplets, the transmittance decreased with increasing surface coverage for droplets on either the front or back sides. Experimental measurements for both visible and infrared parts were in good agreement with numerical predictions obtained using the Monte Carlo ray-tracing method.

Moreover, the effect of droplets on the performance of solar photovoltaic (PV) cells was quantified experimentally. The current vs. voltage curves of polycrystalline silicon solar cells with dry and droplet-covered glass covers were measured under simulated solar irradiation under different incidence angles. For incident angles $\theta_i \leq 30°$, the droplets did not affect the performance of the PV cells. However, for incident angles $\theta_i > 30°$, the presence of droplets caused the maximum power and energy conversion efficiency of the PV cells to decrease significantly. Such performance degradation was attributed to the fact that the incident light was back-scattered through the droplets instead of being trapped by total internal reflection at the cover/air interface.

Finally, the effect of droplets on the emittance and selectivity of radiative cooling surfaces was investigated experimentally. The spectral directional-hemispherical reflectance of a moderately selective emitter supporting acrylic droplets with different contact angles and surface area coverages was measured. The spectral emittance of the radiative cooling surfaces was found to increase significantly across the infrared spectrum in presence of droplets and with increasing

surface area coverage. In fact, the droplets transformed the spectrally selective surface into a broadband emitter. This was attributed to the absorption by the acrylic droplets. In addition, outdoor nighttime experiments under different relative humidity and cloud coverage established that the temperature of the radiative cooling surface increased when covered by droplets due to the increase in the radiative heat gain from the atmosphere.

The dissertation of Eylul Simsek Turan is approved.

Vijay Dhir

Adrienne S. Lavine

Vasilios Manousiouthakis

Laurent G. Pilon, Committee Chair

University of California, Los Angeles

2021

This dissertation is dedicated to my husband, Deniz Turan.

TABLE OF CONTENT

LIST OF SYMBOLS

A	area (m^2)
a	coverage factor
d	droplet diameter (μm)
d_p	projected droplet diameter (μm)
$E_{b,\lambda}$	blackbody spectral emissive power ($W/m^2 \cdot \mu m$)
f	frequency (-)
f_A	droplet surface area coverage (%)
G_s	solar irradiation (W/m^2)
$G_{s,\lambda}$	spectral solar spectral irradiance ($W/m^2 \cdot \mu m$)
H	glass thickness (mm)
i	current (mA)
I	radiation incident intensity ($W/m^2 \cdot sr$)
k	absorption index
L	glass length (mm)
l_c	capillary length (mm)
m	complex index of refraction, $m = n + ik$
n	refractive index
N	number
P_h	hourly electrical energy production rate (W/m^2)
P_{max}	maximum power (mW)
R	reflectance (%)
R_p	reflectivity of the interface for p-polarized light
R_s	reflectivity of the interface for s-polarized light
RH	relative humidity (%)
r_c	radius of curvature
S_C	total radiation flux (kW/m^2)
t	time (hr)

T	temperature (K)
T_{nh}	normal-hemispherical transmittance
T_{nn}	normal-normal transmittance
T_a	air temperature (K)
T_c	solar cell temperature (K)
T_{dew}	dew point temperature (K)
T_o	sample temperature (K)
T_{sol}	solar transmittance (%)
u	standard uncertainty (% or °)
u_w	wind velocity (m/s)
U	expanded uncertainty (% or °)
V	voltage (V)
W	glass width (mm)
x	x coordinate of droplet center (mm)
y	y coordinate of droplet center (mm)

Greek symbols

α	absorptance
δ	sum of the relative errors
ε	total hemispherical emissivity/emittance
ε_d	total directional emissivity/emittance
ε_n	total normal emissivity/emittance
η	solar cell energy conversion efficiency (%)
θ_B	Brewster angle (°)
θ_c	droplet contact angle (°)
θ_{cr}	critical angle for the droplet/air interface (°)
θ_i	incident angle (°)
θ_r	reflection angle (°)
θ_T	tilt angle (°)
θ_t	transmission angle (°)

θ_z solar zenith angle (°)

κ absorption coefficient (1/m)

λ wavelength (nm)

ρ interface reflectivity

σ standard deviation

Subscription

a refers to air

ac refers to air/solar cell interface

ag refers to the air/glass interface

c refers to solar cell

com refers to combined

d refers to droplet

dh refers to directional-hemispherical

g refers to glass

ga refers to glass/air interface

gd refers to glass/droplet interface

gc refers to glass/solar cell interface

i refers to instrumentation

LWIR refers to long-wavelength infrared

nh refers to normal-hemispherical

nn refers to normal-normal

r refers to ratio

s refers to slab

w refers to glass pane of window

λ refers to spectral variables

* refers to the theoretical prediction

LIST OF FIGURES

LIST OF TABLES

ACKNOWLEDGEMENTS

Firstly, I would like to thank my advisor, Prof. Laurent Pilon, for his mentorship throughout my Ph.D. study. His guidance, motivation, and excitement helped me to complete my doctoral work. Secondly, I would like to thank my Ph.D. committee members Prof. Vijay Dhir, Prof. Adrienne S. Lavine, and Prof. Vasilios Manousiouthakis for serving on my thesis committee. I would also like to thank Prof. Aaswath Pattabhi Raman and Dr. Jyotirmoy Mandal for providing radiative cooling materials that I used throughout my research work and for their insightful comments.

I would also like to acknowledge all my current and former lab members Dr. Tiphaine Galy, Jack Hoeniges, Sara Vallejo-Castano, Sun Woong Baek, Dr. Michal Marszewski, Megan Williams, Matevž Frajnkovič, Ali Dashti, Dr. Ampol Likitchatchawankun, Dr. Obaidallah Mohammad Munteshari, and Dr. Bing-Ang Mei. I am so thankful for their support. I would like to thank my husband, Deniz Turan for his patience and unconditional support. Finally, I am grateful to my family Selma Simsek, Yildirim Simsek, Gursevil Turan, and Rasit Turan for their patience, support, and guidance throughout my Ph.D. study.

This material is based upon work supported, in part, by The Scientific and Technological Research Council of Turkey (TÜBİTAK).

VITA

2009 – 2013 B.Sc. in Mechanical Engineering, Middle East Technical University, Ankara.

2013 – 2016 M.Sc. in Mechanical Engineering, Middle East Technical University, Ankara.

2016 – 2021 Graduate Student in Mechanical and Aerospace Engineering, University of California – Los Angeles.

PUBLICATIONS

E. Simsek, S. Coskun, T. Okutucu-Ozyurt, and H. E. Unalan, Heat transfer enhancement by silver nanowire suspensions in microchannel heat sinks, *International Journal of Thermal Sciences*, 123, pp. 1-13 (2018).

E. Simsek, K. Zhu, G. N. Kashanchi, M. J. Williams, T. Galy, M. Marszewski, S. H. Tolbert, and L. Pilon, Light transfer through semi-transparent glass panes supporting pendant droplets, *Journal of Quantitative Spectroscopy and Radiative Transfer*, 261, 107493 (2021).

E. Simsek, M. J. Williams, and L. Pilon, Effect of dew and rain on photovoltaic solar cell performances, *Solar Energy Materials and Solar Cells*, 222, 110908 (2021).

J. Hoeniges, K. Zhu, W. Welch, **E. Simsek**, and L. Pilon, Transmittance of transparent horizontal and tilted windows supporting large non-absorbing pendant droplets, *Journal of Quantitative Spectroscopy and Radiative Transfer*, 275, 107876 (2021).

F. Huisman, **E. Simsek**, T. Galy, F. Saaman, and L. Pilon, Reversible sequin fabric as variable emittance surfaces, *International Journal of Heat and Mass Transfer*, 183, 122167 (2022).

E. Simsek, M. J. Williams, J. Hoeniges, K. Zhu, and L. Pilon, Infrared radiation transfer through semitransparent windows supporting absorbing droplets, *Journal of Quantitative Spectroscopy and Radiative Transfer* (under review).

E. Simsek, J. Mandal, A. P. Raman, and L. Pilon, Dropwise Condensation enhances emittance and reduces selectivity of radiative cooling surfaces, *in preparation*.

Chapter 1: Introduction

1.1 Presence of droplets on surfaces

Water droplets are often observed on the inner or outer surface of covers of solar water heaters [1,2], solar collectors [3], greenhouses [4–9], outdoor photobioreactors [10–12], covered raceway ponds [13], and building windows [14–17] as a result of dropwise condensation and/or rain. For example, Figures 1.1(a) and 1.1(b) show condensed water droplets on the surface of a greenhouse cover and a window. In addition, dropwise condensation occurs in various solar energy conversion systems such as solar stills [18–23], as illustrated in Figure 1.1(c).

Moreover, photovoltaic (PV) solar cells can convert the incident solar radiation directly into electricity for photons with energy larger than the bandgap of the semiconductor (e.g., silicon) used to form PN junctions [24]. Solar PV technology provided 592 TWh of electrical energy worldwide in 2018 and is expected to deliver about 4,700 TWh by 2040 representing 13% of the projected global energy consumption [25]. Photovoltaic solar cells can be classified as (1) crystalline silicon-based solar cells with efficiency up to 27.6%, (2) thin-film solar cells with efficiency up to 23.4%, (3) emerging solar cells such as dye-sensitized, perovskite, quantum dot, and organic solar cells with an efficiency of up to 25.2%, and (4) multijunction solar cells with efficiency up to 39.2% [26]. Among these different types, crystalline silicon-based solar cells (monocrystalline and polycrystalline) have the highest market share representing more than 90%. In general, water droplets are observed at the surface of outdoor PV solar panels as they are exposed to outdoor elements such as rain and/or dew [27–29], as illustrated in Figure 1.1(d).

Figure 1.1. Water droplets on the surface of (a) a greenhouse (Credit: Photograph reproduced with permission from http://www.MikeSavad.com), (b) a window, of (c) a solar still (Photo by Deris Jeannette, ClearDome Solar Thermal), and (d) a solar photovoltaic panel (credit: photograph reproduced with permission from GÜNAM, http://gunam.metu.edu.tr/).

Furthermore, passive radiative cooling refers to the net radiative heat loss from a radiatively selective surface to space and to the upper atmosphere primarily through the long-wavelength infrared (LWIR) transmission window of the atmosphere spanning wavelengths between 8 and 13 μm. It offers a “zero-energy” and “zero-carbon” way to cool terrestrial objects [30,31]. Such

passive net cooling effect is explored as a potential solution to cooling needs at scales ranging from complementing or replacing air-conditioning in the built environment [32,33] to geoengineering in order to address climate change [34]. One of the major applications of radiative cooling is the cooling of buildings [35–37], particularly rooftops, which can radiatively cool down to low temperatures for its advantageous view factor with the sky. Then, rooftop radiative cooling surface tend to collect dew at night, even in relatively arid regions [38]. Indeed, water droplets are commonly observed condensing on a radiative cooling surface as its temperature drops below the dew point temperature of the surrounding air, as illustrated in Figure 1.2. In fact, radiative cooling surfaces can also be used for harvesting atmospheric water by condensing atmospheric water vapor or fog [39–42].

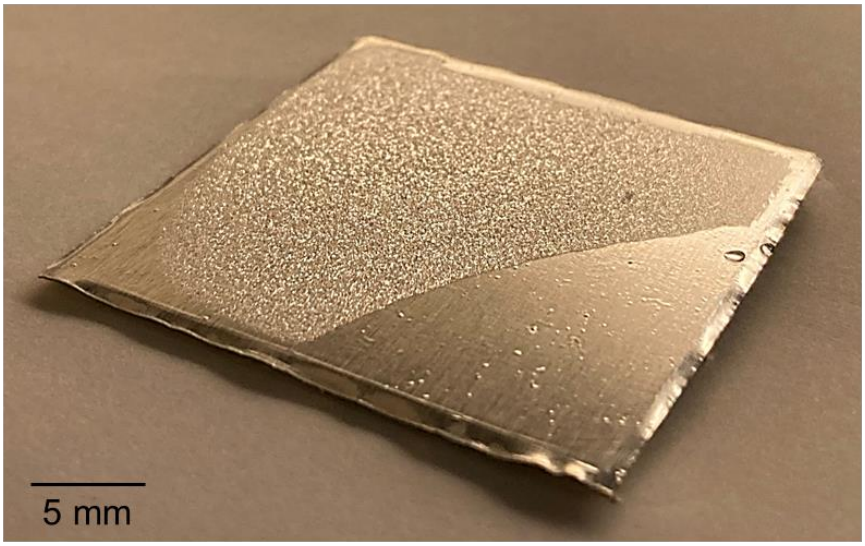

Figure 1.2. Example of condensate water droplets on the radiative cooling surface.

1.2 Dew formation and droplet characterization

Dew formation refers to water vapor condensing on a surface at a temperature below the dew point temperature of the surrounding air or even above due to (i) the presence of hygroscopic dust on the covers [39] and/or (ii) capillary effects [40]. Two main requirements for dew formation include

(i) sufficient vapor amount in the surrounding air and (ii) intensive radiative cooling of the surface [41]. Water droplets can be frequently present on surfaces due to dropwise condensation, even in arid and semi-arid environments [38,42]. For example, in semi-arid coastal regions such as in the province of Almería in southeast Spain dew forms more than 75% of the nights [43]. Also, dew formation has been shown to occur 15% to 95% of the nights in the grasslands of the United States and last for hours under high relative humidity [44]. Dew commonly forms on the surfaces in the night and/or early in the morning [41,44] and dew duration could reach 6–15 hours [44]. For example, the presence of dew in daytime and nighttime was up to 7 hours and 10 hours in the desert-shrub ecosystem of northwestern China, respectively [45].

Discrete droplets form on the surfaces and may grow and coalesce as condensation continues [46], as shown in Figure 1.3. These droplets are characterized by their (i) contact angle θ_c, (ii) projected surface area coverage f_A, (iii) size distribution, and (iv) shape.

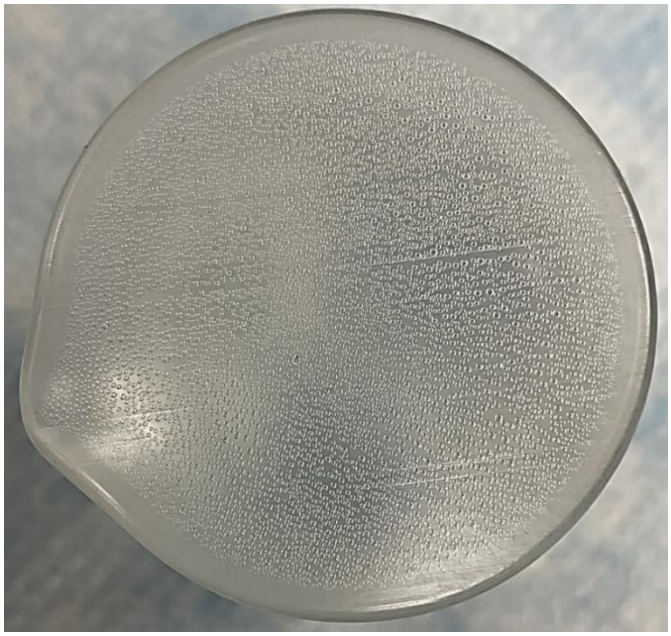

Figure 1.3. Example of water droplets condensed on a plastic cover.

The droplet contact angle is defined as the angle between the tangents at the interface of the liquid droplet and of the solid substrate [38], as illustrated in Figure 1.4(a). Considering the contact angle of a water droplet θ_c, solid surfaces can be classified as (i) superhydrophilic for $\theta_c = 0°$, (ii) hydrophilic for $\theta_c < 90°$, (iii) hydrophobic for $90° \leq \theta_c \leq 150°$, and (iv) superhydrophobic for $\theta_c > 120°$ [47]. Different coatings and micro/nanostructures can be deposited or formed on the surfaces to achieve hydrophilicity preferable for antifogging behavior [48–50] or hydrophobic surfaces for self-cleaning attributes [49].

The droplet projected surface area coverage f_A can be defined as the ratio of the projected surface area occupied by the droplets to the surface area of the solid surface [51]. For dropwise condensation on a vertical and horizontal oriented surface, equilibrium droplet surface area coverage f_A was reported as 55% [52] and 60% [51], respectively.

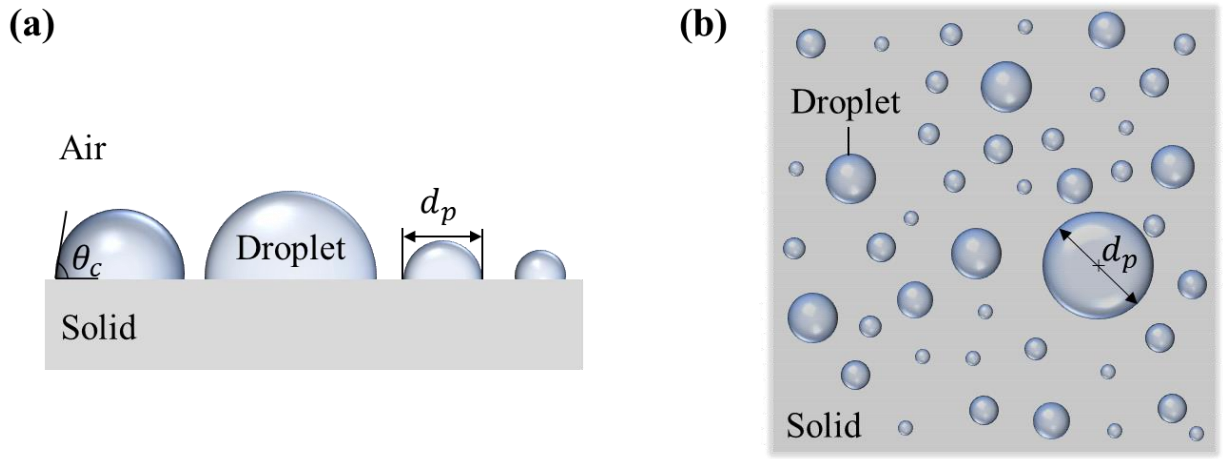

Figure 1.4. Schematic of a solid substrate supporting droplets (a) front view, (b) top view.

Typically, the diameter of the droplets ranges from a few micrometers to millimeters [53,54]. Droplet size distribution can be *monodisperse* where droplets had the same projected droplet diameter d_p or *polydisperse* where droplets had a size distribution. For a dropwise condensation on a solid surface, droplets are *polydisperse* and randomly distributed [55], as illustrated

schematically in Figure 1.4. The droplets are cap-shaped when the surface tension forces are dominant such that the droplet diameter is much smaller than the capillary length l_c [56], as shown in Figure 1.4(a). However, droplets with a diameter equal to or larger than the capillary length l_c are non-cap shaped as they become deformed by gravity [56].

1.3 Motivation of the present study

The presence of water droplets has been shown to reduce the transmittance through the plastic covers or windows in the visible and near-infrared parts of the electromagnetic spectrum thereby decreasing the solar energy input available for photosynthesis [13,57–61] or for solar photothermal and photoelectric energy conversions [62–64]. This has been attributed to back-scattering and/or absorption by droplets [52,55,64–66]. In addition, these solar energy conversion systems have an operating temperature ranging from 280 K to 320 K and emit thermal radiation at infrared wavelengths ($4\ \mu m \leq \lambda \leq 40\ \mu m$) with a peak emissive power occurring around 10 μm while being exposed, during the day, to solar radiation concentrated in the spectral range $400\ nm \leq \lambda \leq 3\ \mu m$ [46]. The presence of droplets on either side of the window or cover can alter the transmission of solar radiation and the emissivity of the covers and windows, thereby impacting the energy input and the thermal load on the systems. However, systematic characterization of the droplets is made difficult by the dynamic nature of the condensation process and the outdoor conditions. As an alternative, numerical simulations have been performed to predict the radiation transmittance through the droplet-covered windows [55,64,67]. Nonetheless, the experimental validation of these complex numerical simulations in the visible and infrared parts of the electromagnetic spectrum has not been reported in the literature. In addition, to the best of our knowledge, the impact of droplets on infrared radiation transfer through windows has not yet been investigated thoroughly.

Similarly, the presence of water droplets on the radiative cooling surfaces can alter the emittance of the surfaces and the performance of the radiative cooler. Understanding the effect of droplets on the radiative cooling surfaces' performance can provide information to optimize the design of these radiative emitters for both building cooling and water harvesting applications. The previous studies reported in the literature related to the radiative cooling surfaces have not considered the effect of dropwise condensation on the emittance and on the selectivity of the radiative coolers.

1.4 Objectives of the present study

This dissertation aims first to experimentally and numerically investigate visible and infrared radiation transfer through semitransparent glass windows supporting droplets on their back or front sides. To do so, glass slabs supporting a large number of polydisperse acrylic droplets with different contact angles and projected surface area coverages were prepared and carefully characterized. Acrylic droplets were used instead of water to avoid changes in the droplet size distribution and surface area coverage during the measurements due to evaporation, coalescence, break-off, and/or droplet motion. The normal-hemispherical transmittance and reflectance of each sample was measured in the visible and infrared part of the electromagnetic spectrum. The experimental measurements were used to validate the previously developed numerical code based on the Monte Carlo ray-tracing method [55,64,66].

This dissertation aims also to investigate experimentally the effect of the presence of droplets in different important applications in energy generation and water production. First, the effect of droplet surface coverage and contact angle on the performance of photovoltaic solar cells were investigated experimentally under simulated collimated solar radiation for a wide range of incident angles. To do so, bare polycrystalline silicon solar cells with different glass covers supporting

droplets with various contact angles and surface area coverage were tested. Second, infrared radiation emission from selective emitters covered with droplets on their front side was investigated experimentally. To do so, a moderately selective emitter recently proposed as a radiative cooling standard [68] supporting a large number of polydisperse acrylic droplets with different droplet contact angles and surface area coverages were prepared and characterized. The spectral directional-hemispherical reflectance of the samples was measured in the infrared part of the electromagnetic spectrum. Then, the total directional emittance, directional emittance inside and outside the atmospheric transparency window of the dry and droplet-covered samples were calculated. Finally, outdoor nighttime experiments were conducted to compare the temperature of the dry and droplet-covered radiative cooling surfaces.

1.5 Organization of the document

Chapter 2 assesses the effect of the pendant droplets condensed on the back side of semi-transparent glass panes on their normal-hemispherical transmittance and reflectance in the visible and near-infrared parts of the electromagnetic spectrum when droplets and windows are transparent. Chapter 3 extends the investigation of Chapter 2 to the infrared part of the spectrum when cover and droplets are semitransparent. Here, infrared radiation transfer through semitransparent glass windows covered with droplets on the front or back sides is experimentally and numerically investigated. Chapter 4 studies the impact of droplets on the performance and hourly energy production of solar photovoltaic cells due to dropwise condensation or rain falling on their cover. Chapter 5 experimentally investigates the effect of dropwise condensation on the emittance and selectivity of the radiative cooling surfaces. Finally, Chapter 6 summarizes the contributions of this thesis and provides recommendations for future research. Figure 1.5

summarizes the organization of this dissertation in terms of single effect experiments in the visible or infrared and in terms of applications.

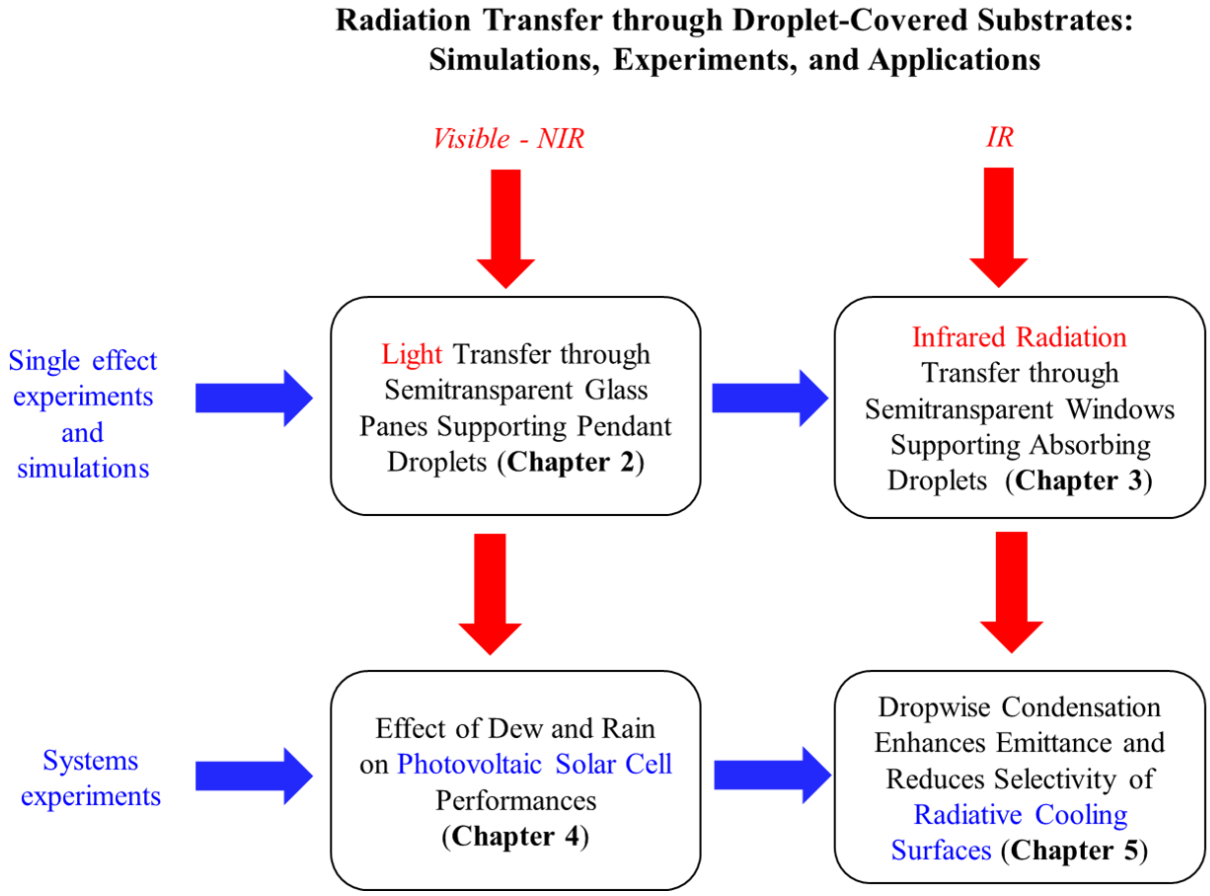

Figure 1.5. Organization of this dissertation.

Chapter 2: Light Transfer through Semitransparent Glass Panes Supporting Pendant Droplets

This chapter demonstrates experimentally the effect of pendant droplets condensed on the back of semi-transparent glass panes on their normal-hemispherical transmittance and reflectance in the visible and near-infrared. To enable sample characterization and ensure repeatability, acrylic droplets were deposited on the back side of 3 mm-thick soda-lime silicate glass slabs with or without hydrophobic surface treatment including perfluorinated silane, perfluorinated silane-coated silica nanoparticle monolayer, or Teflon coatings. The droplet contact angle θ_c was varied between 26° and 76° and the projected surface area coverage reached up to 60%. The results of this chapter can provide guidelines for the design and operation of energy efficient flat-plate solar collectors, outdoor photobioreactors, greenhouses, solar desalination systems, and other solar energy conversion systems.

2.1 Background

2.1.1 Modeling

Tow [67] used the Monte Carlo Ray Tracing (MCRT) method to numerically investigate light transfer through a 3 mm thick non-absorbing glass slab (n_g = 1.5) supporting non-absorbing and ordered cap-shaped water droplets (n_d = 1.33) on its back side. By virtue of symmetry, 1/12 of a cap-shaped droplet on a half-equilateral triangle shaped glass surface was simulated. The droplet contact angle θ_c varied between 0° and 90° while the droplet surface area coverage and diameter were constant and equal to f_A = 55% and d_p = 2.66 mm, respectively. The angle of the collimated incident light varied between 0° and 80°. The directional-hemispherical reflectance was found to decrease slightly in the presence of droplets with contact angles $\theta_c \leq 45°$. However, for contact

angles larger than the critical angle for total internal reflection at the droplet/air interface, the normal-hemispherical reflectance increased significantly with increasing droplet contact angle. This was attributed to the fact that total internal reflection at the droplet/air interface reduced the transmittance through the wet glass. The author also stated the need for experimental measurements to validate the numerical simulations and to assess the use of coatings to adjust the droplet contact angle to minimize reflectance.

More recently, Zhu et al.[55] presented a MCRT method to predict the directional-hemispherical transmittance through a non-absorbing glass pane (n_w = 1.5) supporting between 350 and 800 non-absorbing cap-shaped water droplets (n_d = 1.33) on its back side. Monodisperse or polydisperse droplets either randomly distributed or ordered in a hexagonal pattern on the glass pane surface were investigated. The droplet contact angle θ_c varied between 0° and 180° and the projected surface area f_A between 0 and 90%. The thickness of the glass pane was 3 mm and the angle of the collimated incident light varied between 0° and 90°. The directional-hemispherical transmittance was found to be independent of droplet diameter and spatial distribution, albeit for non-absorbing droplets [66]. However, it depended on (i) the incident angle θ_i, (ii) the droplet contact angle θ_c, and (iii) the surface area coverage f_A. In fact, the directional transmittance decreased monotonously with increasing incident angle. To describe the effect of droplet contact angle θ_c on the normal-hemispherical transmittance, the authors defined four optical regimes with respect to the critical angle θ_{cr} for total internal reflection at the droplet/air interface. In both Regime I ($\theta_c < \theta_{cr}$) and Regime IV ($\theta_c \geq 180° - \theta_{cr}$), the normal-hemispherical transmittance was found to be nearly independent of contact angle as the droplets scatter the photons forward. In Regime II ($\theta_{cr} \leq \theta_c < 90°$), the normal-hemispherical transmittance decreased rapidly and reached a minimum at 90°. This was attributed to the total internal reflection occurring at the droplet/air

interface. A further increase in contact angle between 90° and 180°-θ_{cr} resulted in a rapid increase in the normal-hemispherical transmittance, corresponding to Regime III. In addition, the normal-hemispherical transmittance decreased with increasing surface area coverage in all regimes except Regime I when it slightly increased.

Zhu et al.[66] also predicted the normal-hemispherical transmittance and reflectance of semi-transparent glass pane (n_w = 1.5) supporting a large number of absorbing cap-shaped water droplets (n_d = 1.33) condensed on their back side. The thickness of the pane was 3 mm and its absorption index k_w varied between 0 and $5x10^{-5}$. Monodisperse or polydisperse droplets were distributed either in an ordered hexagonal pattern or randomly on the back side of the pane and featured (i) absorption index k_d ranging between 0 and $5x10^{-2}$, (ii) contact angle θ_c between 0° and 180°, (iii) droplet projected diameter d_p between 50 μm and 250 μm, and (iv) surface area coverage f_A from 30% to 55%. The normal-hemispherical transmittance of glass panes supporting non-absorbing droplets was found to be independent of the droplet spatial distribution. For slightly absorbing droplets ($k_d \leq 5x10^{-2}$), the normal-hemispherical transmittance decreased with increasing droplet diameter and volume by virtue of the fact that absorption is a volumetric phenomenon. In addition, the same four optical regimes defined in Ref.[55] for non-absorbing droplets were also observed for slightly absorbing droplets. However, for strongly absorbing droplets, the normal-hemispherical transmittance decreased sharply with increasing contact angle for $\theta_c < 90°$, while remaining constant and independent of the droplet diameter, contact angle, and absorption index for contact angles $\theta_c \geq 90°$. Finally, while the numerical simulations rely on few and realistic assumptions, they have not been validated experimentally.

2.1.2 Experiments

The effect of water droplets on the transmittance of semi-transparent covers has often been investigated experimentally, under outdoor conditions [7–9,18,22,59,61,69–71]. Cemek et al.[59] measured the total hemispherical transmittance of solar radiation through reduced-scale greenhouses. The greenhouses were covered with a cladding made of a 150-micron thick film of (i) polyethylene (PE), (ii) UV-stabilized polyethylene (UV+PE), (iii) IR absorber polyethylene (IR+PE), or (iv) double-layer polyethylene films (D-Poly). The greenhouses were aligned along the East-West direction in Samsun (42°N), Turkey. The roof of the greenhouses was inclined at an angle of 26° with respect to the horizontal and the sidewalls were vertical. Photographs of the greenhouse roof indicated that the droplet surface area coverage of the roof made of PE, UV+PE, and IR+PE films was 46%, 38%, and 29% with droplet mean diameter of 2.6 mm, 2.0 mm, and 2.6 mm, respectively. Similarly, the droplet surface area coverage on the sidewalls made of PE, UV+PE, and IR+PE films was 48%, 23%, and 16% with droplet mean diameter of 1.2 mm, 1.2 mm, and 2.6 mm, respectively. Droplets on the D-Poly covers were not characterized owing to the small amount of condensation. The total hemispherical transmittance of solar radiation in the visible was estimated by simultaneously measuring the photon flux density outside and inside the greenhouse using a SunScan analyzer connected to a data logger. The largest decrease in the total hemispherical transmittance, with respect to their dry state, was observed in August and reached about 13%, 11%, and 11% for PE, UV+PE, and IR+PE films, respectively. The authors attributed the decrease in transmittance to the high droplet surface area coverage and volume. Note that the droplet contact angles on the different films were not reported. However, the expected small contact angle on UV+PE films [72] might explain why their transmittance losses were similar to those with the IR+PE films even though the droplet surface area coverage was larger.

Stanghellini et al.[60] performed experiments inside a greenhouse with replaceable covers made of (i) single-pane glass, (ii) double-pane glass, (iii) glass with a pyramid-shaped textured surface, (iv) single glass with antireflecting (AR) coating, (v) uncoated polycarbonate, and (vi) polycarbonate with an anti-drop coating favoring filmwise condensation. Quantum sensors were placed above and below the greenhouse rooftop to measure the total hemispherical transmittance of the covers in the photosynthetically active radiation (PAR) region (400-700 nm). The transmittance of the covers was determined by dividing the photon flux measured simultaneously inside and outside the greenhouse. The results indicated that the effect of droplets on the light transmittance depended on the cover material. Condensation did not affect the transmittance of the glass with a pyramid-shaped texture. This was attributed to the decrease in contact angle with increasing roughness favoring filmwise condensation instead of dropwise condensation. The total hemispherical transmittance of single-pane glass, double-pane glass, single glass with anti-reflective (AR) coating or uncoated polycarbonate decreased by 7%, 9%, 10%, or 18%, respectively, with respect to their dry state. The transmittance of the polycarbonate cover decreased more than that of the glass cover due to the larger droplet contact angle around 84° [73]. Unfortunately, the size distribution, surface area coverage, and contact angle of the water droplets were not reported. Finally, the total hemispherical transmittance of the anti-drop coated polycarbonate slab with a low contact angle and thickness of 16 mm increased by 3% due to the presence of a water film.

Bhardwaj et al.[22] performed outdoor tests of solar stills featuring a 2 mm thick cover made of (i) glass, (ii) polyethylene terephthalate (PET), (iii) polycarbonate (PC), or (iv) polymethyl methacrylate (PMMA or acrylic). The covers were facing South and were inclined at an angle of 30° with respect to the horizontal. The contact angle θ_c of water droplets on the glass, PET, PC,

and PMMA covers were reported as 30°, 71°, 72.5°, and 82°, respectively. The water production was found to decrease by 40% as the droplet contact angle increased from 30° to 82°. The authors concluded that the transmission of solar irradiation through the wet covers decreased with increasing droplet contact angle. Note, however, that the droplet surface area coverage was not reported and might have varied as droplets slid or dripped more or less depending on the cover material. Similarly, the transmittance may change with cover material due to their different optical properties. The authors recommended the use of hydrophilic cover materials with a low droplet contact angle to maximize water production.

The experimental observations reported to date confirmed that the transmittance in the visible decreased with dropwise condensation on the back side of windows [7–9,18,22,59,61,69,70]. However, most of the previous experimental studies have not systematically characterized the water droplet contact angle, size, and surface area coverage and/or investigated their effect on the window transmittance and reflectance. This might be due to experimental challenges such as (i) uncontrollable and continuously changing outdoor weather conditions (humidity, temperature, dew point), (ii) contamination on the cover material, and/or (iii) rolling off and entrainment of droplets. These phenomena render difficult the measurements of contact angle and surface coverage and limited their achievable range.

This chapter aims to experimentally investigate radiation transfer through semi-transparent glass slabs supporting pendant droplets condensed at their back side. To do so, surface-treated glass slabs supporting acrylic droplets with different contact angles and surface area coverages were prepared and systematically characterized. In particular, their normal-hemispherical transmittance and reflectance were measured in the visible and near-infrared parts of the

electromagnetic spectrum. The measurements were compared with predictions by the previously developed Monte Carlo Ray Tracing method [55,66] applied to our specific samples.

2.2 Materials and methods

2.2.1 Sample preparation

Five different types of glass samples with different surface treatments were prepared to achieve different droplet contact angles including (1) bare soda-lime glass, (2) soda-lime glass coated with commercial water-repellent spray (Rain-X®, USA), (3) soda-lime glass coated with perfluorinated silane (tridecafluoro-1,1,2,2,-tetrahydrooctyl)trichlorosilane, Gelest, USA) referred to as perfluorinated silane, (4) soda-lime glass coated with a perfluorinated silane-treated monolayer of silica nanoparticles, (5) soda-lime glass coated with Teflon AF-2400 (Chemours, USA). Plane-parallel soda-lime silicate glass slabs, 3 mm in thickness with a surface area of 2.5 x 2.5 cm^2, were kindly provided by Asahi Glass Corporation, Yokohama, Japan. All samples were cleaned with isopropyl alcohol (IPA) prior to any surface treatment.

First, the soda-lime glass slabs coated with water-repellent spray were prepared by spraying the commercial product Rain-X® (620115, 2-in-1 exterior detailer and water repellent) on a small dry cloth and applying it on one face of the glass sample.

Second, the glass samples coated with perfluorinated silane were prepared by placing the glass slabs inside a closed container filled with silane vapor. Silane with chlorine substituent reacts with hydroxyl groups (–OH) present on the glass surface according to [74]

$$\text{Si–Cl} + \text{HO–Si} \rightarrow \text{Si–O–Si} + \text{HCl} \qquad (2.1)$$

Note that only reacting bonds are shown in Equation (2.1). This reaction permanently grafts perfluorocarbon chains on the surface of the glass substrate to form a hydrophobic coating.

Third, before coating the glass slabs with a monolayer of perfluorinated silane-treated silica nanoparticles, the slabs were placed on a hot plate at 450 °C for 30 minutes to remove any oil, dirt, and organic residues. Silica nanoparticles with 307 ± 20 nm diameter were synthesized by the Stöber process [75,76]. In this process, tetraethyl orthosilicate (TEOS, 97.0+%, TCI America™), ethanol (EtOH, 200 proof, Rossville Gold Shield), ammonium hydroxide (NH_4OH, VWR Chemicals BDH), and deionized (DI) water were used without any further purification. First, EtOH (8 mL), NH_4OH (0.31 mL), and DI water (1.4 mL) were mixed vigorously with a magnetic stirrer under atmospheric conditions. After 2 minutes of stirring, TEOS (1.5 mL) was quickly added in a single step. The solution was left to stir for 24 hours to allow for the complete growth of nanoparticles. Then, the ethanol/water-based silica nanoparticle suspension was sonicated to break any nanoparticle aggregate. The suspension was drop-casted onto the glass slabs [77] to obtain a monolayer of silica nanoparticles. Then, the glass slab was heat-treated at 450 °C for 1 hour to bond the nanoparticles onto the glass surface and render the coating mechanically robust. Finally, the surface of the silica nanoparticle coating was rendered hydrophobic by depositing perfluorinated silane using the method previously described. The silica nanoparticles before the silane treatment were characterized using a scanning electron microscope (SEM) (JEOL, JSM-6700F) and an atomic force microscope (AFM) (Bruker, Dimension FastScan).

Fourth, some glass slabs were spin-coated with Teflon AF-2400 followed by heat-treatment on a hot plate at 250 °C for an hour. Finally, the sample was baked in a furnace at 340 °C for 3.5 hours to achieve a 50 nm thick Teflon film [78].

Following the preparation of the glass slabs with or without surface treatment, thousands of transparent droplets made of ultraviolet (UV) curable acrylic polymer (Loctite AA 349) were deposited onto the glass substrate. The tip of the needle of a syringe was used to deposit liquid

acrylic droplets from the container onto the glass substrate. This procedure was repeated until the desired droplet surface area coverage was achieved. Lastly, the acrylic droplets were cured with a UV lamp at 365 nm (Blak-Ray B-100A, Thermo Scientific Fisher, USA). The use of polymer droplets instead of water droplets facilitated the handling of the samples and eliminated the challenges caused by water droplet motion and evaporation on the glass surface. In addition, the droplet surface area coverage and size distribution could be carefully characterized for each sample and remained the same throughout the experiments. The refractive index of acrylic falls between that of air and that of soda-lime glass [79,80]. Thus, the optical effects caused by the presence of droplets are expected to be qualitatively similar to that of water droplets despite the difference in their refractive indices.

2.2.2 Droplet characterization

The contact angle of acrylic droplets on the glass substrate was measured using a Drop Shape Analyzer (DSA100, Kruss Scientific, Germany). For each type of glass substrate, the contact angle measurements were repeated for 9 droplets to obtain the mean contact angle $\bar{\theta}_c$ and the associated 95% confidence interval. In addition, the projected droplet diameter d_p and surface area coverage f_A were measured from microscope images captured with a Leica LMIL microscope (Leica Microsystems, USA) connected to a CCD camera (Spot Insight model 4.2, USA). The image analysis software ImageJ was used to manually measure the droplets' location and projected diameter.

2.2.3 Optical characterization

The normal-hemispherical transmittance and reflectance of the previously described dry and droplet-covered glass slabs were measured using a double-beam ultraviolet-visible (UV-Vis) spectrophotometer (iS50, Thermo Scientific Fisher, USA) equipped with an integrating sphere

(EVO220, Thermo Scientific Fisher, USA). Measurements were performed in the visible and near-infrared range between 400 nm and 1100 nm in 1 nm increment.

2.2.4 Numerical simulations

Figure 2.1 shows a schematic of a semi-transparent glass slab of length L, width W, and thickness H covered with polydisperse droplets with contact angle θ_c and projected diameter d_p. The complex index of refraction of the semi-transparent glass was denoted by $m_{g,\lambda} = n_{g,\lambda} + \mathrm{i}\, k_{g,\lambda}$ while that of the droplets was denoted by $m_{d,\lambda} = n_{d,\lambda} + \mathrm{i}\, k_{d,\lambda}$. In order to predict the normal-hemispherical transmittance and reflectance of droplet-covered glasses, the following main assumptions were made: (1) the droplets were cap-shaped with a constant curvature, (2) all droplets had the same contact angle, (3) all interfaces were optically smooth, and (4) interferences and other wave effects were ignored.

Numerical simulations of the normal-hemispherical transmittance and reflectance of non-absorbing droplet-covered glasses were performed using the MCRT method. The algorithm was described in detail in Ref.[55] and need not be repeated. In all simulations, the total number of photon bundles simulated was 10^7 to ensure numerical convergence [55]. Note that simulations of the spectral normal-hemispherical transmittance and reflectance of the Teflon AF-2400 coated soda-lime glass slab with droplet mean contact angle $\bar{\theta}_c$ = 76.2° and surface area coverage f_A = 45% faithfully simulated the more than 2000 polydisperse droplets with their precisely measured position and projected diameter, as illustrated in Figure 2.2. Other simulations assumed droplets to be polydisperse and their diameter followed a normal distribution with an average diameter of $\bar{d}_p$ = 250 μm and standard deviation σ = 150 μm to ensure that the droplet diameter was much smaller than the capillary length and that Assumption 1 was satisfied.

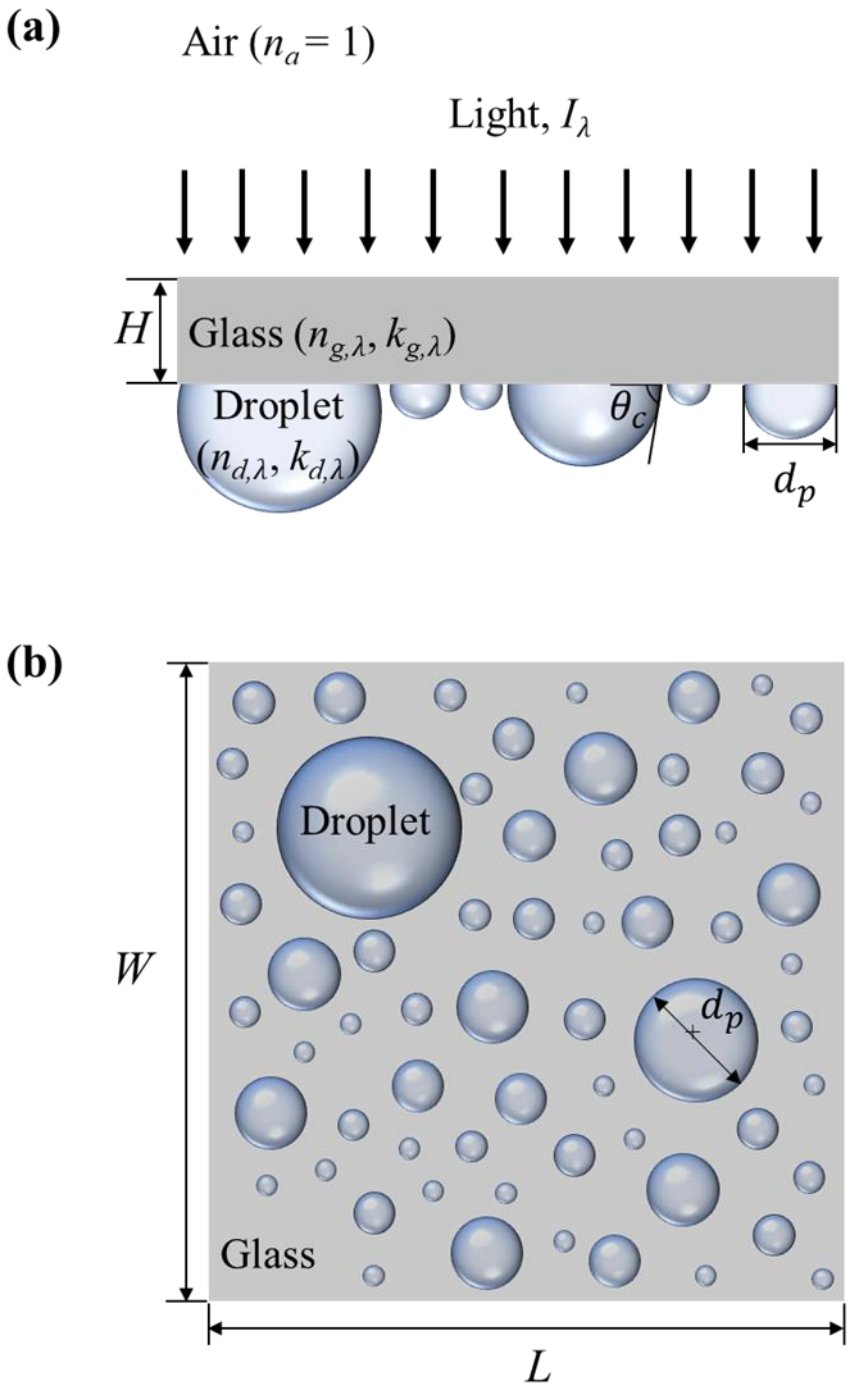

Figure 2.1. Schematic of a semi-transparent glass supporting non-absorbing polydisperse droplets (a) front view, (b) top view.

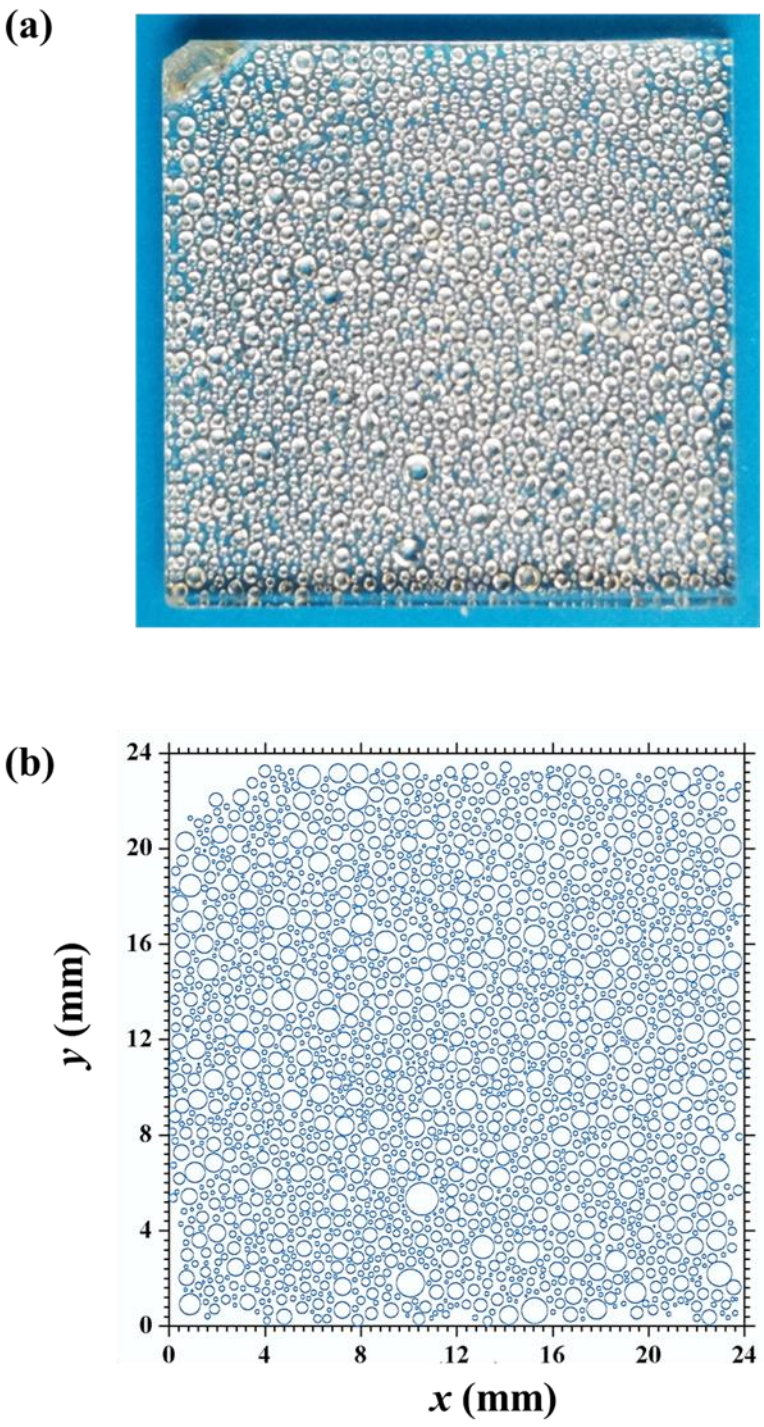

Figure 2.2. (a) Photograph of the Teflon-coated glass sample covered with acrylic droplets with contact angle $\bar{\theta}_c$= 76.2° and surface area coverage f_A = 45% and (b) corresponding computer-generated droplets.

Note that previous numerical simulations established that the droplet size distribution had no effect on the directional-hemispherical transmittance of glass panes supporting droplets on their back side provided that the droplets were non-absorbing and their diameters were small to ensure that they were cap-shaped [55,66].

The spectral refractive $n_{g,\lambda}$ and absorption $k_{g,\lambda}$ indices of the bare soda-lime silica glass slab used in all simulations were retrieved from the measured normal-normal transmittance $T_{nn,g,\lambda}$ and reflectance $R_{nn,g,\lambda}$ in the wavelength range from 400 to 1100 nm using the following analytical expressions [81]

$$T_{nn,g,\lambda} = \frac{(1-\rho_{ag,\lambda})^2 e^{-\kappa_{g,\lambda}H}}{1-\rho_{ag,\lambda}^2 e^{-2\kappa_{g,\lambda}H}} \quad \text{and} \quad R_{nn,g,\lambda} = \rho_{ag,\lambda}\left(1 + \frac{(1-\rho_{ag,\lambda})^2 e^{-2\kappa_{g,\lambda}H}}{1-\rho_{ag,\lambda}^2 e^{-2\kappa_{g,\lambda}H}}\right). \tag{2.2}$$

Here, $\rho_{ag,\lambda}$ is the spectral reflectivity of the air/glass interface and $\kappa_{g,\lambda}$ is the spectral absorption coefficient of the glass slab expressed as [81]

$$\rho_{ag,\lambda} = \frac{(n_{g,\lambda}-1)^2+k_{g,\lambda}^2}{(n_{g,\lambda}+1)^2+k_{g,\lambda}^2} \quad \text{and} \quad \kappa_{g,\lambda} = \frac{4\pi k_{g,\lambda}}{\lambda}. \tag{2.3}$$

Finally, the refractive $n_{d,\lambda}$ and absorption $k_{d,\lambda}$ indices of the acrylic were taken from Refs.[79] and [82], respectively.

2.3 Results and discussion

2.3.1 Sample characterization

Figure 2.3 shows (a) an SEM image of aggregates of the synthesized silica nanoparticles and (b) an AFM image of the silica nanoparticle monolayer deposited onto a glass slab. The arithmetic average surface roughness of the coating was measured as 35 nm based on AFM images.

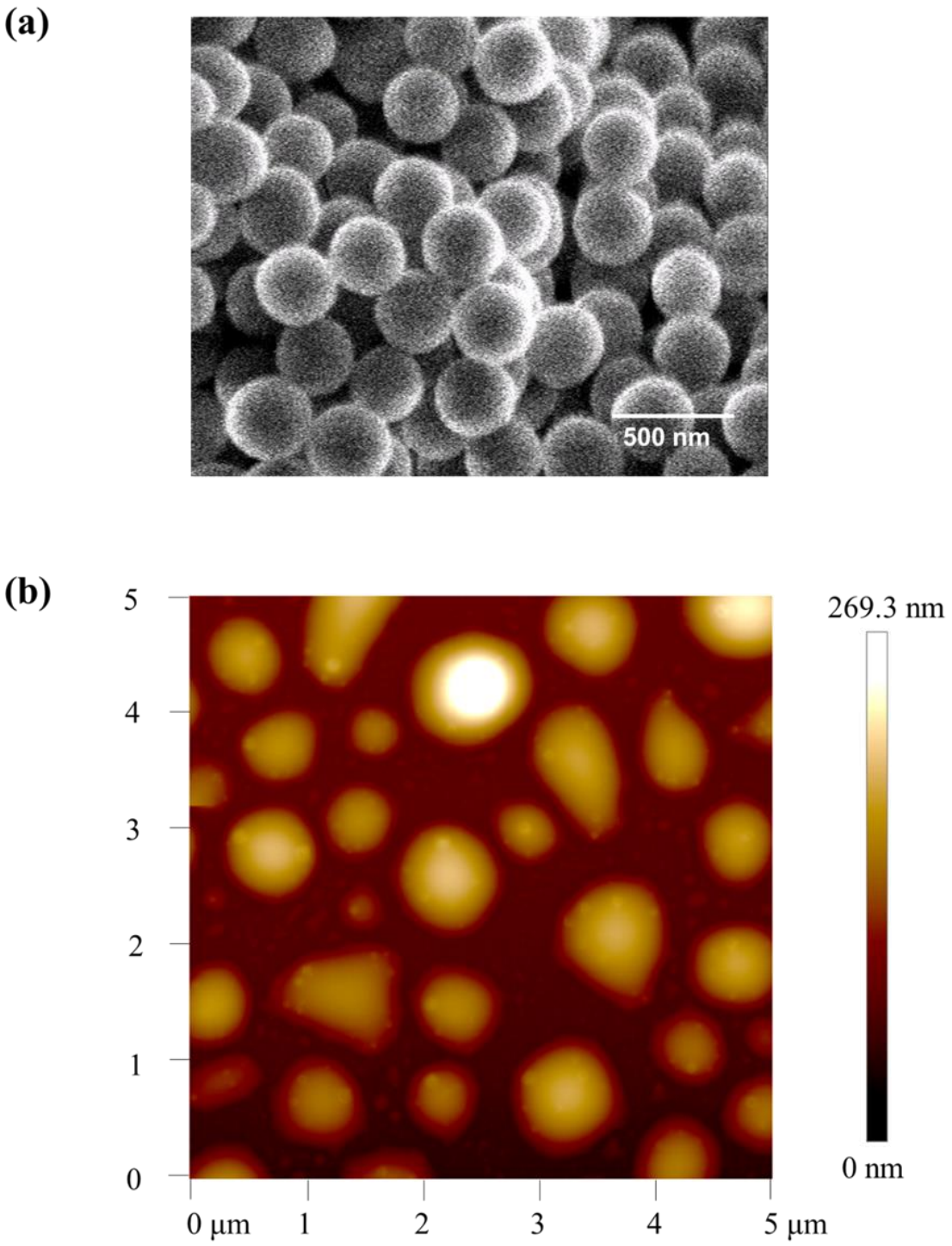

Figure 2.3. (a) SEM images of the aggregates of silica nanoparticles synthesized by the Stöber process and (b) AFM image of the silica nanoparticle monolayer deposited onto a glass slab.

Table 2.1 summarizes the different droplet-covered and surface-treated glass slabs fabricated with different droplet mean contact angle $\bar{\theta}_c$ and surface area coverage f_A. The droplet mean contact angle for the (i) bare glass slabs or glass slabs coated with (ii) water-repellent, (iii) perfluorinated silane, (iv) perfluorinated silane-treated monolayer of silica nanoparticles, and (v) Teflon AF-2400 was $\bar{\theta}_c$ = 25.8 ± 2.2°, 37.1 ± 3.8°, 54.8 ± 4.6°, 66.6 ± 4.5°, and 76.2 ± 1.6°, respectively. In addition, the droplet surface area coverage f_A ranged between 19% and 59%. The droplet mean diameter varied between 250 μm and 614 μm. Finally, for the sake of completeness, measurements of the droplet contact angles are reported in Figure A.1 in Appendix. Similarly, Figure A.2 shows representative microscope images of the different samples (Samples 2, 4-6, and 9) and Figure A.3 plots the droplet size distribution for each of the 9 samples presented in Table 2.1.

Table 2.1. Summary of the characteristics of the surface-treated glass samples covered with acrylic droplets.

Sample #	**Coating**	**Droplet mean contact angle $\bar{\theta}_c$ (°)**	**Droplet surface area coverage f_A (%)**	**Droplet mean diameter $\bar{d}_p$ (μm)**
1	None	25.8 ± 2.2	40 ± 5	413 ± 194
2	None	25.8 ± 2.2	49 ± 5	614 ± 360
3	None	25.8 ± 2.2	59 ± 5	507 ± 283
4	Rain-X	37.1 ± 3.8	45 ± 5	368 ± 740
5	perfluorinated silane	54.8 ± 4.6	52 ± 5	606 ± 323
6	perfluorinated silane-treated silica nanoparticles	66.6 ± 4.5	47 ± 5	250 ± 308
7	50 nm Teflon film	76.2 ± 1.6	19 ± 5	428 ± 143
8	50 nm Teflon film	76.2 ± 1.6	34 ± 5	271 ± 161
9	50 nm Teflon film	76.2 ± 1.6	45 ± 5	312 ± 193

2.3.2 Optical characterization

2.3.2.1 Optical properties of the soda-lime silicate glass slabs

Figure A.4 in Appendix plots the spectral refractive $n_{g,\lambda}$ and absorption $k_{g,\lambda}$ indices of the soda-lime silicate glass slabs, retrieved from spectral normal-normal transmittance $T_{nn,g,\lambda}$ and reflectance $R_{nn,g,\lambda}$, as functions of wavelength between 400 and 1100 nm. It also plots the refractive $n_{d,\lambda}$ and absorption $k_{d,\lambda}$ indices of acrylic [79,82], as well as that of Teflon AF-2400 [83,84] over the same spectral window. Figure A.4 indicates that the retrieved values of $n_{g,\lambda}$ and $k_{g,\lambda}$ differed slightly from those reported in the literature [80,85] but featured similar trends with respect to wavelength. The difference can be attributed to variations in the glass composition.

2.3.2.2 Spectral normal-hemispherical transmittance and reflectance

Figure 2.4 shows the measured spectral normal-hemispherical (a) transmittance $T_{nh,\lambda}$ and (b) reflectance $R_{nh,\lambda}$ as functions of wavelength λ for the dry and droplet-covered glass slabs featuring droplet mean contact angle $\bar{\theta}_c$ = 25.8° and surface area coverage f_A = 40%, 49%, and 59% (Samples 1, 2, 3). Figure 2.4 indicates that, for dry glass, the spectral normal-hemispherical transmittance $T_{nh,\lambda}$ and reflectance $R_{nh,\lambda}$ decreased with increasing wavelength λ due to absorption attributed to the iron oxide content of the glass [85,86]. In addition, it establishes that the measured spectral normal-hemispherical transmittance $T_{nh,g,\lambda}$ and reflectance $R_{nh,g,\lambda}$ of the dry glass slab were in good agreement with predictions by Equations (2.2) and (2.3). This observation confirms that the refractive and absorption indices of the glass slabs were properly retrieved. Moreover, Figure 2.4(a) shows that the presence of droplets did not affect the spectral normal-hemispherical transmittance $T_{nh,\lambda}$ for droplet contact angle $\bar{\theta}_c$ = 25.8° and surface area coverage f_A between 40% and 60%.

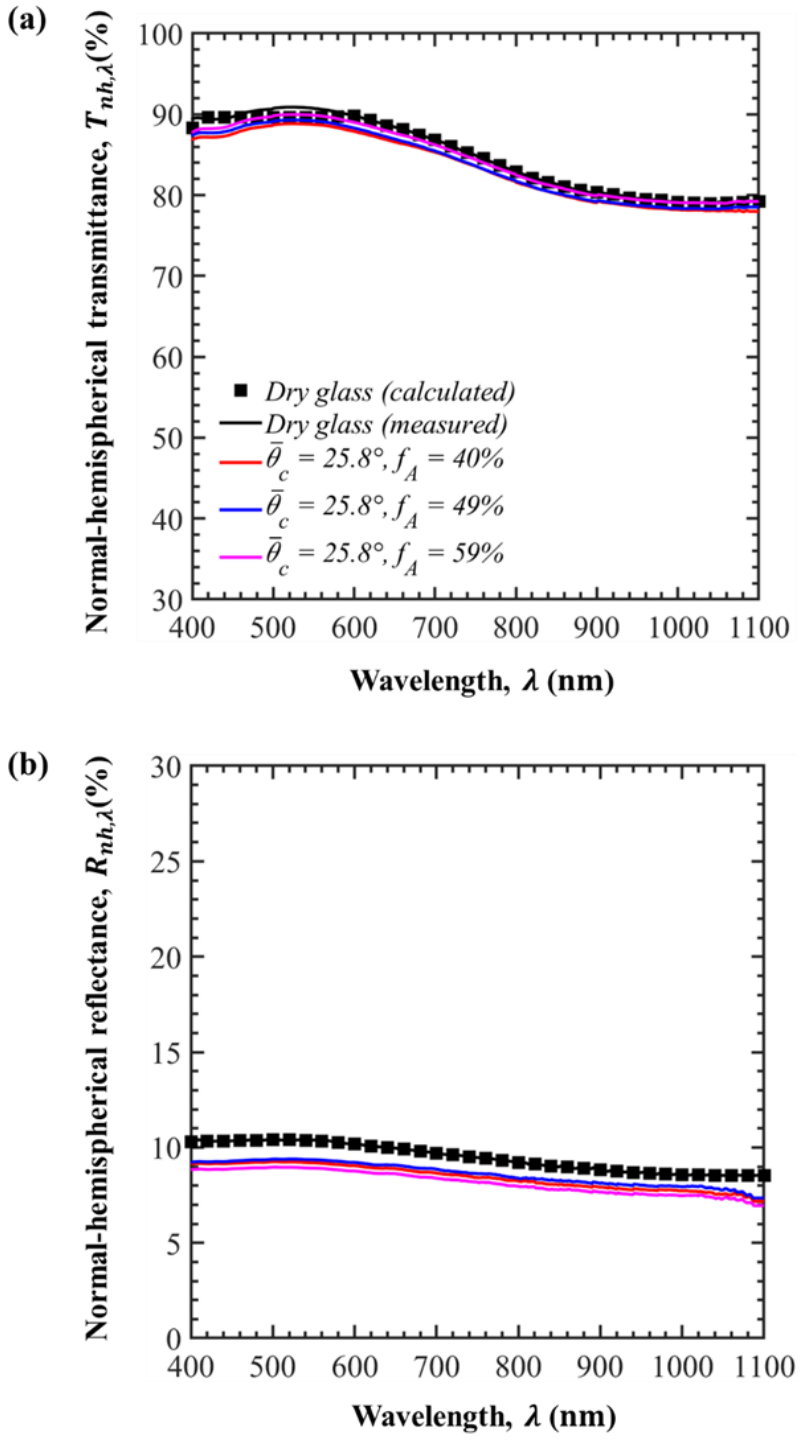

Figure 2.4. Normal-hemispherical (a) transmittance $T_{nh,\lambda}$ and (b) reflectance $R_{nh,\lambda}$ as functions of wavelength λ for dry glass and droplet-covered samples with mean contact angle $\bar{\theta}_c$ = 25.8° (< θ_{cr} in Regime I) and surface area coverage f_A = 40, 49, and 59%.

These results are consistent with numerical predictions reported by Zhu et al.[55] for non-absorbing water droplets with small contact angle such that $\bar{\theta}_c < \theta_{cr}$ corresponding to Regime I, as previously discussed. Figure 2.4(b) shows that the spectral normal-hemispherical reflectance $R_{nh,\lambda}$ decreased slightly due to the presence of droplets, as predicted by Tow [67]. However, the spectral normal-hemispherical reflectance $R_{nh,\lambda}$ was found to be mostly independent of surface area coverage f_A. This can be attributed to the fact that acrylic droplets had a similar refractive index to that of the glass window.

Figure 2.5 plots the (a) transmittance $T_{nh,\lambda}$ and (b) reflectance $R_{nh,\lambda}$ as functions of wavelength λ between 400 and 1100 nm for dry and droplet-covered glass slabs with $\bar{\theta}_c$ = 76.2° and f_A = 19, 34, and 45% (Samples 7, 8, 9). Unlike Figure 2.4 (a) for $\bar{\theta}_c$= 25.8°, Figure 2.5(a) indicates that the spectral normal-hemispherical transmittance $T_{nh,\lambda}$ decreased significantly with increasing droplet surface area coverage f_A across the spectral range considered. This situation corresponds to Regime II defined by Zhu et al.[55]. Figure 2.5(b) also indicates that the normal-hemispherical reflectance $R_{nh,\lambda}$ increased with increasing droplet surface area coverage f_A due to backscattering caused by total internal reflection at the droplet/air interface [69].

Moreover, Figures 2.5(a) and 2.5(b) compare experimental measurements with predictions obtained from MCRT simulations. Excellent agreement was obtained between experimental measurements and simulations for $T_{nh,\lambda}$ across the spectral window and for all values of surface area coverage f_A considered. However, Figure 2.5(b) indicates that the measured normal-hemispherical reflectance $R_{nh,\lambda}$ was systematically smaller than the numerical predictions, particularly with increasing surface area coverage f_A.

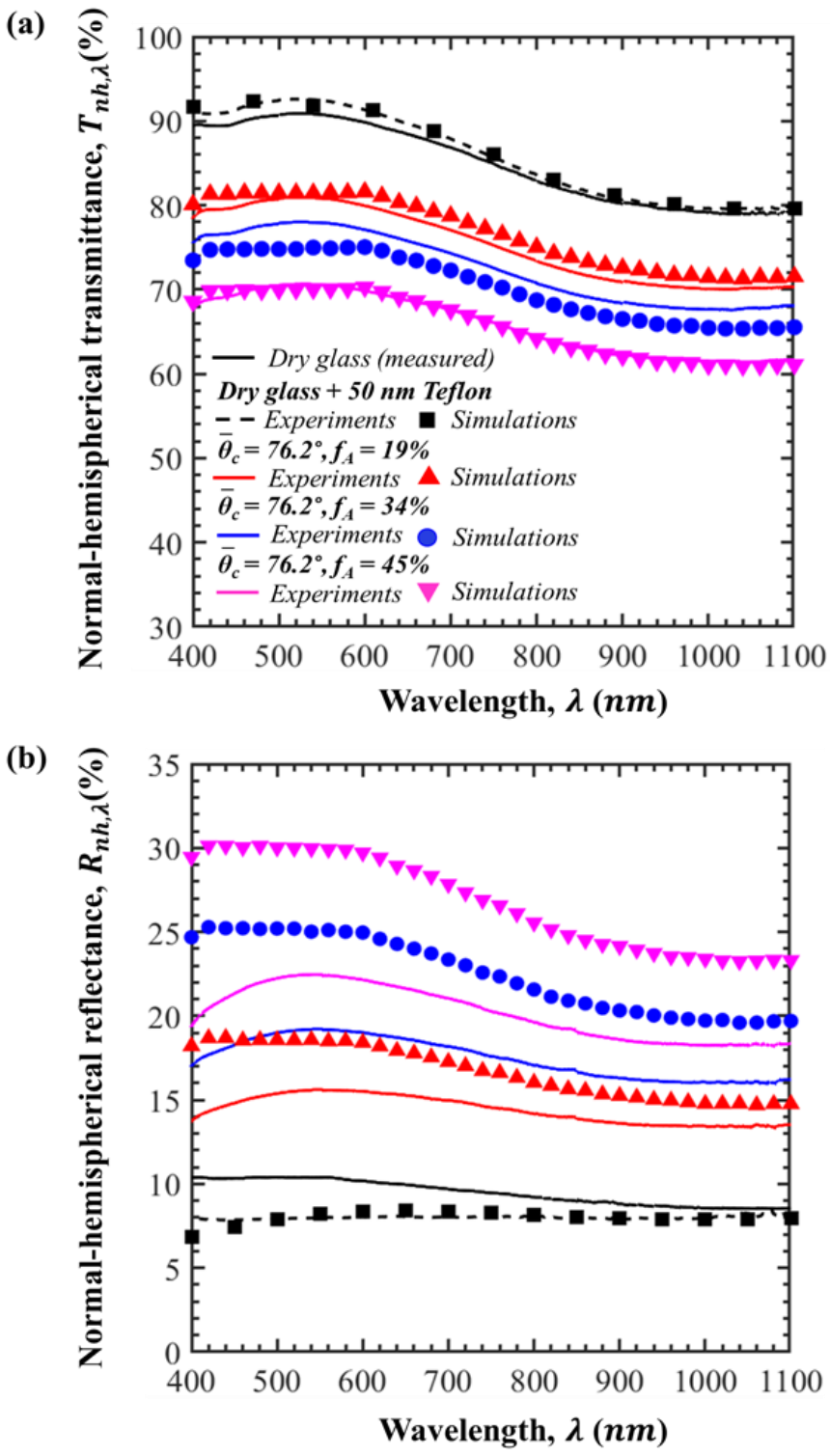

Figure 2.5. Normal-hemispherical (a) transmittance $T_{nh,\lambda}$ and (b) reflectance $R_{nh,\lambda}$ as functions of wavelength λ for dry glass, dry glass with 50 nm Teflon coating, and samples with mean contact angle $\bar{\theta}_c$ = 76.2° (Regime II) and surface area coverages f_A = 19, 34, and 45%.

This discrepancy can be attributed to the presence of the 50 nm thick Teflon coating, which was not accounted for in the MCRT simulations based on geometric optics and ignoring wave effects and interferences occurring in the Teflon thin film. Indeed, Figures 2.5(a) and 2.5(b) also show the spectral normal-hemispherical transmittance $T_{nh,\lambda}$ and reflectance $R_{nh,\lambda}$ of a 3 mm plane-parallel glass slab uncoated and coated with a 50 nm thick Teflon film as predicted from electromagnetic wave theory using TFCalc software (Software Spectra, Inc., Portland, OR, USA) and the refractive index of Teflon AF-2400 *(*$n \approx 1.28$*)* taken from Ref.[83]. These predictions, accounting for interferences, were in excellent agreement with experimental measurements for $T_{nh,\lambda}$ and $R_{nh,\lambda}$ of the dry window coated with 50 nm thick Teflon film. Figure 2.5 indicates that the presence of the 50 nm Teflon film slightly increased the normal-hemispherical transmittance but decreased the normal-hemispherical reflectance of the glass pane ($n_g \approx 1.59$) particularly for wavelengths less than 600 nm. Indeed, the presence of the Teflon film ($n \approx 1.28$) reduced the refractive index mismatch at the window/air interface (1.6/1) and thus reduced the amount of total internal reflection occurring at the back surface of the window. In fact, the slight gain in transmittance $T_{nh,\lambda}$ resulted in a similar reduction in reflectance $R_{nh,\lambda}$. For the same reason, the reflectance of any of the dry coated samples was smaller than the uncoated dry glass pane. In fact, their absorptance $A_{nh,\lambda} = 1 - T_{nh,\lambda} - R_{nh,\lambda}$ was nearly identical for all samples with or without coating [Figure A.5(c)]. It increased monotonously with wavelengths above 550 nm to reach 13% at 1100 nm and closely followed the trend observed in the spectral absorption index of soda-lime silica glass [85] [Figure A.4]. Similar differences and trends can be observed between the measured and predicted normal-hemispherical reflectance $R_{nh,\lambda}$ of droplet-covered glass samples. The absorptance $A_{nh,\lambda}$ of the glass with droplets increased slightly with increasing contact angle $\bar{\theta}_c$ and/or surface coverage

f_A. This was due to the fact that the acrylic droplets absorbed light in a similar spectral window as the glass, albeit with a smaller absorption index k_d.

2.3.2.3 Effect of droplet contact angle

Figure 2.6 shows the measured spectral normal-hemispherical (a) transmittance T_{nh} and (b) reflectance R_{nh} as functions of wavelength λ for dry glass and droplet-covered samples with different contact angles $\bar{\theta}_c$ ranging from 25.8° to 76.2° and similar surface area coverage $f_A \approx 48\pm$ 4% (Samples 2, 4-6, 9). Figure 2.6 indicates that for contact angles $\bar{\theta}_c < \theta_{cr}$, the normal-hemispherical transmittance T_{nh} increased and reflectance R_{nh} decreased slightly with increasing contact angle $\bar{\theta}_c$. However, for contact angles $\bar{\theta}_c \geq \theta_{cr}$, the normal-hemispherical transmittance T_{nh} decreased and the reflectance R_{nh} increased significantly with increasing contact angle $\bar{\theta}_c$.

Moreover, Figure 2.7 plots the measured and simulated normal-hemispherical (a) transmittance T_{nh} and (b) reflectance R_{nh} at wavelength λ = 410 nm as functions of contact angle $\bar{\theta}_c$ for dry and droplet-covered glass slabs with surface area coverage $f_A \approx 48\pm$ 4% (Samples 2, 4-6, 9). As a reference, the measured normal-hemispherical transmittance T_{nh} and reflectance R_{nh} at 410 nm of the dry glass slabs with and without coatings were also plotted at their corresponding contact angle with acrylic droplets. This wavelength was selected because the sum of the normal-hemispherical transmittance and reflectance of the samples approached 100% so that absorption by the glass pane and the droplets could be neglected, as assumed by Zhu et al.[55]. Note that the error bars associated with transmittance and reflectance measurements were 4.4% and 1.3%, respectively. They were estimated by considering two main sources of uncertainties during the experiments namely random and instrumentation uncertainties, as presented in Appendix.

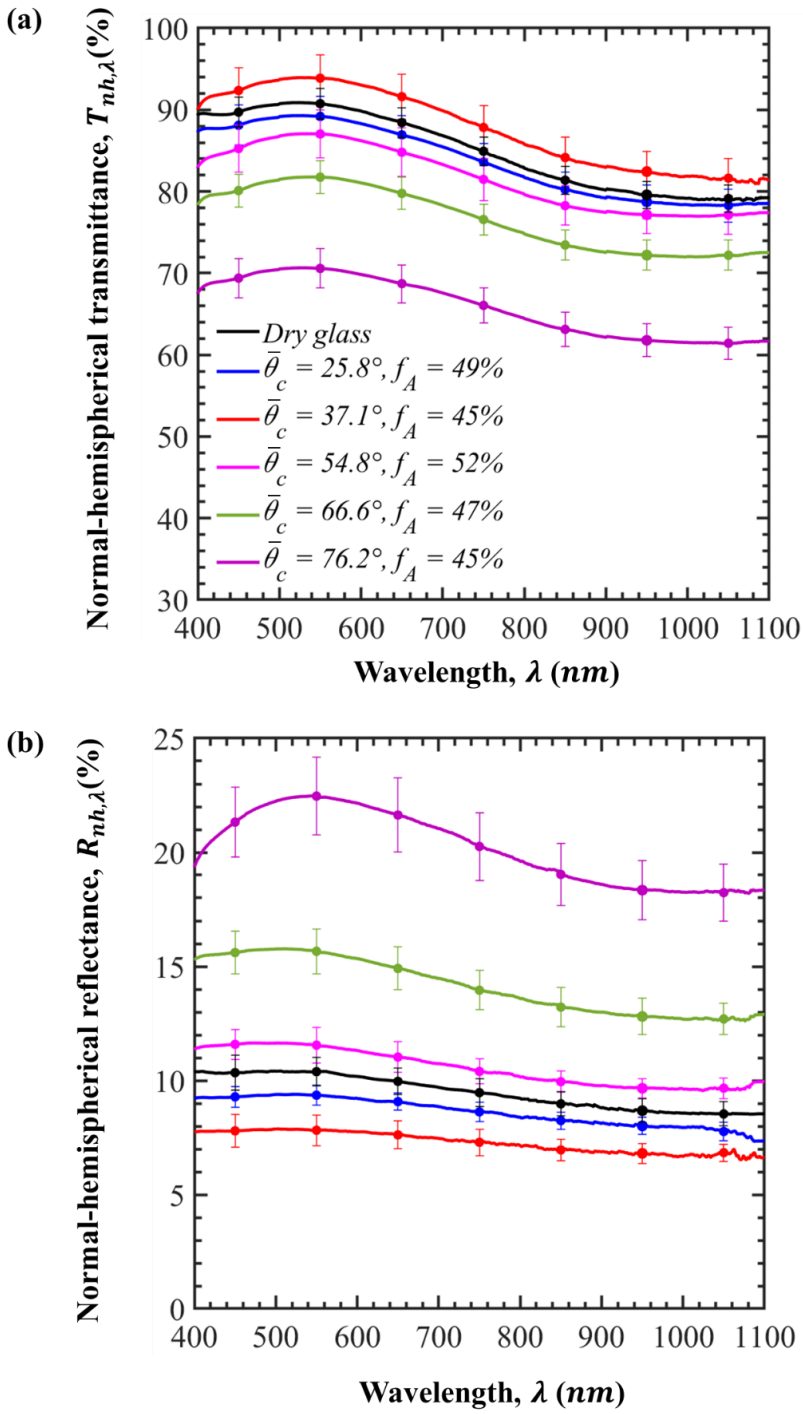

Figure 2.6. Normal-hemispherical (a) transmittance $T_{nh,\lambda}$ and (b) reflectance $R_{nh,\lambda}$ as functions of wavelength λ for dry glass and droplet-covered samples with different contact angles ranging from 25.8° to 76.2° (Samples 2, 4-6, 9) and similar surface area coverage around 48 ± 4%.

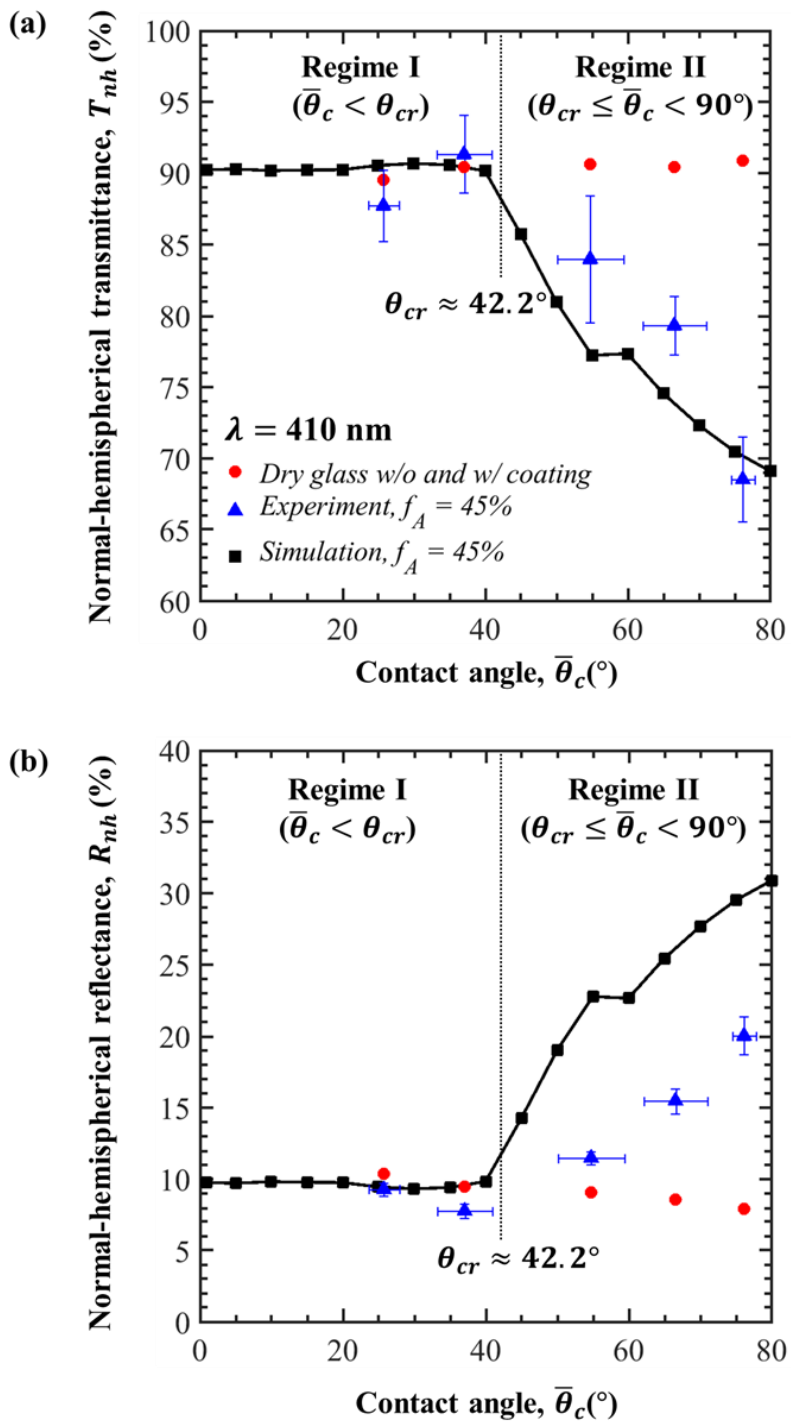

Figure 2.7. Comparison of the measured and simulated normal-hemispherical (a) transmittance T_{nh} and (b) reflectance R_{nh} at 410 nm as functions of contact angle $\bar{\theta}_c$ for dry glass slabs with and without coatings and droplet-covered samples with different surface treatments (Samples 2, 4-6, 9) and droplet surface area coverage $f_A \approx 48 \pm 4\%$.

First, Figure 2.7 indicates that, for dry glass slabs, the normal-hemispherical transmittance T_{nh} at λ = 410 nm increased only slightly by less than 2% due to the presence of coating while the normal-hemispherical reflectance R_{nh} decreased accordingly. For the sake of completeness, Figure A.5 in Appendix plots the spectral normal-hemispherical transmittance $T_{nh,\lambda}$, reflectance $R_{nh,\lambda}$, and absorptance $A_{nh,\lambda}$ of the dry glass slabs with and without coating. Moreover, Figure 2.7(a) indicates that the normal-hemispherical transmittance T_{nh} slightly increased with increasing contact angle $\bar{\theta}_c$ in Regime I until it reached the critical angle for internal reflection at the droplet/air interface predicted by Snell's law as $\theta_{cr} = \sin^{-1}(n_a/n_d) \approx 42.2°$ [81]. In Regime II, corresponding to $\theta_{cr} \leq \bar{\theta}_c < 90°$, the measured normal-hemispherical transmittance T_{nh} decreased rapidly with increasing contact angle $\bar{\theta}_c$. For example, the normal-hemispherical transmittance T_{nh} decreased from 89% to 71% as $\bar{\theta}_c$ increased from 25.8° to 76.2°. The normal-hemispherical transmittance T_{nh} of the glass supporting acrylic droplets is expected to be qualitatively similar to that with water droplets despite the difference in their refractive indices (≈1.49 vs. 1.33). Indeed, our previous study [55] established that the normal-hemispherical transmittance T_{nh} of glass cover supporting droplets with surface area coverage f_A = 90% followed the same trends and was quantitatively similar for droplets with refractive index n_d equal to 1.33 or 1.6, as illustrated in Figure A.6. In addition, the optical Regimes I and II identified numerically by Zhu et al.[55] for water droplets were confirmed experimentally with acrylic droplets [Figure 2.7(a)]. Moreover, Figure 2.7(b) shows that the normal-hemispherical reflectance R_{nh} initially decreased ($\bar{\theta}_c < \theta_{cr}$) and then increased ($\theta_{cr} \leq \bar{\theta}_c < 90°$) with increasing contact angle $\bar{\theta}_c$. This could be attributed to the total internal reflection occurring at the droplet/air interface resulting in a decrease in the number of transmitted photons and an increase in the number of back-scattered photons [55].

Figures 2.7(a) and 2.7(b) also indicate that predictions of the normal-hemispherical transmittance and reflectance, obtained assuming $k_w = k_d = 0$, qualitatively followed the same trends as the experimental measurements. However, the measured and simulated reflectance differed quantitatively especially for samples with contact angle $\theta_{cr} < \bar{\theta}_c \leq 90°$ corresponding to Regime II. This discrepancy can be attributed to the fact that, unlike in Regime I (Samples 1-4), droplets in Regime II (Samples 5-9) reflected photons at the droplet/air interface back through the absorbing acrylic droplets and soda-lime glass window, as illustrated in Figures 8(a)-8(b) of Ref.[55]. As a result, more photons were not only reflected but also absorbed by the droplets and the window in the presence of a hydrophobic coating. In fact, Figure A.7 in Appendix plots the normal-hemispherical absorptance $A_{nh,\lambda}$ of the samples with the droplet contact angle (a) $\bar{\theta}_c < \theta_{cr}$ = 42° and (b) $\theta_{cr} < \bar{\theta}_c \leq 90°$ as well as that of the corresponding dry sample. Figure A.7 indicates that the normal-hemispherical absorptance $A_{nh,\lambda}$ of Samples 1–4 ($\bar{\theta}_c < \theta_{cr}$ = 42° - Regime I) was close to that of dry glass. However, the normal-hemispherical absorptance $A_{nh,\lambda}$ of Samples 5–9 ($\theta_{cr} < \bar{\theta}_c \leq 90°$ - Regime II) was larger than that of the dry glass and followed similar trends as the increase in the absorption index spectra of the soda-lime glass and acrylic [Figure A.4(b)]. Other discrepancies could be attributed to other effects such as the non-uniformity of the silane coating on the glass slab surface, as visually observed during the droplet deposition, resulting in variations in contact angle, reported in Table 2.1. Note also that the predicted normal-hemispherical transmittance and reflectance remained constant for droplet contact angle varying between 55° and 60°. This could be attributed to the fact that photons reflected at the droplet/air interface traveled through the droplet and the glass pane and experienced total internal reflection at the glass/air interface for contact angles $55° < \theta_c < 60°$. They were then transmitted through the

glass/droplet and droplet/air interface. The droplet contact angle initiating total internal reflection at the glass/air interface was equal to θ_c = 55.5°, as explained in detail in Appendix.

2.3.2.4 Effect of droplet surface area coverage

Figure 2.8 shows the normal-hemispherical (a) transmittance T_{nh} and (b) reflectance R_{nh} at wavelength λ = 410 nm as functions of surface area coverage f_A for dry and droplet-covered glass slabs with mean contact angle $\bar{\theta}_c$ = 25.8° and 76.2° (Samples 1-3, 7-9). Figure 2.8(a) indicates that in Regime I ($\bar{\theta}_c < \theta_{cr}$), the transmittance T_{nh} increased slightly with increasing surface area coverage f_A. By contrast, in Regime II ($\theta_{cr} \leq \bar{\theta}_c < 90°$), the transmittance T_{nh} decreased almost linearly with increasing f_A due to total internal reflection at the droplet/air interface, as explained in Ref.[55]. For example, the normal-hemispherical transmittance decreased from 81% to 71% as the surface area coverage increased from 19% to 45%. Here also, predictions by the MCRT simulations were in excellent agreement with experimental data. Finally, Figure 2.8(b) shows that the reflectance R_{nh} at 410 nm decreased slightly with increasing surface area coverage f_A in Regime I ($\bar{\theta}_c < \theta_{cr}$), and increased in Regime II ($\theta_{cr} \leq \bar{\theta}_c < 90°$), as predicted in Ref.[55]. The very good qualitative and quantitative agreements observed between numerical predictions and experimental measurements validate the numerical results reported previously [55,66] as well as the conclusions drawn including the existence of the optical Regimes I and II. Hydrophobic coatings have been recommended in solar energy applications such as greenhouses due to their anti-fogging [49] and self-cleaning property [87–89]. However, the present results establish that, strictly from a light transfer point of view, hydrophilic cover with droplet contact angle $\bar{\theta}_c < \theta_{cr}$ should be preferred to maximize net solar energy input in applications such as solar collectors, photobioreactors, solar desalination, and greenhouses since dropwise (or filmwise) condensation of hydrophilic surface does not affect solar transmittance significantly [22,49,52].

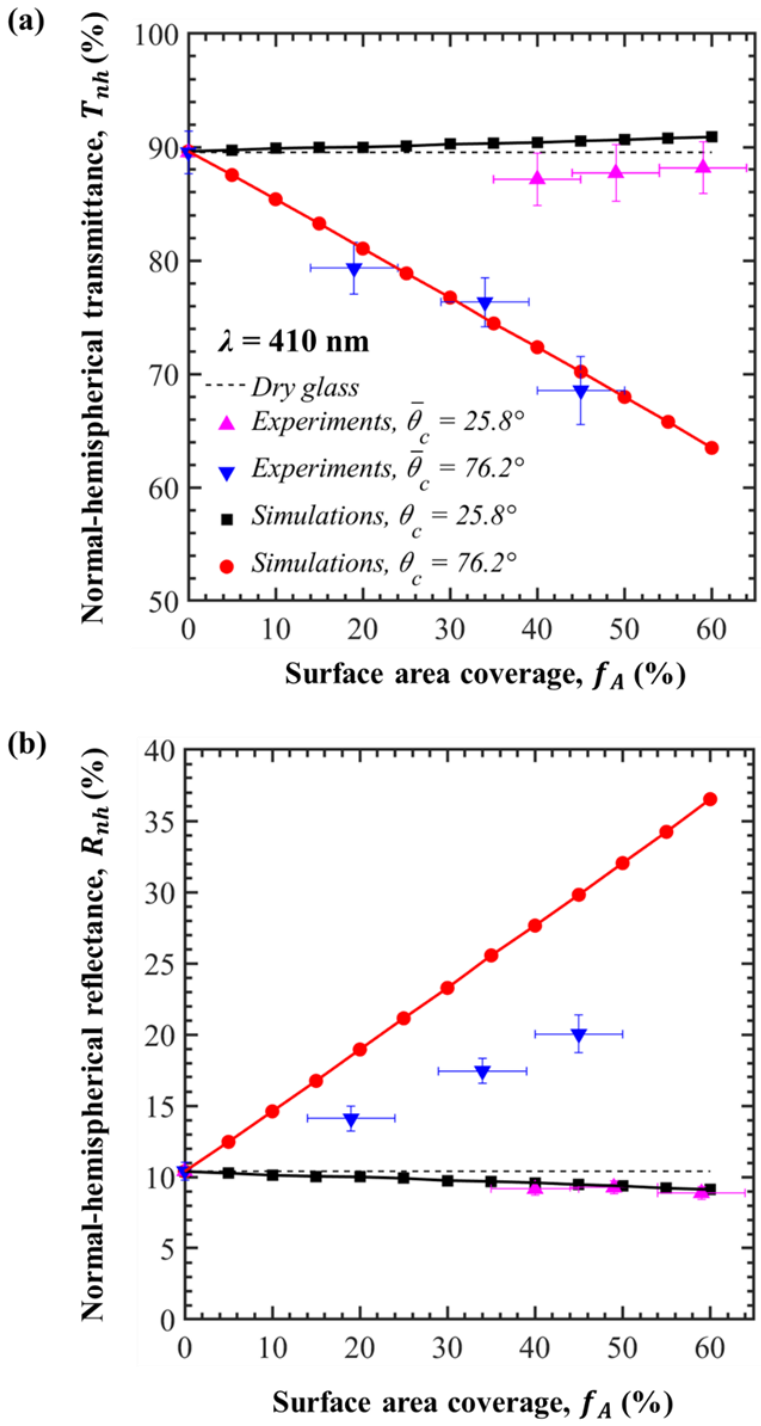

Figure 2.8. Comparison of the measured and simulated normal-hemispherical (a) transmittance T_{nh} and (b) reflectance R_{nh} at 410 nm as functions of surface area coverage f_A for dry and droplet-covered samples with mean contact angle $\bar{\theta}_c$ = 25.8° (Samples 1-3) and 76.2° (Samples 7-9).

2.4 Conclusion

This chapter investigated experimentally the effects of pendant droplets on the back side of semi-transparent glass slabs on their normal-hemispherical transmittance and reflectance. Soda-lime silica glass slabs without and with surface-treatment and covered with acrylic droplets were prepared with contact angle between 26° and 76° and surface area coverage between 0 and 60%. For droplet contact angle $\bar{\theta}_c$ smaller than the critical angle θ_{cr} for total internal reflection at the droplet/air interfaces (i.e., $\bar{\theta}_c < \theta_{cr}$), the spectral normal-hemispherical transmittance $T_{nh,\lambda}$ was independent of surface area coverage and increased slightly with increasing contact angle. For droplet contact angle such that $\theta_{cr} \leq \bar{\theta}_c < 90°$, the normal-hemispherical transmittance decreased with increasing contact angle and surface area coverage. This was attributed to total internal reflection at the droplet/air interfaces resulting in back-scattering. Predictions of the normal-hemispherical transmittance and reflectance, obtained using the Monte Carlo Ray Tracing method, were in good agreement with experimental measurements thus validating our simulation algorithm and confirming previous conclusions [55]. In particular, this chapter confirms the existence of optical Regimes I ($\bar{\theta}_c < \theta_{cr}$) and II ($\theta_{cr} \leq \bar{\theta}_c < 90°$) defined by Zhu et al.[55]. In practice, to minimize the effect of dropwise condensation on the efficiency of solar energy conversion systems, it is recommended to select durable hydrophilic cover materials or apply transparent hydrophilic coatings.

Chapter 3: Infrared Radiation Transfer through Semitransparent Windows Supporting Absorbing Droplets

This chapter experimentally and numerically investigates infrared radiation transfer through semitransparent glass windows covered with droplets on the front or back sides. The measured normal-hemispherical transmittance of glass windows with slightly absorbing droplets on the front side increased while the reflectance decreased with increasing droplet contact angle θ_c and surface area coverage f_A due to antireflecting effects. However, for droplets on the back side of the glass window with contact angles larger than the critical angle θ_{cr} for total internal reflection at the droplet/air interface, the spectral normal-hemispherical transmittance decreased by up to 55% while the reflectance increased with increasing contact angle θ_c and surface area coverage f_A. In the infrared spectral range when droplets were strongly absorbing, the normal-hemispherical transmittance decreased by up to 60% with increasing surface area coverage f_A of droplets either on the front or back side. The experimental measurements were in excellent agreement with numerical predictions obtained using the Monte Carlo ray-tracing method. Finally, the experimentally-validated numerical simulation tool was used to predict the hourly solar transmittance and the total hemispherical emissivity of horizontal glass windows covered with cap-shaped water droplets in Los Angeles, CA on June 21. In the presence of water droplets on the back side, the solar transmittance of the glass window decreased for most of the day by up to 26% whereas the total hemispherical emissivity remained unchanged. However, for droplets on

the front side of the glass window, the solar transmittance decreased in the morning or evening by up to 40% and the already high total hemispherical emissivity increased slightly.

3.1 Background

This section reviews both numerical and experimental studies focused on radiative transfer through *semitransparent* windows supporting *absorbing* droplets on either their *front* or *back* sides. The reader is referred to Ref.[55] for a review of the literature when both the window and the droplets are *non-absorbing*.

Zhu et al.[64] numerically predicted the normal-hemispherical transmittance of 3 mm thick *transparent* glass window (n_w = 1.5) supporting cap-shaped droplets (n_d = 1.33) on their *front side* using the Monte Carlo ray-tracing (MCRT) method. Monodisperse or polydisperse droplets were either randomly distributed or ordered in a hexagonal pattern with (i) projected droplet surface area coverage f_A varying between 10% and 90%, (ii) droplet contact angle θ_c between 10° and 180°, (iii) droplet absorption index k_d ranging from 0 to $5\text{x}10^{-2}$, and (iv) droplet projected diameter d_p equal to either 100 μm or 250 μm. The normal-hemispherical transmittance of windows supporting non-absorbing droplets on their front side was found to be independent of the droplet size and spatial arrangement. It was also independent of the droplet contact angle for contact angles θ_c < 160° and increased slightly with increasing droplet surface area coverage f_A. This was attributed to the antireflecting effect of the droplets caused by the decrease in the refractive index mismatch at the window surface ($1 = n_a < n_d = 1.33 < n_w = 1.5$) in the presence of droplets. However, for strongly absorbing droplets ($k_d \geq 10^{-2}$), the normal-hemispherical transmittance T_{nh} decreased significantly with increasing surface area coverage f_A, droplet diameter d_p, and contact angle θ_c for contact angles θ_c < 90°. This was attributed to the fact that the number of photons absorbed by the droplets increased as the volume of droplets increased. However, for contact

angles $\theta_c \geq 90°$, the normal-hemispherical transmittance T_{nh} reached its minimum value beyond which it was independent of the droplet contact angle θ_c, projected diameter d_p, and absorption index k_d. This was explained by the fact that, beyond a critical value of the absorption index k_d, all photons entering the droplets were absorbed. Then, the transmittance depended only on the surface area coverage f_A.

Hsieh and Rajvanshi [65] used the ray-tracing method to numerically predict the spectral normal-hemispherical transmittance and reflectance of a 2.3 mm thick soda-lime glass window supporting a single cap-shaped water droplet on its *back side* for wavelengths λ ranging from 0.5 to 2.6 μm. The droplet diameter d_p varied between 0.5 and 2.5 mm while the droplet contact angle was constant and equal to $\theta_c = 90°$. The spectral normal-hemispherical transmittance $T_{nh,\lambda}$ and reflectance $R_{nh,\lambda}$ were found to be independent of the droplet diameter d_p for wavelengths $\lambda < 0.9$ μm due to the small absorption index of water. However, both $T_{nh,\lambda}$ and $R_{nh,\lambda}$ decreased with increasing droplet diameter d_p for $0.9\ \mu m < \lambda < 2.6\ \mu m$ due to the increase in the absorption index of water.

Zhu and Pilon [66] used the MCRT method to numerically predict the normal-hemispherical transmittance through a *transparent* window ($n_w = 1.5$) supporting cap-shaped droplets ($n_d = 1.33$) on its *back side*. Numerous monodispersed cap-shaped droplets either distributed randomly or ordered in a hexagonal pattern were considered with (i) droplet contact angle θ_c ranging between 0° and 180°, (ii) droplet diameter d_p from 50 to 250 μm, (iii) projected droplet surface area coverage f_A between 30% and 55%, and (iv) droplet absorption index k_d between 0 and $5x10^{-2}$. For non-absorbing and slightly absorbing ($k_d \leq 10^{-4}$) droplets, four optical regimes were identified as a function of the droplet contact angle θ_c and the critical angle θ_{cr} for total internal reflection at the droplet/air interface. In Regime I ($\theta_c < \theta_{cr}$) and Regime IV ($\theta_c \geq 180° - \theta_{cr}$), the normal-

hemispherical transmittance T_{nh} was found to be mostly independent of droplet contact angle θ_c. This was due to the fact that the droplets scattered the photons in the forward direction. However, in Regime II ($\theta_{cr} \leq \theta_c < 90°$), the normal-hemispherical transmittance T_{nh} decreased with increasing droplet contact angle θ_c to reach a minimum at $\theta_c = 90°$ due to total internal reflection at the droplet/air interface. In Regime III ($90° \leq \theta_c < 180°- \theta_{cr}$), the normal-hemispherical transmittance T_{nh} increased with increasing droplet contact angle θ_c as a result of the decrease in the number of back-scattered photons due to a reduction in the fraction of the droplet/air interface where total internal reflection occurred. On the other hand, for strongly absorbing droplets ($k_d \geq 10^{-2}$), the normal-hemispherical transmittance T_{nh} decreased with increasing droplet contact angle θ_c up to 90° and remained constant for $\theta_c \geq 90°$. This was explained by the fact that, for contact angle $\theta_c \geq 90°$, the volume of the droplets was so large that all photons entering the droplets were absorbed.

Moreover, the numerical simulations for glass windows supporting droplets on their *back side* in Regimes I and II have recently been validated experimentally in the visible and near-infrared (0.4-1.1 μm) for acrylic droplets deposited on the back side of 3 mm-thick soda-lime glass slabs with or without hydrophobic coatings corresponding to droplet contact angle θ_c between 26° and 76° and surface area coverage f_A between 19% and 59% [90]. However, to the best of our knowledge, experimental validation of previous numerical simulations [64,66]. of radiation transfer through semitransparent windows supporting absorbing droplets on their front or back sides has not been reported in the literature. This chapter aims to experimentally and numerically investigate infrared radiation transfer through semitransparent glass windows covered with absorbing droplets on either their back or front sides. First, glass windows covered with acrylic droplets with different droplet contact angles and surface area coverages were prepared and systematically characterized. Then, their spectral normal-hemispherical transmittance and

reflectance were measured at wavelengths between 1.35 μm and 20 μm. In addition, experimental measurements for selected samples were compared with numerical predictions obtained from our previously developed code based on the MCRT method [55,64,66]. Finally, the experimentally-validated numerical code was used to predict the hourly solar transmittance and total hemispherical emissivity of the glass windows supporting water droplets on their back or front side.

3.2 Materials and methods

3.2.1 Sample preparation

The same samples as those prepared and described in detail in Table 2.1 were used in the present chapter. In brief, all samples consisted of 3 mm-thick plane-parallel soda-lime glass slabs (Asahi Glass Corporation, Yokohama, Japan) with a surface area of 2.5 x 2.5 cm^2. Nine different samples with or without hydrophobic coatings were prepared to achieve different droplet contact angles and projected surface area coverages including (1) clean and uncoated glass slabs with droplet surface area coverage f_A ranging between 40% and 60% (Samples 1, 2, 3), (2) glass slab coated with commercial water-repellent spray Rain-X® with a droplet surface area coverage f_A = 45% (Sample 4), (3) glass slab coated with a monolayer of perfluorinated silane (tridecafluoro-1,1,2,2,-tetrahydrooctyl)trichlorosilane (Gelest, USA) with a droplet surface area coverage f_A = 52% (Sample 5), (4) glass slab coated with a perfluorinated silane-treated monolayer of silica nanoparticles with 307 ± 20 nm diameter with a droplet surface area coverage f_A = 47% (Sample 6), and (5) glass slabs coated with 50 nm thick Teflon AF-2400 (Chemours, USA) film with droplet surface area coverage f_A ranging between 19% and 45% (Samples 7, 8, 9). Once the uncoated or coated glass slabs were prepared, thousands of droplets made of acrylic polymer (Loctite AA 349) were deposited by hand with the tip of a needle onto the glass and cured with a UV lamp (Blak-Ray B-100A, Thermo Scientific Fisher, USA) emitting at a wavelength 365 nm. Acrylic was

selected among other polymers because it is UV-curable and does not undergo any color change upon curing. It is also relatively viscous thus preventing the droplets from merging during deposition.

3.3 Analysis

3.3.1 Problem statement

Figure 3.1 shows a schematic representation of a semitransparent glass window of thickness H and spectral complex index of refraction $m_{g,\lambda} = n_{g,\lambda} + \mathrm{i}\, k_{g,\lambda}$, exposed to normally incident infrared radiation at wavelength λ. The glass window supported polydisperse droplets with contact angle θ_c, projected diameter d_p, and spectral complex index of refraction $m_{d,\lambda} = n_{d,\lambda} + \mathrm{i}\, k_{d,\lambda}$ on either its (a) back side or (b) front side. For the back side configuration, the photons were first incident on the semitransparent glass slab where they could be reflected, absorbed, or transmitted. A fraction of the photons transmitted through the glass slab reached the absorbing droplets. These photons could be (i) absorbed by the droplets, (ii) internally reflected at the droplet/air interface, or (iii) transmitted through the droplet/air interface. For the front side configuration [Figure 3.1(b)], the photons were directly incident on either the glass or the droplets. In either case, photons were reflected or refracted at each interface and could be absorbed by either the droplets or the glass slab. Here also, internal reflection may occur on the back surface of the glass window.

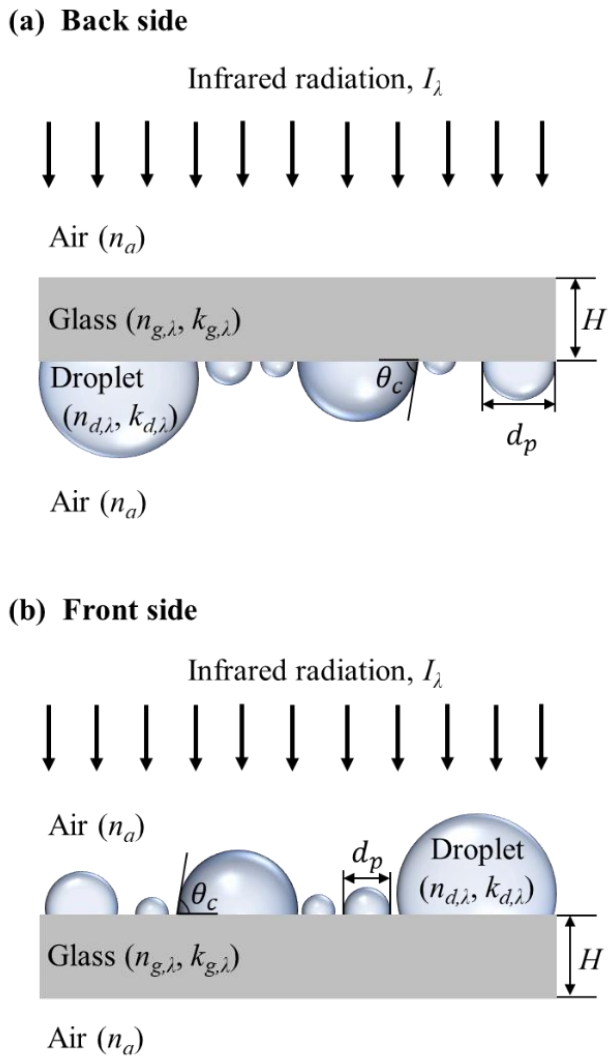

Figure 3.1. Schematic of a numerically simulated semitransparent glass window supporting absorbing polydisperse droplets on its (a) back side and (b) front side.

The spectral normal-hemispherical transmittance and reflectance of droplet-covered glass slabs were predicted using the MCRT method [64,66] based on the precisely measured coordinates and projected diameters of all droplets deposited on the glass slab for (i) Sample 3 consisting of an uncoated glass slab covered with droplets with mean contact angle $\bar{\theta}_c$ = 25.8° and surface area coverage f_A = 59% and (ii) Sample 9 featuring a glass slab coated with a 50 nm thick Teflon film with $\bar{\theta}_c$ = 76.2° and f_A = 45%. Both back and front side configurations were simulated.

3.3.2 Problem statement

The following assumptions were made to predict numerically the spectral normal-hemispherical transmittance and reflectance of the droplet-covered glass slabs: (1) all droplets were cap-shaped with constant curvature and identical contact angle θ_c; (2) the droplet size was much larger than the wavelength so geometric optics prevailed; (3) all interfaces were optically smooth so Snell's law and Fresnel equations applied; (4) the optical effects of the hydrophobic thin film coatings were ignored.

3.3.3 Optical properties of soda-lime glass and acrylic

The spectral refractive $n_{g,\lambda}$ and absorption $k_{g,\lambda}$ indices of the glass slab of thickness H = 3 mm were retrieved from the normal-normal transmittance $T_{nn,g,\lambda}$ and reflectance $R_{nn,g,\lambda}$ measurements in the spectral range from 1.35 to 20 μm by minimizing, for each wavelength, the sum δ_λ of the relative errors between the experimental measurements ($T_{nn,g,\lambda}$, $R_{nn,g,\lambda}$) and the theoretical predictions ($T^*_{nn,g,\lambda}$, $R^*_{nn,g,\lambda}$) for the transmittance and reflectance defined as

$$\delta_\lambda = \frac{\left|T_{nn,g,\lambda} - T^*_{nn,g,\lambda}\right|}{T_{nn,g,\lambda}} + \frac{\left|R_{nn,g,\lambda} - R^*_{nn,g,\lambda}\right|}{R_{nn,g,\lambda}}. \quad (3.1)$$

The pair ($n_{g,\lambda}$, $k_{g,\lambda}$) that minimized δ_λ was found using the sequential quadratic programming (SQP) method [91] ensuring that $\delta_\lambda < 5\text{x}10^{-2}$. The analytical expressions for $T^*_{nn,g,\lambda}$ and $R^*_{nn,g,\lambda}$ were given in Equation (2.2).

Figure 3.2 shows the spectral refractive $n_{g,\lambda}$ and absorption $k_{g,\lambda}$ indices of soda-lime glass retrieved from the transmittance $T_{nn,g,\lambda}$ and reflectance $R_{nn,g,\lambda,}$ measurements on an uncoated glass slab between 1.35 and 20 μm. The spectral refractive $n_{d,\lambda}$ and absorption $k_{d,\lambda}$ indices of acrylic for the same wavelength range were also shown in Figure 3.2, as reported in the literature [82,92,93].

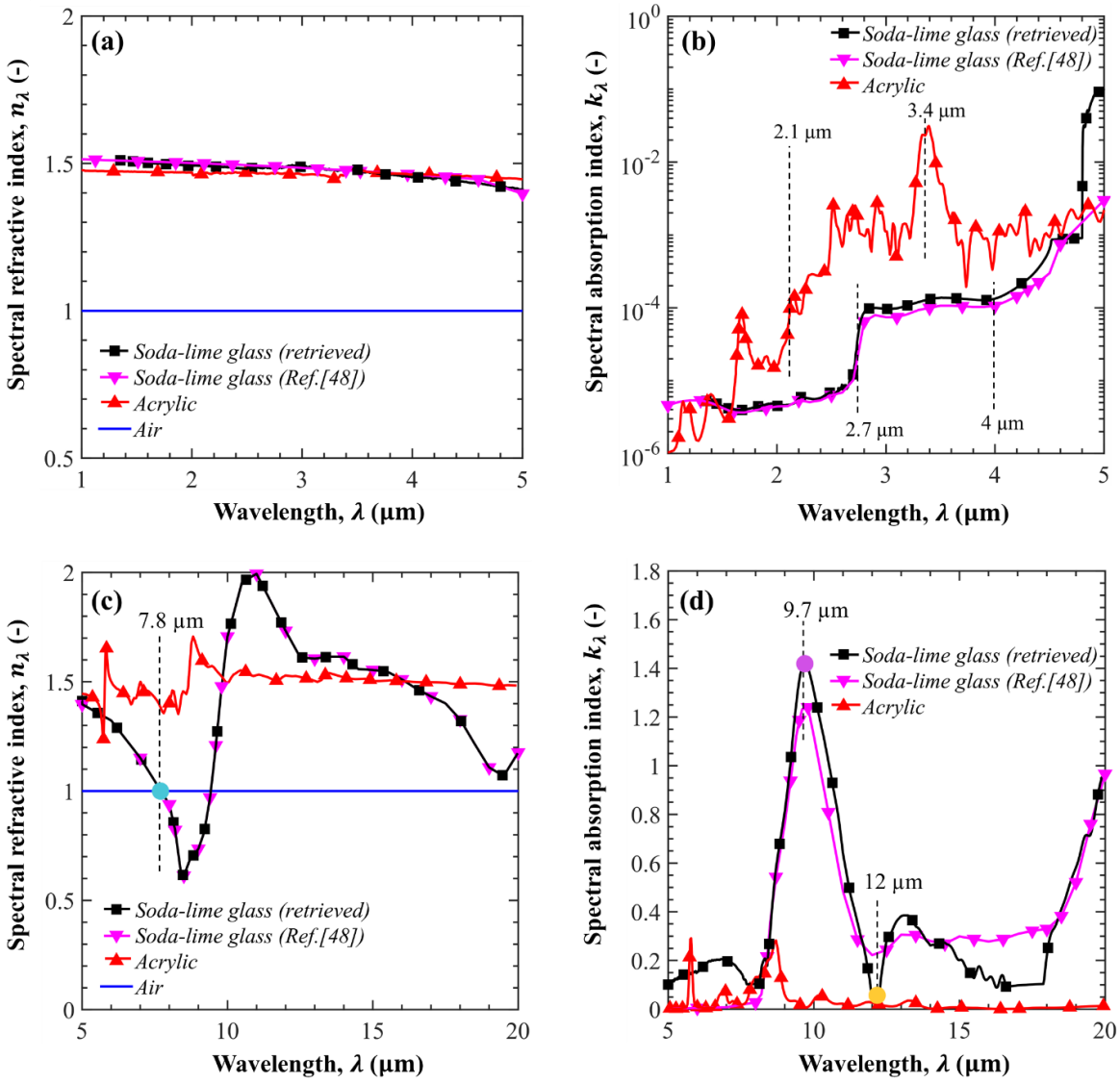

Figure 3.2. Spectral refractive n_λ and absorption indices k_λ of soda-lime glass slabs retrieved from measurements of $T_{nn,g,\lambda}$ and $R_{nn,g,\lambda}$ and those taken from Ref.[80] as well as those of acrylic in the spectral range between (a, b) 1.35 and 5 μm and (c, d) 5 and 20 μm.

The refractive and absorption indices of the air were taken as n_a = 1.0 and k_a = 0, respectively. As a reference, the refractive $n_{g,\lambda}$ and absorption $k_{g,\lambda}$ indices of the clear soda-lime glass reported in Ref.[80] were also plotted. The retrieved refractive and absorption indices ($n_{g,\lambda}$, $k_{g,\lambda}$) of the glass window used in this chapter were in good agreement with those reported in the literature [80]. The

slight difference can be attributed to the difference in the glass composition and in particular in the iron content [85].

3.3.4 Method of solution

The numerical predictions of the spectral normal-hemispherical transmittance $T_{nh,\lambda}$ and reflectance $R_{nh,\lambda}$ of glass slabs covered with absorbing droplets on their back or front sides were obtained using the MCRT method described in detail in Refs.[64,66]. To ensure numerical convergence, 10^7 photon bundles for each numerical simulation were traced until they were counted as reflected, transmitted, or absorbed by the simulated sample.

3.4 Results and discussion

3.4.1 Back side condensation

3.4.1.1. Spectral normal-hemispherical transmittance and reflectance

Figure 3.3 shows the spectral normal-hemispherical transmittance $T_{nh,\lambda}$ and reflectance $R_{nh,\lambda}$ measured between 1.35 and 5 μm for glass slabs either dry or supporting acrylic droplets on their *back side* with (a, b) droplet mean contact angle $\bar{\theta}_c$ = 25.8° and surface area coverage f_A = 40, 49, and 59% (Samples 1, 2, 3) and (c, d) droplet mean contact angle $\bar{\theta}_c$ = 76.2° and surface area coverage f_A = 19, 34, and 45% (Samples 7, 8, 9). It is evident that the presence of droplets with low contact angle did not affect the spectral normal-hemispherical transmittance $T_{nh,\lambda}$ for wavelengths λ < 2.1 μm when the droplet absorption index $k_{d,\lambda}$ was small [Figure 3.2(b)]. These results corroborate the findings of previous analytical studies [55,66,67] which established that transmittance and reflectance are unaffected by the presence of pendant droplets when their contact angle θ_c is smaller than the critical angle for total internal reflection at the droplet/air interface defined as $\theta_{cr} = \sin^{-1}(n_a/n_d) \approx 42.2°$ [81].

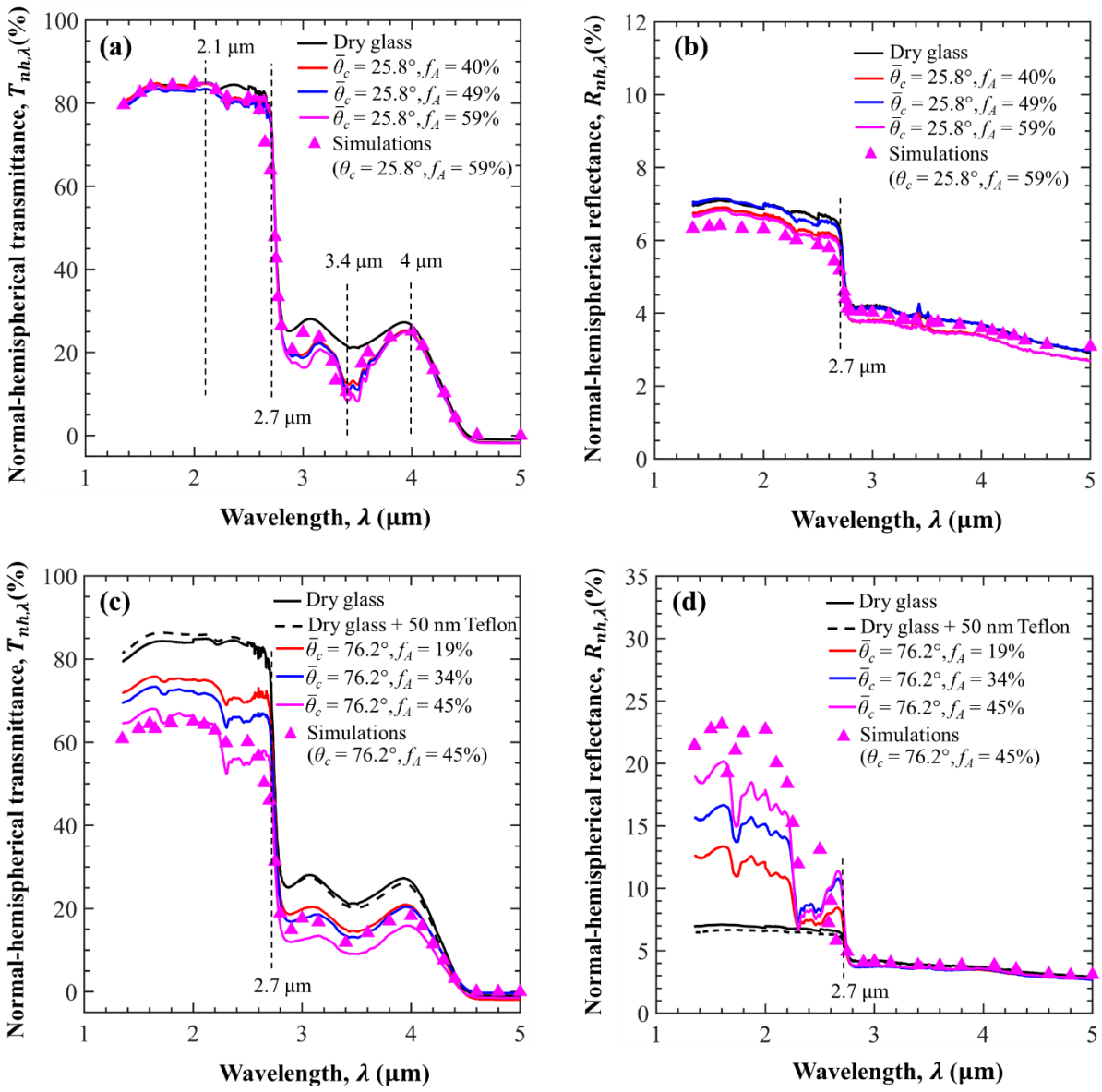

Figure 3.3. Spectral normal-hemispherical transmittance $T_{nh,\lambda}$ and reflectance $R_{nh,\lambda}$ as functions of wavelength λ for dry glass and glass slabs supporting droplets on their back side with (a, b) contact angle $\bar{\theta}_c$ = 25.8° and surface area coverage f_A = 40, 49, and 59% (Samples 1, 2, 3) and (c, d) contact angle $\bar{\theta}_c$ = 76.2° and surface area coverage f_A = 19, 34, and 45% (Samples 7, 8, 9).

For the same reasons, Figure 3.3(b) also shows that the reflectance $R_{nh,\lambda}$ was unaffected by droplets with $\bar{\theta}_c$ = 25.8° at all wavelengths. In fact, all droplet-covered samples had similar reflectance as the dry sample.

Furthermore, Figure 3.3(a) indicates that the presence of droplets decreased the spectral normal-hemispherical transmittance $T_{nh,\lambda}$ at wavelengths λ = 2.1 - 4 μm for the different surface area coverages f_A considered. This was attributed to the absorption of the radiation by the droplets since the acrylic droplets were strongly absorbing in this spectral range, as shown in Figure 3.2(b). In addition, the transmittance $T_{nh,\lambda}$ and reflectance $R_{nh,\lambda}$ of the dry and droplet-covered glass slabs decreased sharply at λ = 2.7 μm due to the sharp shoulder in the absorption index $k_{g,\lambda}$ of the soda-lime glass from 10^{-5} to 10^{-4} around 2.7 μm [Figure 3.2(b)] corresponding to Si-OH stretching vibration [94].

Similarly, the normal-hemispherical transmittance $T_{nh,\lambda}$ of the droplet-covered glass slabs reached a local minimum at λ = 3.4 μm due to the peak in the absorption index of acrylic. However, for wavelengths λ > 4 μm, the presence of droplets did not affect the spectral normal-hemispherical transmittance $T_{nh,\lambda}$. This can be attributed to the fact that only a relatively small fraction of incident photons reached the back side of the glass slab due to its strong absorption index at λ > 4 μm. The few photons reaching the droplets did not experience back-scattering due to the small droplet contact angle ($\bar{\theta}_c < \theta_{cr}$). In fact, the normal-hemispherical transmittance $T_{nh,\lambda}$ of all samples vanished for $\lambda \geq$ 4.8 μm, as the glass absorption index $k_{g,\lambda}$ further increased. Figures 3.3(a) and 3.3(b) also compare the measured and numerically predicted spectral normal-hemispherical transmittance $T_{nh,\lambda}$ and reflectance $R_{nh,\lambda}$ of Sample 3 ($\bar{\theta}_c$ = 25.8°, f_A = 59%), respectively. They indicate that the numerical predictions were in good agreement with experimental measurements of $T_{nh,\lambda}$ and $R_{nh,\lambda}$ across the entire spectral range considered.

By contrast, Figures 3.3(c) and 3.3(d) establish that, for droplet contact angle $\bar{\theta}_c$ = 76.2°, $T_{nh,\lambda}$ decreased and $R_{nh,\lambda}$ increased significantly with increasing surface area coverage f_A for λ < 2.7 μm. This was attributed to total internal reflection at the droplet/air interface since the droplet contact

angle was larger than the critical angle, i.e., $\bar{\theta}_c \geq \theta_{cr} \approx 42.2°$ and the glass did not absorb significantly ($k_{g,\lambda} \leq 10^{-5}$). However, for $\lambda > 2.7$ μm, increasing the droplet surface area coverage f_A had a negligible effect on the normal-hemispherical reflectance $R_{nh,\lambda}$ while the transmittance $T_{nh,\lambda}$ still decreased with increasing f_A. This was due to the large absorption indices of glass $k_{g,\lambda}$ and acrylic $k_{d,\lambda}$ causing most photons to be absorbed by the glass window and those transmitted to be partially absorbed by the small droplets.

Moreover, Figures 3.3(c) and 3.3(d) compare the measured and simulated spectral normal-hemispherical transmittance $T_{nh,\lambda}$ and reflectance $R_{nh,\lambda}$ between 1.35 and 5 μm for Sample 9 ($\bar{\theta}_c$ = 76.2°, f_A = 45%), respectively. Both figures show relatively good agreement between measurements and numerical predictions. The discrepancies observed between the measured and predicted reflectance $R_{nh,\lambda}$ can be attributed to the fact that the MCRT simulations did not account for the 50 nm thick Teflon film coating on the back side of the glass slab. In fact, Figure 3.3 shows the measured spectral normal-hemispherical (c) transmittance $T_{nh,g,\lambda}$ and (d) reflectance $R_{nh,g,\lambda}$ of a 3 mm glass slab with and without a 50 nm thick Teflon film, respectively. They indicate that $T_{nh,\lambda}$ of the glass slab slightly increased while $R_{nh,\lambda}$ decreased due to the presence of the Teflon film for wavelengths $\lambda < 2.7$ μm. Here, the Teflon film ($n \approx 1.29$) [95] reduced the refractive index mismatch at the glass/air interface (n_g = 1.5, n_a = 1) resulting in a decrease in the glass slab reflectance [90]. Thus, by ignoring the Teflon film, the MCRT simulations slightly overestimated the normal-hemispherical reflectance $R_{nh,\lambda}$ of Sample 9.

Figure 3.4 shows the spectral normal-hemispherical reflectance $R_{nh,\lambda}$ between 5 and 20 μm for the dry and droplet-covered glass slabs with (a) droplet mean contact angle $\bar{\theta}_c$ = 25.8° and surface area coverage f_A between 40% and 60% (Samples 1, 2, 3) and (b) $\bar{\theta}_c$ = 76.2° and f_A between 19% and 45% (Samples 7, 8, 9). Note that the spectral normal-hemispherical transmittance $T_{nh,\lambda}$ between

5 and 20 μm is not shown since it vanished for wavelengths $\lambda \geq 4.8$ μm beyond which the glass window was opaque ($k_{g,\lambda} \geq 10^{-3}$). First, Figure 3.4(a) indicates that the spectral normal-hemispherical reflectance of the dry glass $R_{nh,g,\lambda}$ initially decreased with increasing wavelength λ. $R_{nh,g,\lambda}$ reached zero at $\lambda = 7.8$ μm due to the absence of a refractive index mismatch at the glass/air interface, i.e., $n_{g,\lambda} = 1$ at $\lambda = 7.8$ μm, as illustrated by the blue dot in Figure 3.2(c). In addition, the reflectance $R_{nh,g,\lambda}$ of the dry glass then reached a maximum at $\lambda = 9.7$ μm before decreasing to a minimum at $\lambda = 12$ μm respectively attributed to the peak at $\lambda = 9.7$ μm (purple dot) and subsequent trough at $\lambda = 12$ μm (yellow dot) in the spectral absorption index $k_{g,\lambda}$ of the soda-lime glass slab [Figure 3.2(d)]. Figure 3.4 also indicates that, for wavelengths between 5 and 20 μm, the spectral normal-hemispherical reflectance $R_{nh,\lambda}$ of the droplet-covered glass slabs was nearly independent of droplet surface area coverage f_A regardless of the contact angle $\bar{\theta}_c$. Finally, the numerical simulations were in excellent agreement with the measurements for the dry and droplet-covered samples for both $\bar{\theta}_c = 25.8°$ and 76.2°.

3.4.1.2. Effect of droplet contact angle $\bar{\theta}_c$

Figure 3.5 shows the spectral normal-hemispherical (a) transmittance $T_{nh,\lambda}$ and (b) reflectance $R_{nh,\lambda}$ as functions of droplet contact angle $\bar{\theta}_c$ for droplet-covered glass slabs with surface area coverage $f_A \approx 48 \pm 4\%$ (Samples 2, 4-6, 9) at wavelength $\lambda = 1.6$, 2.5, and 3.4 μm. These wavelengths were selected to illustrate the effect of the absorption indices of the droplet and soda-lime glass on $T_{nh,\lambda}$ and $R_{nh,\lambda}$. The absorption index of the acrylic droplets $k_{d,\lambda}$ at wavelength $\lambda = 1.6$, 2.5, and 3.4 μm was equal to 10^{-5}, 10^{-3}, and $3\text{x}10^{-2}$ and that of the soda-lime glass $k_{g,\lambda}$ was equal to 10^{-6}, 10^{-6}, and 10^{-4}, respectively.

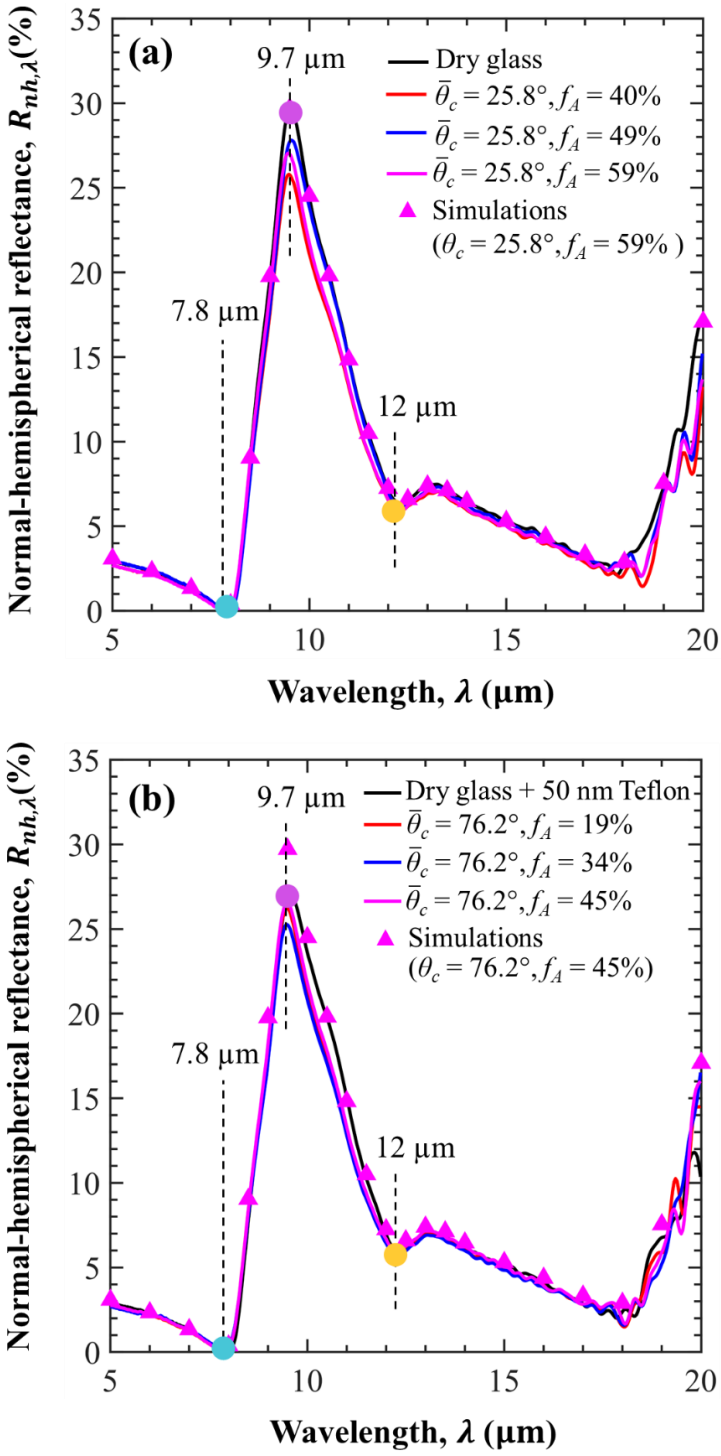

Figure 3.4. Spectral normal-hemispherical reflectance $R_{nh,\lambda}$ as a function of wavelength λ between 5 and 20 µm for dry glass and glass slabs supporting droplets on their back side with (a) contact angle $\bar{\theta}_c$ = 25.8° and surface area coverage f_A = 40, 49, and 59% (Samples 1, 2, 3) and (b) $\bar{\theta}_c$ = 76.2° and f_A = 19, 34, and 45% (Samples 7, 8, 9). In this wavelength range, $T_{nh,\lambda} = 0$.

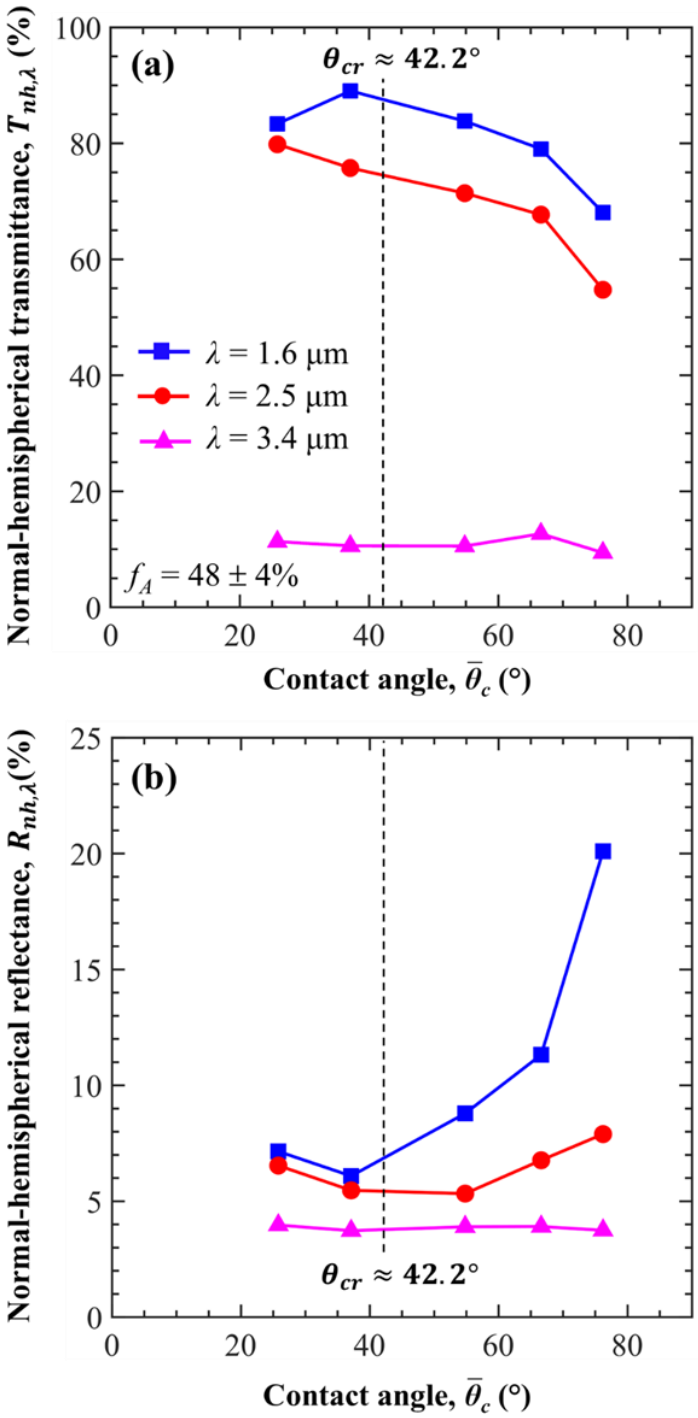

Figure 3.5. Spectral normal-hemispherical (a) transmittance $T_{nh,\lambda}$ and (b) reflectance $R_{nh,\lambda}$ as functions of contact angle $\bar{\theta}_c$ for glass slabs supporting droplets on their back side with surface area coverage $f_A \approx 48 \pm 4\%$ (Samples 2, 4-6, 9) at wavelength $\lambda = 1.6$ ($k_{d,\lambda} = 10^{-5}$, $k_{g,\lambda} = 10^{-6}$), 2.5 ($k_{d,\lambda} = 10^{-3}$, $k_{g,\lambda} = 10^{-6}$), and 3.4 μm ($k_{d,\lambda} = 3\text{x}10^{-2}$, $k_{g,\lambda} = 10^{-4}$).

First, the normal-hemispherical transmittance $T_{nh,\lambda}$ at wavelength λ = 1.6 μm decreased with increasing contact angle $\bar{\theta}_c$ for contact angle greater than the critical angle $\theta_{cr} = \sin^{-1}(n_a/n_d) \approx 42.2°$ as the droplets were weakly absorbing. Simultaneously, the normal hemispherical reflectance $R_{nh,\lambda}$ at wavelength λ = 1.6 μm increased. These observations can be attributed to total internal reflection occurring at the droplet/air interface, as discussed previously. Figure 3.5(a) also indicates that the larger droplet absorption index $k_{d,\lambda}$ at wavelength λ = 2.5 μm caused the normal hemispherical-transmittance $T_{nh,\lambda}$ to decrease with increasing droplet contact angle $\bar{\theta}_c$ even before reaching the critical angle θ_{cr}. On the other hand, the corresponding reflectance $R_{nh,\lambda}$ increased only slightly. This can be attributed to absorption by the droplets whose volume increased with increasing contact angle. Total internal reflection at the droplet/air interface also contributed to the increase in $R_{nh,\lambda}$ and the associated decrease in $T_{nh,\lambda}$ at λ = 2.5 μm for contact angles $\bar{\theta}_c > \theta_{cr}$. Finally, the normal-hemispherical transmittance $T_{nh,\lambda}$ and reflectance $R_{nh,\lambda}$ at λ = 3.4 μm of the droplet-covered glass slabs remained constant and independent of droplet contact angle $\bar{\theta}_c$ when the glass window was strongly absorbing and only a small fraction of photons reached the droplets.

3.4.1.3. Effect of droplet surface area coverage f_A

Figure 3.6 shows the spectral normal-hemispherical (a) transmittance $T_{nh,\lambda}$ and (b) reflectance $R_{nh,\lambda}$ as functions of surface area coverage f_A for dry and droplet-covered glass slabs with mean contact angle $\bar{\theta}_c$ = 76.2° (Samples 7, 8, 9) at λ = 1.6, 2.5, and 3.4 μm. First, the normal-hemispherical transmittance $T_{nh,\lambda}$ decreased with increasing surface area coverage f_A at all wavelengths considered. This was attributed to total internal reflection at the droplet/air interface at λ = 1.6 μm and to absorption by the droplets and the glass slab at λ = 3.4 μm.

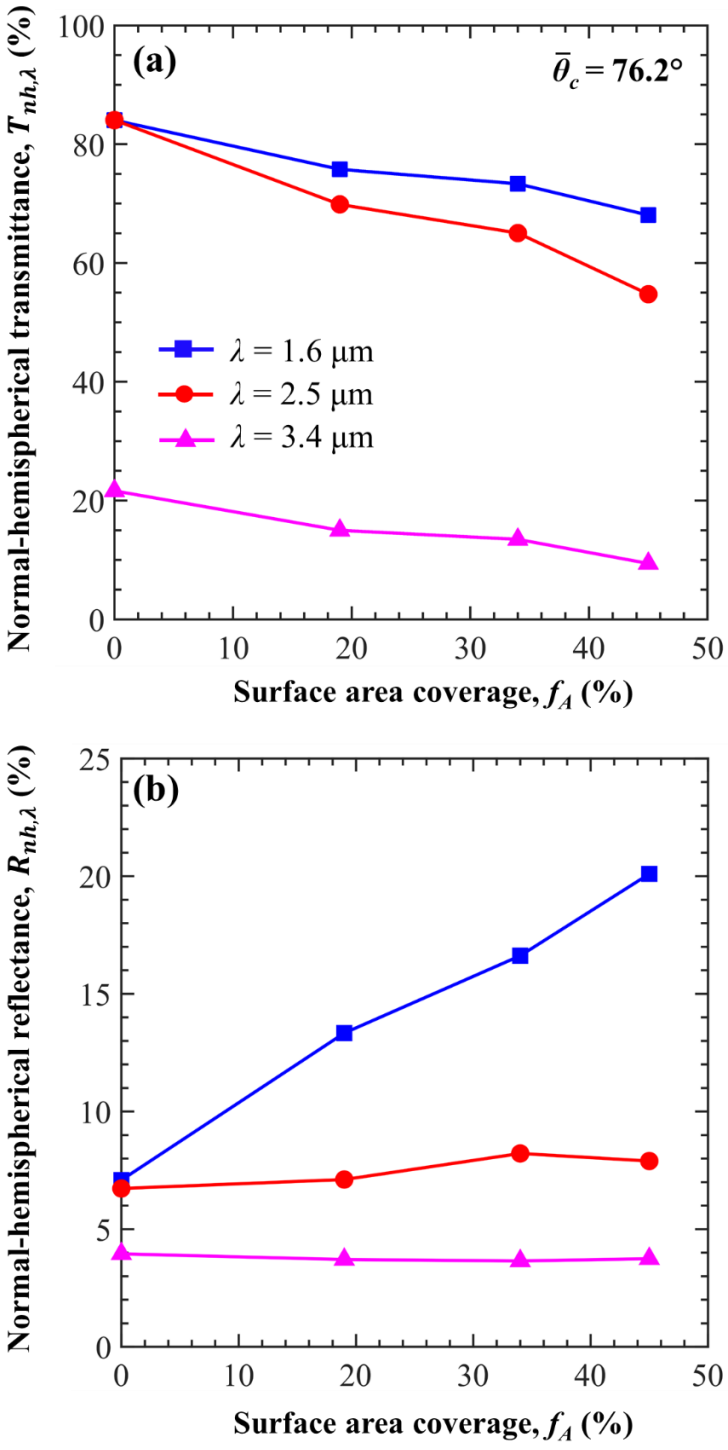

Figure 3.6. Spectral normal-hemispherical (a) transmittance $T_{nh,\lambda}$ and (b) reflectance $R_{nh,\lambda}$ as functions of surface area coverage f_A for glass slabs supporting droplets on their back side with mean contact angle $\bar{\theta}_c$ = 76.2° (Samples 7, 8, 9) at λ = 1.6 ($k_{d,\lambda}$ = 10^{-5}, $k_{g,\lambda}$ = 10^{-6}), 2.5 ($k_{d,\lambda}$ = 10^{-3}, $k_{g,\lambda}$ = 10^{-6}), and 3.4 μm ($k_{d,\lambda}$ = 3x10^{-2}, $k_{g,\lambda}$ = 10^{-4}).

The steepest decrease in transmittance with increasing f_A was observed at λ = 2.5 μm as both total internal reflection and droplet absorption occurred. Moreover, Figure 3.6(b) indicates that, at λ = 1.6 μm when droplets were weakly absorbing, the reflectance $R_{nh,\lambda}$ increased almost linearly with increasing surface area coverage f_A thanks to total internal reflection at the droplet/air interface. On the other hand, at λ = 3.4 μm when the glass was strongly absorbing, $R_{nh,\lambda}$ remained constant and independence of surface area coverage f_A. At λ = 2.5 μm when the glass slab was weakly absorbing and the droplets slightly absorbing, $R_{nh,\lambda}$ remained constant and independent of f_A. This can be attributed to the fact that photons were absorbed by either the glass window or the droplets after being refracted at the glass/air interface or backscattered at the droplet/air interface.

3.4.2 Front side condensation

3.4.2.1 Spectral normal-hemispherical transmittance and reflectance

Figure 3.7 shows the spectral normal-hemispherical transmittance $T_{nh,\lambda}$ and reflectance $R_{nh,\lambda}$ between 1.35 and 5 μm for the dry and droplet-covered glass slabs featuring droplets on their *front side* with (a, b) mean contact angle $\bar{\theta}_c$ = 25.8° and surface area coverage f_A = 40%, 49%, and 59% (Samples 1, 2, 3) and (c, d) mean contact angle $\bar{\theta}_c$ = 76.2° and surface area coverage f_A = 19, 34, and 45% (Samples 7, 8, 9).

For droplet mean contact angle $\bar{\theta}_c$ = 25.8°, the normal-hemispherical transmittance $T_{nh,\lambda}$ slightly increased while the normal-hemispherical reflectance $R_{nh,\lambda}$ decreased in the presence of droplets for wavelengths λ < 2.1 μm. These trends were amplified for droplets with droplet mean contact angle $\bar{\theta}_c$ = 76.2° [Figures 3.7(c) and 3.7(d)]. These observations were due to the fact that droplets had an antireflection effect by reducing the refractive index mismatch at the air/droplet interface (n_a = 1, n_d = 1.47) compared to that at the air/glass interface (n_a = 1, n_g = 1.51).

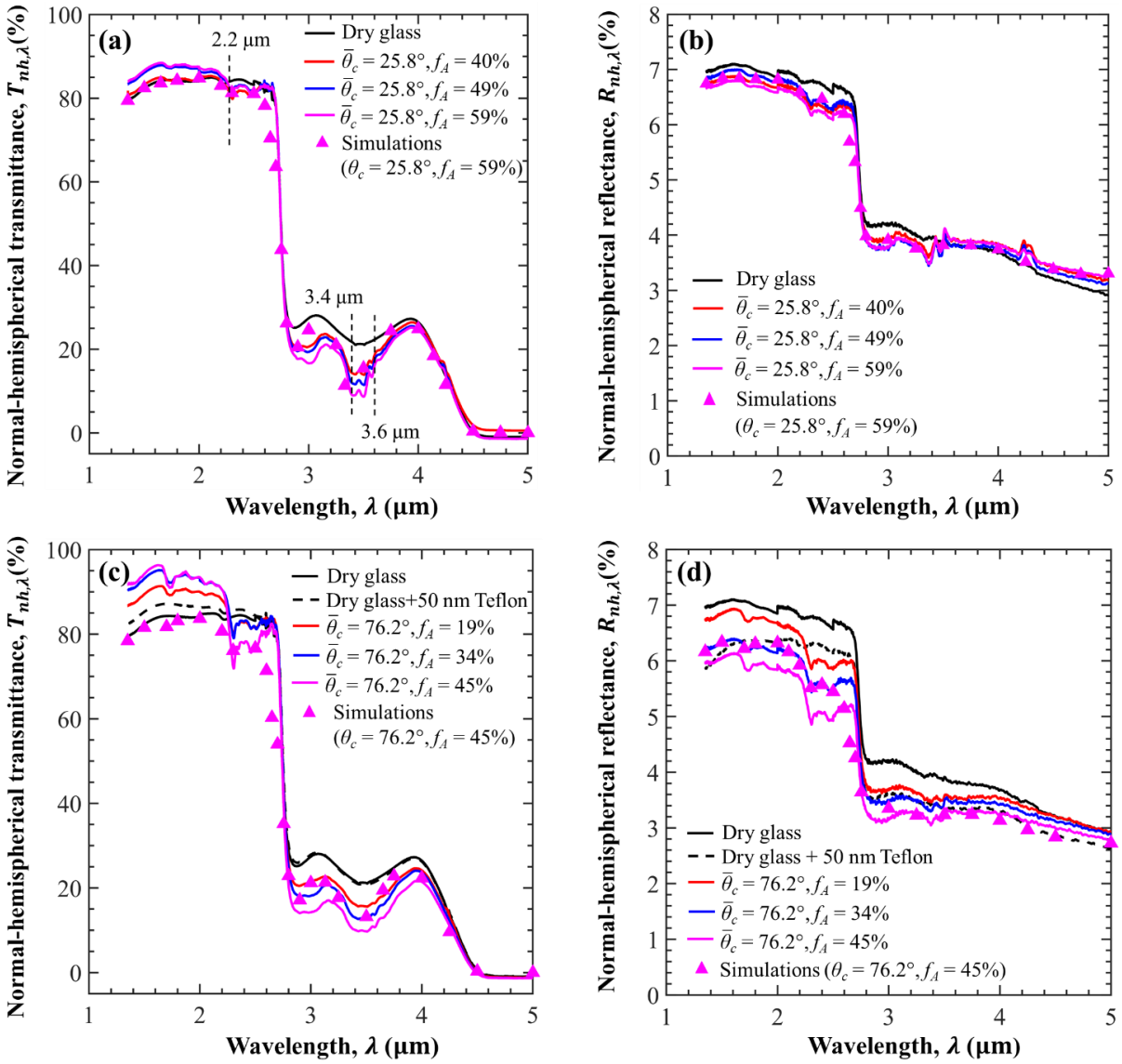

Figure 3.7. Spectral normal-hemispherical transmittance $T_{nh,\lambda}$ and reflectance $R_{nh,\lambda}$ as functions of wavelength λ for dry glass and glass slabs supporting droplets on their front side with (a, b) mean contact angle $\bar{\theta}_c$ = 25.8° and surface area coverage f_A = 40, 49, and 59% (Samples 1, 2, 3) and (c, d) $\bar{\theta}_c$ = 76.2° and f_A = 19, 34, and 45% (Samples 7, 8, 9).

Moreover, Figures 3.7(a) and 3.7(c) indicate that the transmittance $T_{nh,\lambda}$ decreased with increasing surface area coverage f_A for wavelengths between 2.1 - 4 μm due to absorption by the

droplets for both contact angles considered. In fact, transmittance $T_{nh,\lambda}$ featured ripples between 3.4 - 3.6 μm similar to those observed in the spectral absorption index $k_{d,\lambda}$ of acrylic plotted in Figure 3.2(b). Similarly, the Teflon film coating on the front side acted as an anti-reflective coating ($n \approx 1.29$). In fact, the presence of 50 nm Teflon film on the dry glass window increased its normal-hemispherical transmittance and decreased its reflectance, particularly for wavelengths less than 2.7 μm. In addition, the increase in the normal-hemispherical transmittance $T_{nh,\lambda}$ for wavelengths $\lambda < 2.1$ μm was more pronounced for Samples 7-9 than for Samples 1-3 due to the presence of the Teflon film. Note that, for wavelengths beyond 2.7 μm, reflectance $R_{nh,\lambda}$ remained nearly independent of surface area coverage f_A for contact angle $\bar{\theta}_c = 25.8°$ as shown in Figure 3.7(b). It decreased only so slightly for $\bar{\theta}_c = 76.2°$ [Figure 3.7(d)].

Finally, Figures 3.7(a) and 3.7(b) establish that the numerical predictions were in very good agreement with the experimental measurements for the spectral normal-hemispherical transmittance $T_{nh,\lambda}$ and reflectance $R_{nh,\lambda}$ of Sample 3 ($\bar{\theta}_c = 25.8°$ and $f_A = 59\%$) across the IR spectrum considered. This further confirm the validity of the simulation tools for absorbing droplets present on the front side of a semitransparent window. Similarly, Figures 3.7(c) and 3.7(d) compare numerical predictions and experimental measurements of the normal-hemispherical transmittance $T_{nh,\lambda}$ and reflectance $R_{nh,\lambda}$ for Sample 9 ($\bar{\theta}_c = 76.2°$ and $f_A = 45\%$), respectively. The measured normal-hemispherical transmittance $T_{nh,\lambda}$ and reflectance $R_{nh,\lambda}$ were respectively larger and smaller than the numerical predictions for wavelengths $\lambda < 2.7$ μm. Here again, these discrepancies can be attributed to the presence of the Teflon coating, which was not accounted for in the MCRT simulations.

Figure 3.8 shows the spectral normal-hemispherical reflectance $R_{nh,\lambda}$ between 5 and 20 μm for the dry and droplet-covered glass slabs on their front side featuring (a) $\bar{\theta}_c = 25.8°$ and f_A between

40% and 60% (Samples 1, 2, 3), and (b) $\bar{\theta}_c$ = 76.2° and f_A between 19% and 45% (Samples 7, 8, 9). Unlike for back side droplets [Figure 3.4], the normal-hemispherical reflectance $R_{nh,\lambda}$ for front side droplets decreased significantly with increasing f_A for wavelengths between 8 and 15 μm due to the droplets antireflecting effect. In addition, $R_{nh,\lambda}$ for samples with droplet contact angle $\bar{\theta}_c$ = 76.2° further decreased due to the presence of the Teflon film and its additional antireflecting effect. Finally, Figure 3.8 shows good agreements between measurements and numerical predictions of reflectance $R_{nh,\lambda}$.

3.4.3 Impact of water droplets on radiometric properties

To assess the impact of water droplets on the thermal load and radiometric properties of windows and covers used in buildings and solar energy conversion systems, the solar transmittance T_{sol} and the total hemispherical emissivity ε of the dry and glass windows covered with cap-shaped water droplets on their front or back sides were predicted for a horizontal window exposed to direct and collimated solar radiation in Los Angeles, CA, USA (latitude: 34.07° N; longitude: 118.44° W) throughout the day on June 21st. First, the solar transmittance T_{sol} can be defined as [5,96]

$$T_{sol}(\theta_z(t)) = \frac{\int_{0.3\ \mu m}^{3\ \mu m} T_{dh,\lambda}(\theta_z(t)) G_{s,\lambda}(\theta_z(t)) d\lambda}{\int_{0.3\ \mu m}^{3\ \mu m} G_{s,\lambda}(\theta_z(t)) d\lambda}. \quad (3.2)$$

Here, $\theta_z(t)$ is the time-dependent solar zenith, $T_{dh,\lambda}$ is the corresponding spectral directional-hemispherical transmittance, and $G_{s,\lambda}$ is the spectral solar irradiation (in W/m^2·μm) incident on a horizontal window for the location and day of interest taken from Ref.[97]. In order to evaluate $T_{sol}(\theta_z(t))$, the spectral directional-hemispherical transmittance $T_{dh,\lambda}$ was predicted numerically for water droplets using the previously experimentally-validated MCRT code in the visible [59] and infrared parts of the electromagnetic spectrum.

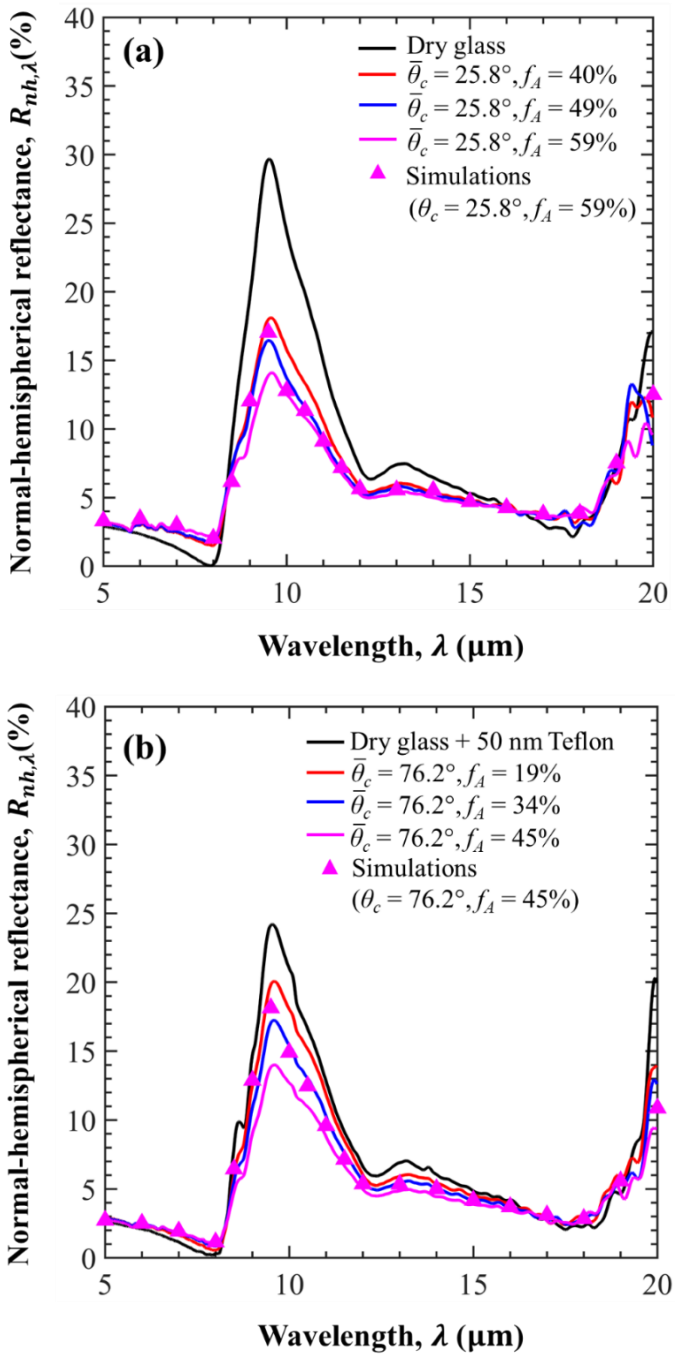

Figure 3.8. Spectral normal-hemispherical reflectance $R_{nh,\lambda}$ as a function of wavelength λ for dry glass with Teflon coating and glass slabs supporting droplets on their front side with (a) contact angle $\bar{\theta}_c$ = 25.8° and surface area coverage f_A = 40, 49, and 59% (Samples 1, 2, 3) and (b) contact angle $\bar{\theta}_c$ = 76.2° and surface area coverage f_A = 19, 34, and 45% (Samples 7, 8, 9).

The spectral range between 0.3 and 3 μm was considered because it accounts for 95% of the solar radiation. The spectral refractive and absorption indices of the soda-lime silica glass and water at this spectral range were taken from Refs.[80] and [98], respectively. In the MCRT simulations, the water droplets had the same coordinates (x, y) and projected diameters d_p as the acrylic droplets deposited on Sample 3 with surface area coverage f_A = 59% in order to simulate a realistic droplet size distribution and surface area coverage f_A.

Figure 3.9 plots the hourly solar transmittance T_{sol} calculated from the spectral directional-hemispherical transmittance $T_{dh,\lambda}(t)$ (see Appendix B.2) for dry and droplet-covered glass windows supporting water droplets on their (a) back side and (b) front side with droplet contact angle θ_c = 30°, 60°, and 90°, and surface area coverage f_A = 59% on June 21st in Los Angeles, CA. The solar transmittance of the glass windows decreased by up to 26% due to the presence of droplets on their back side for contact angles θ_c = 60° and 90° because of total internal reflection at the droplet/air interface and absorption by the water droplets. Note that, the solar transmittance T_{sol} remained unchanged between 11 AM and 3 PM in the presence of droplets with θ_c = 30°. This can be explained by the fact that during this time, solar incident angles were near-normal ($\theta_i \leq 30°$) and the droplet contact angle θ_c was smaller than the critical angle $\theta_{cr} \approx 48.8°$ [81].

For glass windows supporting droplets on their front side, T_{sol} decreased by up to 43% in the presence of water droplets due to the increase in reflection and absorption by the water droplets between 7 AM and 11 AM and from 3 PM to 7 PM. Here also, T_{sol} remained unchanged in the presence of water droplets between 11 AM and 3 PM due to the near-normal solar zenith angles ($\theta_z \leq 30°$). Note that in the early morning before 7 AM and evening after 7 PM when the solar radiation was incident at angles $\theta_z > 80°$, the glass windows supporting water droplets on their front side featured a larger solar transmittance T_{sol} than the dry glass window as the water droplets

scattered the photons back towards the glass window [64]. Moreover, for θ_c = 90°, the solar transmittance T_{sol} reached a minimum at t = 6:30 PM and then increased with increasing time until it reached a peak at t = 7:30 PM. This can be attributed to the decrease in total internal reflection at the back glass window/air interface and to the increase in total internal reflection at the water droplet/air interfaces [62,64]. These results establish that the presence of water droplets on the back or front side of the glass windows can significantly reduce the solar transmittance T_{sol} at different times of the day and thereby the energy input and efficiency of solar energy conversion systems. In addition, hydrophilic coatings should be preferred to minimize the effect of droplets. However, note that most of the previous studies on the thermal modeling of solar energy conversion systems such as solar stills [99] and greenhouses [100] have not considered the presence of droplets and the hourly change in the solar transmittance of the cladding covered with droplets.

Moreover, the above-mentioned systems operate at temperatures between 280 and 320 K and emit thermal radiation at infrared wavelengths that affect the thermal load on these systems. For an opaque medium, the spectral normal emissivity $\varepsilon_{n,\lambda}$ given by Kirchhoff's law [5,101]

$$\varepsilon_{n,\lambda} = \alpha_{n,\lambda} = 1 - R_{nh,\lambda} \tag{3.3}$$

where $\alpha_{n,\lambda}$ is the spectral normal absorptance. The total hemispherical emissivity ε does not differ considerably from the total normal emissivity ε_n for dielectric materials [29], therefore ε can be calculated as [5,46]

$$\varepsilon \approx \varepsilon_n = \frac{\int_{5\ \mu m}^{50\ \mu m} \varepsilon_{n,\lambda} E_{b,\lambda}(T_o) d\lambda}{\int_{5\ \mu m}^{50\ \mu m} E_{b,\lambda}(T_o) d\lambda}. \tag{3.4}$$

Here, $E_{b,\lambda}(T_o)$ is the blackbody spectral emissive power (in W/m^2·μm) at temperature T_o = 296 K. Note that the integrals in both the numerator and denominator of Equation (3.4) were truncated to wavelengths between 5 - 50 μm spectral range where 96% of their emissive power $E_{b,\lambda}(T_o)$ is

concentrated and as the glass window was opaque for $\lambda \geq 4.8$ μm. The validation of this approach is presented in Appendix B.

Figure B.3(c) in Appendix plots the total hemispherical emissivity ε [Equation (3.4)] as a function of droplet contact angle θ_c for water droplet-covered glass windows with surface area coverage f_A = 59%. It indicates that the total hemispherical emissivity ε of the glass window remained unchanged (see Figure B.3(a)) in the presence of water droplets on the back side. This was due to the fact that the glass window was strongly absorbing in this spectral range and photons did not reach the droplets. By contrast, total hemispherical emissivity ε increased slightly in the presence of water droplets on the front side from 0.93 for surface area coverage f_A = 0% to 0.96 for surface area coverage f_A = 59%. This can be attributed to the (i) antireflecting effect and (ii) absorption of the IR radiation by the water droplets.

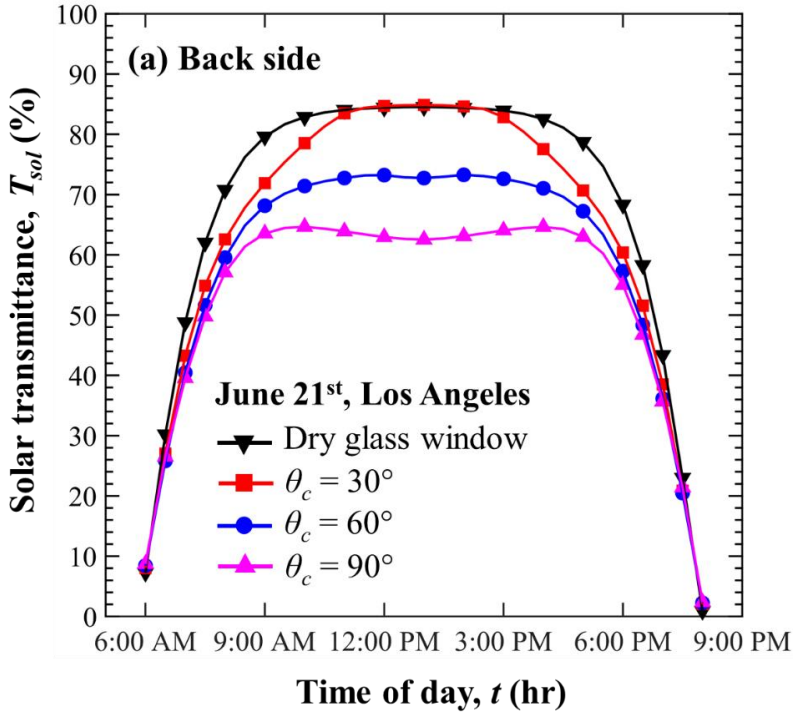

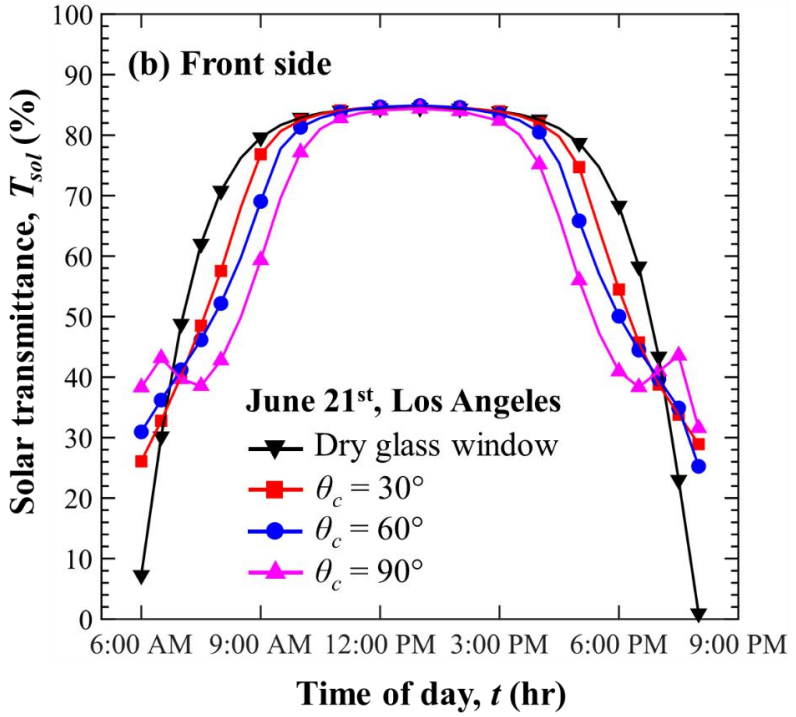

Figure 3.9. Solar transmittance T_{sol} as a function of time t for a horizontal glass window supporting polydisperse cap-shaped water droplets on its (a) back side and (b) front side for droplet contact angle θ_c = 30°, 60°, and 90°, and surface area coverage f_A = 59% on June 21st, in Los Angeles, CA.

3.5 Conclusion

Radiation transfer through glass windows supporting droplets on their back side was controlled by absorption by the droplets and/or the glass window and by total internal reflection at the droplet/air interface. More specifically, when the droplets and the glass window were slightly absorbing, the spectral normal-hemispherical transmittance $T_{nh,\lambda}$ was independent of droplet surface area coverage f_A and increased slightly with increasing droplet contact angle $\bar{\theta}_c$ smaller than the critical angle θ_{cr} for total internal reflection. However, for droplet contact angles $\bar{\theta}_c \geq \theta_{cr}$, the normal-hemispherical transmittance $T_{nh,\lambda}$ decreased with increasing contact angle $\bar{\theta}_c$ and surface area coverage f_A due to total internal reflection at the droplet/air interface. Moreover, when the droplets were strongly absorbing and the glass was weakly absorbing, the spectral normal-hemispherical transmittance $T_{nh,\lambda}$ decreased with increasing droplet surface area coverage f_A and contact angle $\bar{\theta}_c$ due to absorption by both the glass and the droplets. Finally, when the glass window was strongly absorbing, the spectral normal hemispherical transmittance $T_{nh,\lambda}$ vanished and the spectral normal hemispherical reflectance $R_{nh,\lambda}$ was independent of surface area coverage f_A and contact angle $\bar{\theta}_c$ as the radiation was reflected by the surface of the glass window and did not reach the droplets.

Radiation transfer through glass windows supporting droplets on their front side was affected by the antireflecting effects of droplets which reduced the index mismatch between the window and the air as well as by absorption by the droplets and/or the glass window. More specifically, when the droplets and the glass window were slightly absorbing, the spectral normal-hemispherical transmittance $T_{nh,\lambda}$ increased while the reflectance $R_{nh,\lambda}$ decreased with increasing surface area coverage f_A. Moreover, when the droplets were strongly absorbing and the glass was weakly absorbing, the spectral normal-hemispherical transmittance $T_{nh,\lambda}$ of glass windows supporting droplets on their front side decreased with increasing droplet surface area coverage f_A and contact

angle $\bar{\theta}_c$. Finally, when the glass window was strongly absorbing, the transmittance $T_{nh,\lambda}$ vanished and the reflectance $R_{nh,\lambda}$ decreased with increasing droplet surface area coverage f_A.

The experimental results were successfully validated both qualitatively and quantitatively by predictions from numerical simulations based on Monte Carlo ray-tracing method [64,66] for both droplets on the back and front sides of glass windows. The experimentally-validated numerical simulation tool was used to predict the hourly solar transmittance and total hemispherical emissivity of horizontal glass windows supporting cap-shaped water droplets on their back or front side in Los Angeles, CA on June 21. In the presence of droplets on the back side, the solar transmittance of the glass window decreased by up to 26% for most of the day while the total hemispherical emissivity remained unchanged. However, for droplets on the front side, solar transmittance decreased by up to 40% in the morning and evening while the total hemispherical emissivity increased slightly. These results will be useful in selecting cover materials and surface coatings to improve and model the solar energy conversion systems.

Chapter 4: Effect of Dew and Rain on Photovoltaic Solar Cell Performances

This chapter investigates experimentally the impact of droplets on the performance of solar photovoltaic (PV) cells due to dropwise condensation or rain falling on their cover. Dew formation occurs frequently in various climates including in semi-arid regions suitable to PV cell deployment. Then, droplets present on the cover of solar cells can negatively affect the cell power generation and efficiency due to optical effects. Here, semi-transparent glass covers were prepared without or with surface treatments and covered with acrylic droplets with contact angle ranging between 25° and 77° and surface area coverage between 19% and 49%. The results of this chapter highlight the importance of selecting durable hydrophilic solar cell cover.

4.1 Background

Outdoor PV solar panels are exposed to elements including dust, rain, and/or dew that can reduce their efficiency, power output, and lifetime [102–105]. The adverse effect of soiling by dust on solar cell performance has been widely documented [106–110]. Jiang et al.[106] showed experimentally that the conversion efficiency of amorphous silicon PV cells can be reduced by 26% for a dust deposition density of 22 g/m^2 of PV cell under normally incident irradiance of 760 W/m^2 supplied by a solar simulator. Pavan et al.[107] compared the power output of polycrystalline silicon PV cells built on either sandy (more dusty) or compact (less dusty) soils. The power output losses, compared with clean PV cells, were 6.9% and 1.1% for sandy and compact soil sites, respectively. In addition, a few studies considered the effect of rainfall on the dust-covered PV solar cell performance [108–110]. These studies showed that rain helps wash off

the dust accumulated on the cells and thus improves their performance compared with the dust-covered PV solar cells [108–110].

To the best of our knowledge, only a few studies have investigated the effect of dropwise condensation on the performance of PV cells [27,39,111,112]. Ilse et al.[39] reported frequent dew formation on the surface of outdoor PV modules in arid regions with high concentrations of airborne dust. The presence of dew was found to increase dust and particle adhesion onto the surface of the PV cells and thus reduce their performance and increase maintenance costs. Figgis et al.[112] also demonstrated experimentally that dew formed on soiled PV modules even when the PV module surface temperature was higher than the dew point temperature. This was attributed to the fact that hygroscopic materials such as salt, nitrate, and sulfate found in the dust particles serve as nucleation sites for dropwise condensation of atmospheric water vapor. The power output of the PV solar cells was also shown to decrease under high relative humidity weather conditions due to the scattering of solar radiation by the water vapor in the atmosphere and by condensed droplets formed on the solar cell surface [113].

Hosseini et al.[29] investigated experimentally the effect of dew formation on the performance of monocrystalline and polycrystalline silicon solar cells. LEDs were used to provide radiation between 400 and 1,100 nm with total irradiation up to 309 W/m^2 under normal incidence onto horizontal solar cells. Humidifier and heater/cooler units were used to regulate the humidity and temperature of the air in the test chamber. The relative humidity was varied from 45 to 75%. The chamber temperature was imposed above the dew point temperature of 25 °C to study dry solar cells and (ii) below 25 °C to investigate solar cells covered with droplets with surface area coverage ranging between 45-84%. The maximum power output of the module was found to increase by 3.5% and 7% in the presence of droplets at a relative humidity of 75% for monocrystalline and

polycrystalline cells, respectively. This was attributed to the increase in the number of photons reaching the solar cell since the scattering of the incident radiation by water vapor in the ambient air decreased with dew formation. Finally, the maximum power decreased by about 9% for a polycrystalline solar cell as the droplet surface area coverage increased from 45% to 84% by increasing the relative humidity from 45% to 75%, respectively. Unfortunately, despite the valuable insights, the contact angle and size distribution of the droplets were not reported in this study. Also, the droplet surface area coverage could vary during the experiments due to evaporation and/or condensation. In addition, the droplet contact angle and/or surface area coverage might have been different for the monocrystalline and polycrystalline solar cells. This could explain why the percentage increase in the maximum power output of the polycrystalline solar cells was greater than the monocrystalline solar cells under the same relative humidity. Finally, all the performance metrics reported corresponded to normal incidence radiation when the effect of droplets on the transmittance of the glass cover has been shown to be relatively limited [64].

4.2 Materials and Methods

4.2.1 Materials preparation and characterization

Bare polycrystalline silicon solar cells (Aoshike, China) with a surface area of 3.8 x 3 cm^2 and a maximum power of 175 W/m^2 were used as representative of commercially available solar cells deployed in the field. Three types of solar cell assembly were tested including (1) the bare solar cell as received, (2) the solar cell covered with a clear soda-lime glass cover, and (3) the bare solar cell with a clear soda-lime glass cover without or with surface treatment and covered with acrylic droplets.

Commercial 3 mm thick plane-parallel slabs of soda-lime architectural glass with a surface area of 2.5 x 2.5 cm^2 were used as cover. The glass covers were placed on top of the bare solar cell and the rest of the solar cell was covered with opaque black tape to match the glass size. Three different surface-treatment conditions were investigated to achieve different droplet contact angles including (A) clean soda-lime glass cover, (B) soda-lime glass cover coated with a silane-treated monolayer of silica nanoparticles, and (C) soda-lime glass cover coated with Teflon AF-2400 (Chemours, USA). First, all glass covers were cleaned with isopropyl alcohol (IPA) prior to any surface treatment or droplet deposition. Before coating the glass covers with a monolayer of silane-treated silica nanoparticles, the covers were placed on a hot plate at 450 °C for 30 minutes to remove any oil, dirt, and organic residues. Silica nanoparticles with 307 ± 20 nm diameter were synthesized by the Stöber process [75,76]. The details of the silica nanoparticle synthesis are given in Appendix C. The ethanol/water-based silica nanoparticle suspension was sonicated to break down any nanoparticle aggregate. Then, the suspension was drop-casted onto the glass covers [77] to obtain a monolayer of silica nanoparticles with an arithmetic average surface roughness of 35 nm measured with Atomic Force Microscope (Bruker, Dimension FastScan). The coated glass covers were heat-treated on a hot plate at 450 °C for 1 hour to bond the nanoparticles onto the glass surface and make the coating mechanically robust. Finally, silane was deposited on top of the monolayer of silica nanoparticles by placing the glass covers inside a closed container filled with silane vapor. The silane reacted with the available hydroxyl group (OH) and permanently grafted perfluorocarbon chains on the surface of the nanoparticles and glass substrate to form a hydrophobic monolayer [74]. The third type of glass covers were spin-coated with Teflon AF-2400 followed by heat-treatment on a hot plate at 250 °C for an hour. Finally, the sample was baked in a furnace at 340 °C for 3.5 hours to achieve a 50 nm thick Teflon film [78].

Following the preparation of the glass covers without or with surface treatment, thousands of transparent acrylic droplets made of ultraviolet (UV) curable acrylic polymer (Loctite AA 349) were deposited onto the glass covers with a syringe and cured with a UV lamp at 365 nm (Blak-Ray B-100A, Thermo Scientific Fisher, USA). The use of polymer droplets instead of water droplets facilitated the handling of the solar cell assemblies and eliminated the challenges caused by the dynamic nature of dropwise condensation and water evaporation. In addition, when handling the solar cell or tilting it to simulate non-normal incidence, the water droplets would merge and/or roll off from the glass surface. Acrylic presented the benefit of being relatively viscous to avoid excessive spreading and merging among droplets during deposition over the glass substrate and was easily UV-curable without any color change. Overall, by using acrylic droplets, the surface area coverage and size distribution could be carefully characterized for each sample and remained the same throughout the experiments.

The contact angle of acrylic droplets on the glass cover was measured using a Drop Shape Analyzer (DSA100, Kruss Scientific, Germany). For each type of glass substrate, the contact angle measurements were repeated for 9 different droplets and the mean contact angle $\bar{\theta}_c$ was calculated. The projected diameter d_p and surface area coverage f_A of the droplets were measured using microscope images captured by a Leica LMIL microscope (Leica Microsystems, USA) connected to a CCD camera (Spot Insight model 4.2, USA). The image analysis software ImageJ was used in manual mode to measure the location and projected diameter of a large number of droplets.

Figure 4.1(a) schematically shows a solar cell with a semi-transparent glass cover supporting droplets along with the geometric parameters characterizing the droplets. The acrylic droplets had a refractive index n_d of about 1.49 in the visible [79] falling between that of air (n_a = 1) and that of soda-lime glass ($n_g \approx 1.53$) [80]. Thus, the optical effects caused by the presence of the acrylic

droplets are expected to be qualitatively similar to that of water droplets despite the difference in their refractive indices (1.49 vs. 1.33). Indeed, our previous study [64] established that the directional-hemispherical transmittance of glass cover supporting droplets with contact angle θ_c = 90° and surface area coverage f_A = 50% followed the same trends and was quantitatively similar for droplets with refractive index n_d equal to 1.33 or 1.5, as illustrated in Figure C.1. The polycrystalline silicon solar cells had a refractive index n_c of about 3.90 and absorption index k_c of about 0.03 in the visible [114]. Figure 4.1(b) shows a side view of the acrylic droplets with droplet mean contact angle $\bar{\theta}_c$ = 76.2°. Finally, Figures 4.1(c) and 4.1(d) present the photograph and microscope image of the Teflon-coated semi-transparent glass cover with acrylic droplets with droplet mean contact angle $\bar{\theta}_c$ = 76.2° and surface area coverage f_A = 45%.

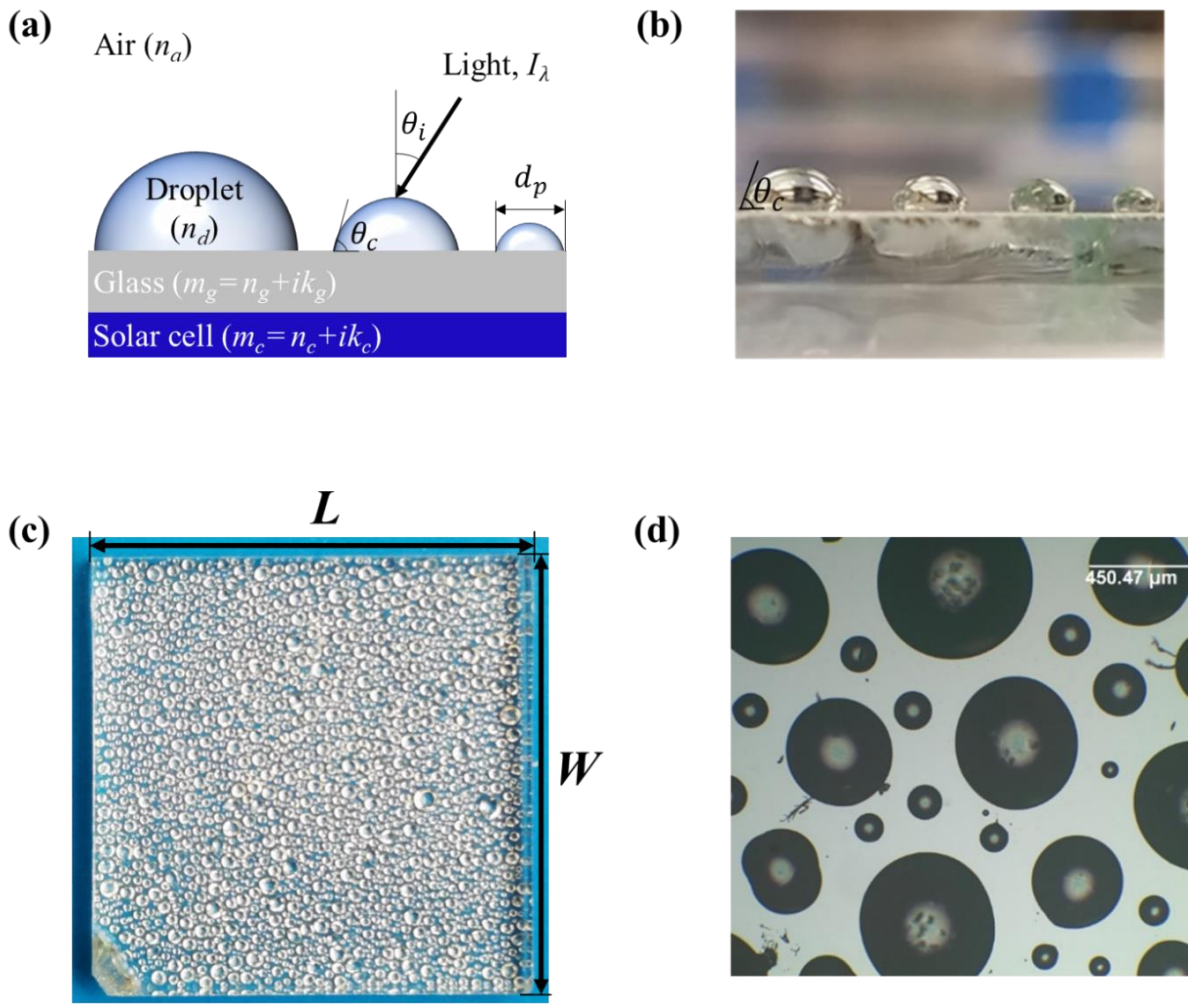

Figure 4.1. (a) Schematic of a solar cell with a semi-transparent glass cover supporting transparent polydisperse droplets, (b) side view photograph of acrylic droplets with mean contact angle $\bar{\theta}_c$ = 76.2°, (c) photograph, and (d) microscope image of the Teflon AF-2400 coated semi-transparent glass cover with acrylic droplets with droplet mean contact angle $\bar{\theta}_c$ = 76.2° and surface area coverage f_A = 45%.

4.2.2 Solar cell performance characterization

Figures 4.2(a) and 4.2(b) show the experimental setup consisting of (i) a polycrystalline silicon solar cell assembly mounted on (ii) a goniometer (OptoSigma, USA) with a custom made sample holder, (iii) a solar simulator (TriSol TS-300, OAI, USA) providing collimated simulated solar

radiation in the wavelength range between 400 and 1,100 nm with total radiation flux incident on a surface perpendicular to the collimated simulated radiation of S_c = 1 kW/m^2, and (iv) a potentiostat (BioLogic VSP-300, France) used to collect the current vs. voltage curves (*i*-*V* curves) of the different solar cell assemblies investigated under different angles of incidence.

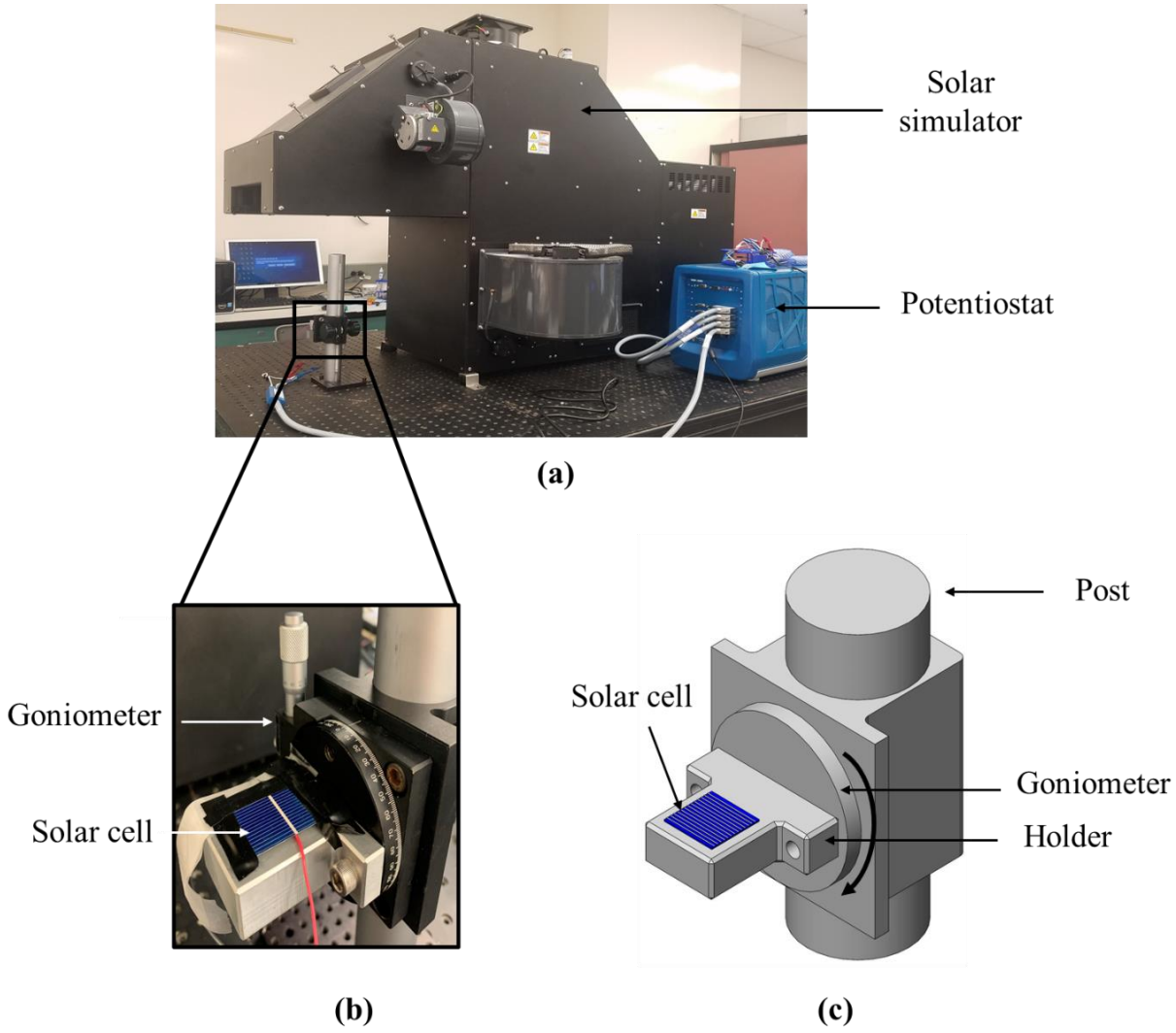

Figure 4.2. (a) Photograph of the experimental setup with the solar simulator (TriSol TS-300, OAI, USA) and the sample holder, (b) goniometer supporting a polycrystalline silicon solar cell assembly, and (c) detailed schematic of the goniometer stage.

Figure 4.2(c) shows the detailed schematic of the goniometer stage and of the sample holder used to vary the incident angle θ_i of the simulated solar radiation. Before any measurement, each solar cell assembly was securely taped flat onto the sample holder.

Finally, two metrics were considered to assess the performance of any given solar cell assembly namely (a) the maximum power P_{max} and (ii) the energy conversion efficiency η defined as [101]

$$P_{max} = Max(iV) \qquad \text{and} \qquad \eta = \frac{P_{max}}{G_s}. \tag{4.1}$$

Here, G_s is the solar irradiation incident on the PV cell at incident angle θ_i and expressed as $G_s = S_c\cos\theta_i$. The solar cell temperature remained constant at near room temperature (~ 22 ^oC) throughout the experiments. In fact, the *i-V* curve for the bare solar cell was recorded regularly to verify that the solar cell temperature and incident simulated solar irradiation remained constant throughout the experiment, as documented in Figure C.2 in Appendix.

4.3 Results and discussion

4.3.1 Droplet characterization

The different glass covers were characterized in our previous study [90]. Table 4.1 summarizes the mean contact angle $\bar{\theta}_c$ and surface area coverage f_A for the seven different solar cell assemblies tested under simulated solar irradiation G_s with incident angle θ_i varying between 0 (normal incidence) and 85^o corresponding to G_s varying between 1 kW/m^2 and 0.087 kW/m^2, respectively. The droplet mean contact angle on (A) clean, (B) silane-treated silica nanoparticle-coated, and (C) Teflon-coated glass covers were $\bar{\theta}_c$ = 25.8°, 66.6°, and 76.2°, respectively. The droplet mean projected diameter d_p on different glass covers varied between 250 μm and 614 μm while the surface area coverage f_A ranged between 19% and 49% [90].

Table 4.1. Summary of the solar cell assemblies tested in this chapter.

Sample #	Sample details	Incident angle θ_i (°)	Droplet contact angle $\bar{\theta}_c$ (°)	Droplet surface area coverage f_A (%)	Droplet projected diameter $\bar{d}_p$ (μm)
1	Cell without glass	0-85	N/A	N/A	N/A
2	Cell with dry glass	0-85	N/A	0	N/A
3	Cell with droplet-covered glass	0-85	76.2	45	312
4	Cell with droplet-covered glass	0-85	76.2	34	271
5	Cell with droplet-covered glass	0-85	76.2	19	428
6	Cell with droplet-covered glass	0-85	66.6	47	250
7	Cell with droplet-covered glass	0-85	25.8	49	614

4.3.2 Solar cell performance

4.3.2.1 i-V curves

Figure 4.3 compares the *i-V* curves obtained from (i) a bare solar cell, (ii) a solar cell with a dry glass cover, and (iii) a solar cell with glass covers supporting droplets with mean contact angle $\bar{\theta}_c$ = 25.8°, 66.6°, and 76.2° for (a) incident angle θ_i = 0° and irradiation G_s = 1 kW/m^2, (b) θ_i = 30° and G_s = 0.86 kW/m^2, (c) θ_i = 50° and G_s = 0.64 kW/m^2, and (d) θ_i = 70° and G_s = 0.34 kW/m^2. Here, the droplet surface area coverage f_A of the glass covers was around f_A = 47±2% for all solar cell assemblies considered to isolate the effects of θ_i and $\bar{\theta}_c$ on the solar cell performance.

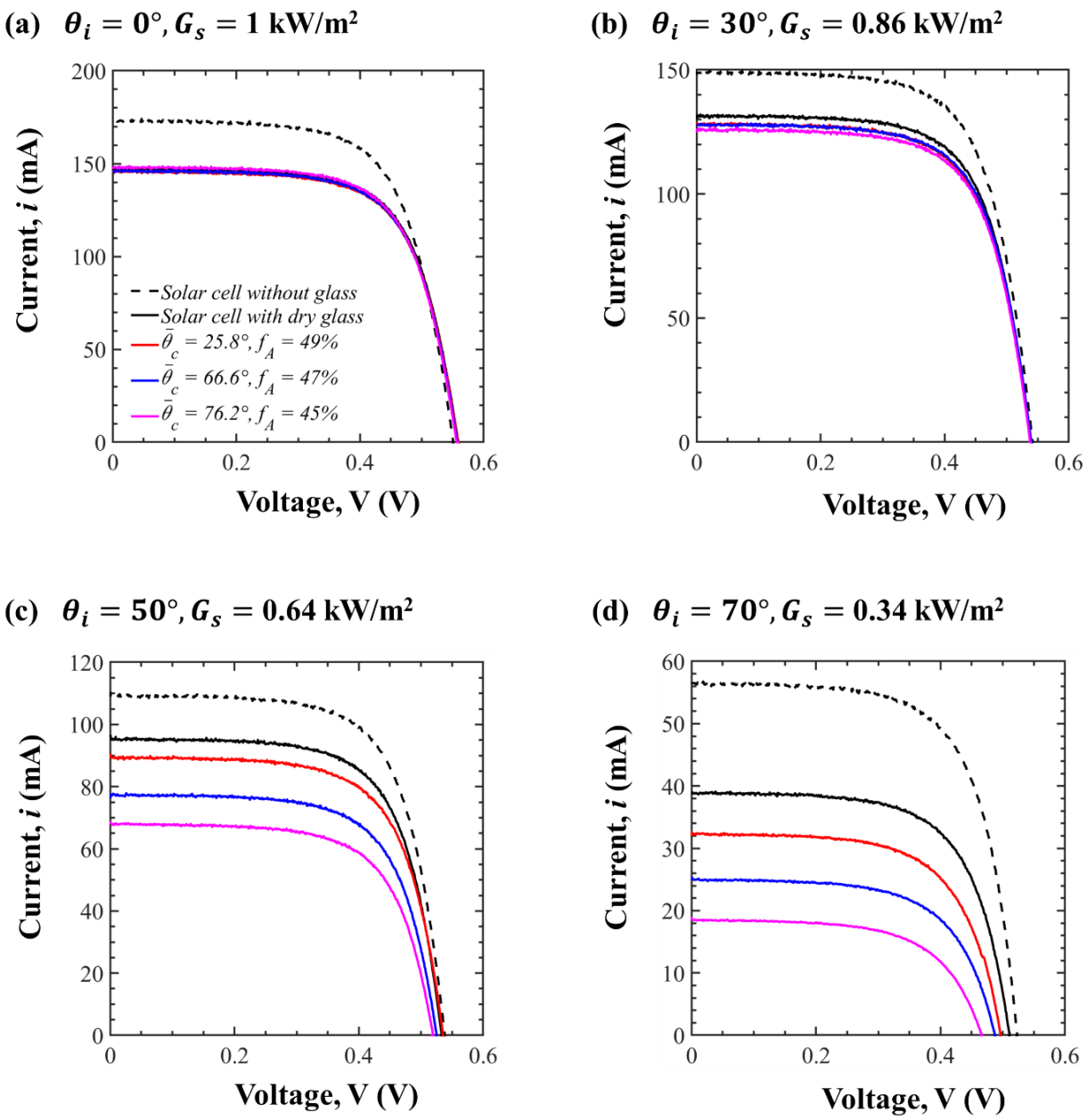

Figure 4.3. Current as a function of voltage for (a) incident angle θ_i = 0° and irradiation G_s = 1 kW/m^2, (b) θ_i = 30° and G_s = 0.86 kW/m^2, (c) θ_i = 50°and G_s = 0.64 kW/m^2, and (d) θ_i = 70° and G_s = 0.34 kW/m^2.

First, for all incident angles, the bare solar cell systematically featured the largest current i for any potential V. Thus, it can serve as a reference to assess the effects of the glass cover and droplets on the solar cell performance. Figures 4.3(a) and 4.3(b) indicate that the glass cover reduces the generated current across the potential window of the solar cell by about 15%. This relatively large decrease was due to the iron content of the conventional soda-lime glass used and can be considered as an upper bound. In fact, a thinner and/or ultra-clear glass cover would reduce significantly the effect of the dry glass cover. In addition, the presence of droplets did not affect the i-V curve of the solar cells under near-normal incident radiation ($\theta_i \leq 30°$). This can be explained by the fact that most of the collimated light incident at angle $\theta_i \leq 30°$ was transmitted through the glass cover supporting droplets, as established numerically by Zhu et al.[64]. These experimental results also corroborate the experimental observations reported in the literature indicating that the droplets did not significantly affect the performance of solar cells under normal incidence [115,116].

By contrast, Figures 4.3(c) and 4.3(d) establish that, for incident angles $\theta_i = 50°$ and 70°, the generated current i decreased significantly due to the presence of droplets, particularly as the droplet contact angle $\bar{\theta}_c$ increased from 25.8° to 76.2°. This observation can be attributed to the decrease in the number of photons reaching the photovoltaic solar cell surface due to the increase in reflectance caused by the presence of droplets [101,117]. Additional experiments were performed by spraying water droplets, using a push spray bottle, on the glass cover of the same solar cell used throughout (see Appendix C.4). The results established that the i-V curves of the solar cell with glass cover sprayed with water droplets were quantitatively similar to those obtained when the glass cover supported acrylic droplets, as illustrated in Figure C.3. However, the droplet surface area coverage f_A and projected diameter d_p could not be determined as they varied due to

rapid droplet evaporation at near-normal incident angles and/or droplet merger and roll-off for larger incident angles.

Figure 4.4 schematically illustrates light transfer through the solar cell assembly with (a) dry glass cover and (b) droplet-covered glass cover under normal collimated incident radiation. Photons that reached the air/glass interface with incident angle θ_i were refracted through the air/glass interface with the transmission angle $\theta_{t,1}$ before reaching the glass/solar cell interface. The latter has a reflectivity to unpolarized light expressed as [81]

$$R_{gc} = (R_s + R_p)/2 \tag{4.2}$$

where R_s and R_p are the reflectivities of the interface for s-polarized and p-polarized light predicted by Fresnel equations considering the glass to be non-absorbing and the solar cell to be absorbing [81].

The reflectivity R_{gc} of the glass/solar cell interface remained nearly constant around 19% for incident angle θ_i ranging from 0 to 85^o (see Appendix C.5). *In absence of droplets*, the photons reflected by the glass/solar cell interface traveled through the glass window and were reflected back towards to solar cell due to internal reflection at the glass/air interface with critical angle $\theta_{cr,ga} = \sin^{-1}(n_a/n_g) \approx 41°$ [81] [Figure 4.4(a)]. The multiple reflections through the glass cover increase the probability of the photons to eventually be absorbed by the solar cells. By contrast, *in presence of droplets*, the reflected photons were transmitted into the droplets through the glass/droplet interface because of the small index mismatch between the glass and the droplets corresponding to a large critical angle $\theta_{cr,gd} = \sin^{-1}(n_d/n_g) \approx 77°$ [81] [Figure 4.4(b)]. Then, due to the droplet curvature, the photon reached the droplet/air interface at an angle smaller than the critical angle of that interface $\theta_{cr,da} = \sin^{-1}(n_a/n_d) \approx 39°$ and were transmitted through the interface. Note that reflection losses were very similar at the air/glass and air/droplet interface so the number of

photons entering the solar cell assembly was not significantly affected by the presence of droplets. In addition, reflection loss at the droplet/glass interface was negligible due to the very small index mismatch. Overall, the presence of droplets resulted in back-scattering of incident photons instead of trapping and photovoltaic conversion.

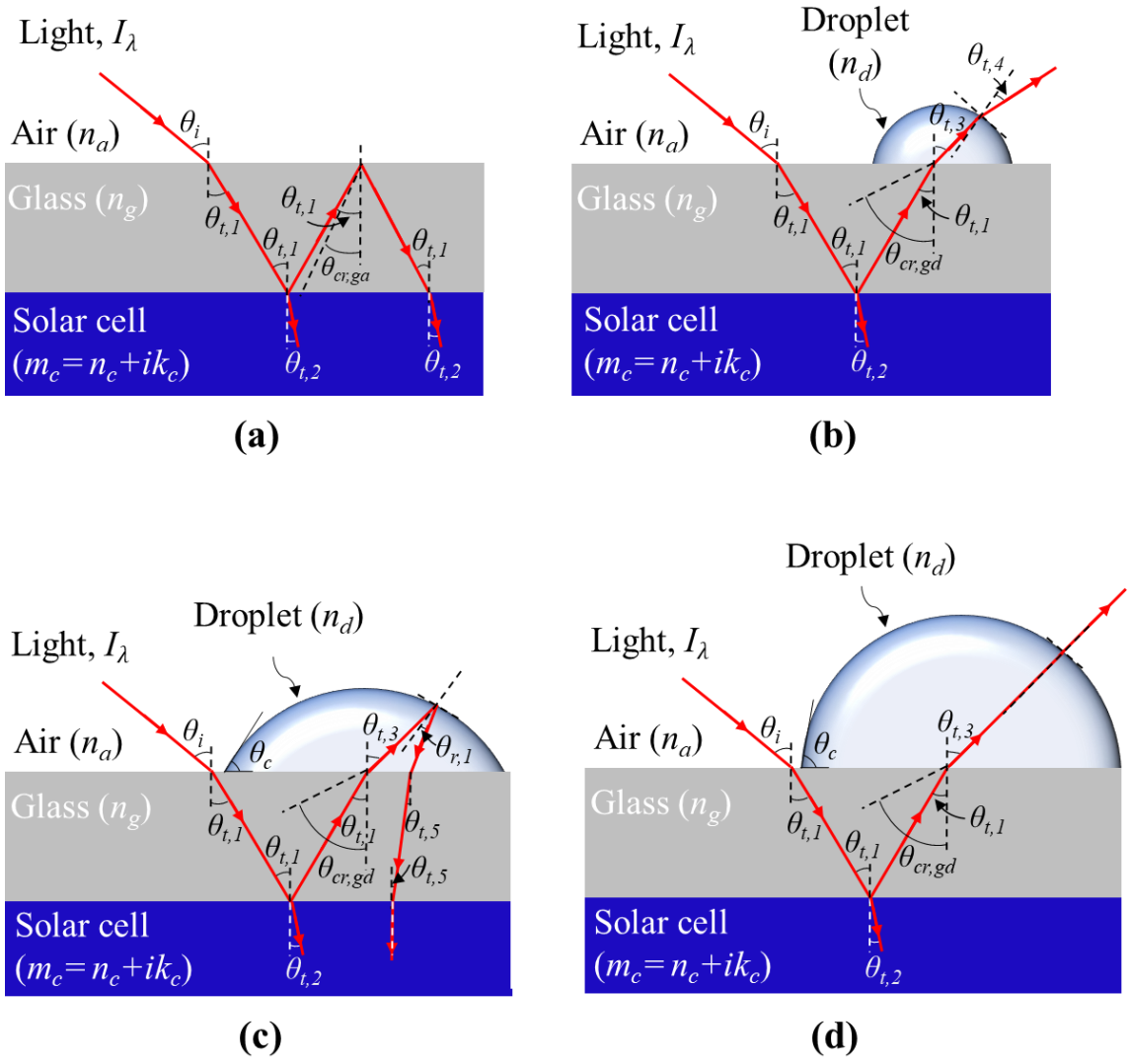

Figure 4.4. Schematic of a solar cell with (a) dry glass cover and (b) droplet-covered glass cover to explain the effect of droplets on the light transmittance and a solar cell with droplet-covered glass cover having (c) small droplet contact angle and (d) large droplet contact angle to demonstrate the effect of droplet contact angle on the light transmittance under collimated incident radiation at angle θ_i.

Furthermore, Figures 4.3(c) and 4.3(d) indicate that, for surface coverage $f_A \approx 47\%$ and large incident angle $\theta_i \geq 50^o$, the generated current decreased with increasing droplet mean contact angle $\bar{\theta}_c$. Figures 4.4(c) and 4.4(d) schematically illustrate the effect of the droplet contact angle on the number of photons reaching the solar cell surface. The number of photons transmitted through the droplet/air interface increased with increasing droplet contact angle due to the fact that the photon incident angle on the droplet/air interface decreased with decreasing droplet radius of curvature defined as $r_c = \mathrm{d}/2\sin\bar{\theta}_c$. As a result, less photons were reflected back towards the solar cell and the generated cell current decreased. Note that, only for droplet contact angles $\bar{\theta}_c \geq 76.2^o$, the photons that were incident at large angles could experience total internal reflection at the droplet/air interface and then reached the solar cell. Zhu et al.[64] numerically showed that, for water droplets condensed at the frontside of windows, total internal reflection at the droplet/air interface occurred for droplet contact angles $\theta_c \geq 70^o$ and large incident angles, i.e. for $\theta_c = 70^o$ total internal reflection occurred for incident angles $\theta_i > 80^o$.

4.3.2.2 Maximum power

Figure 4.5(a) shows the maximum power P_{max} generated by the solar cell as a function of the incident angle θ_i for the three different assemblies considered. Here also, the droplet mean contact angles considered were $\bar{\theta}_c$ = 25.8°, 66.6°, or 76.2° while the surface area coverage f_A was maintained around 47 ± 2 %. Figure 4.5(a) indicates that, for a solar cell, bare or with a dry glass cover, the maximum power P_{max} decreased with increasing incident angle θ_i [118]. In fact, the maximum power generated by the solar cell closely follows the same trend as the incident solar irradiation $G_s = S_c \cos\theta_i$ and has been expressed as [119]

$$P_{max}(\theta_i) = P_{max}(\theta_i = 0)\cos\theta_i. \quad (4.3)$$

Figure 4.5(a) establishes that the measured maximum power of bare solar cell P_{max} was in excellent agreement with the predictions of Equation (4.3). However, the measured maximum power of solar cells with a dry glass cover slightly deviated from Equation (4.3) for $\theta_i \geq 50°$. This can be attributed to the increase in the reflection losses for incident angle θ_i larger than the Brewster angle θ_B. Indeed, the reflectivity of the air/glass interface to incident unpolarized light remained nearly constant for $\theta_i < \theta_B$ and then increased sharply for $\theta_i > \theta_B$ where the Brewster angle is equal to $\theta_{B,ag} = tan^{-1}(n_g/n_a) \approx 57°$ [81]. On the other hand, the Brewster angle for the bar solar cell was $\theta_{B,ac} = tan^{-1}(n_c/n_a) \approx 74°$. In addition, the maximum power P_{max} of the solar cells was unchanged for dry and droplet-covered glass covers under normal incidence ($\theta_i = 0°$). These results corroborate the observations of Hosseini et al.[29] for monocrystalline solar cells. Figure 4.5(a) also establishes that, in the presence of droplets, the maximum power P_{max} decreased with increasing $\bar{\theta}_c$ for $\theta_i > 30°$ because of the optical phenomena invoked previously [Figure 4.4].

4.3.2.3 Solar cell energy conversion efficiency

Figure 4.5(b) shows the solar cell energy conversion efficiency η [Equation (4.1)] as a function of the incident angle θ_i for the same three configurations considered previously with similar surface area coverage f_A around 47% but different droplet contact angles $\bar{\theta}_c$ between 25.8° and 76.2°. Figure 4.5(b) indicates that for $0° \leq \theta_i \leq 30°$, the energy conversion efficiency η remained constant and identical for all solar cell assemblies with a glass cover with or without droplets. However, for $\theta_i > 30°$, the energy conversion efficiency η decreased with increasing incident angle θ_i and droplet contact angle $\bar{\theta}_c$. For example, for $\theta_i = 60°$, the energy conversion efficiency decreased from η = 10 % for a dry glass cover to 9% and 5% for droplet mean contact angle $\bar{\theta}_c$ of 25.8° and 76.2°, respectively. This decrease in the energy conversion efficiency can be attributed to the decrease in the maximum power output of the PV solar cell, as previously discussed [Figure 4.5(a)].

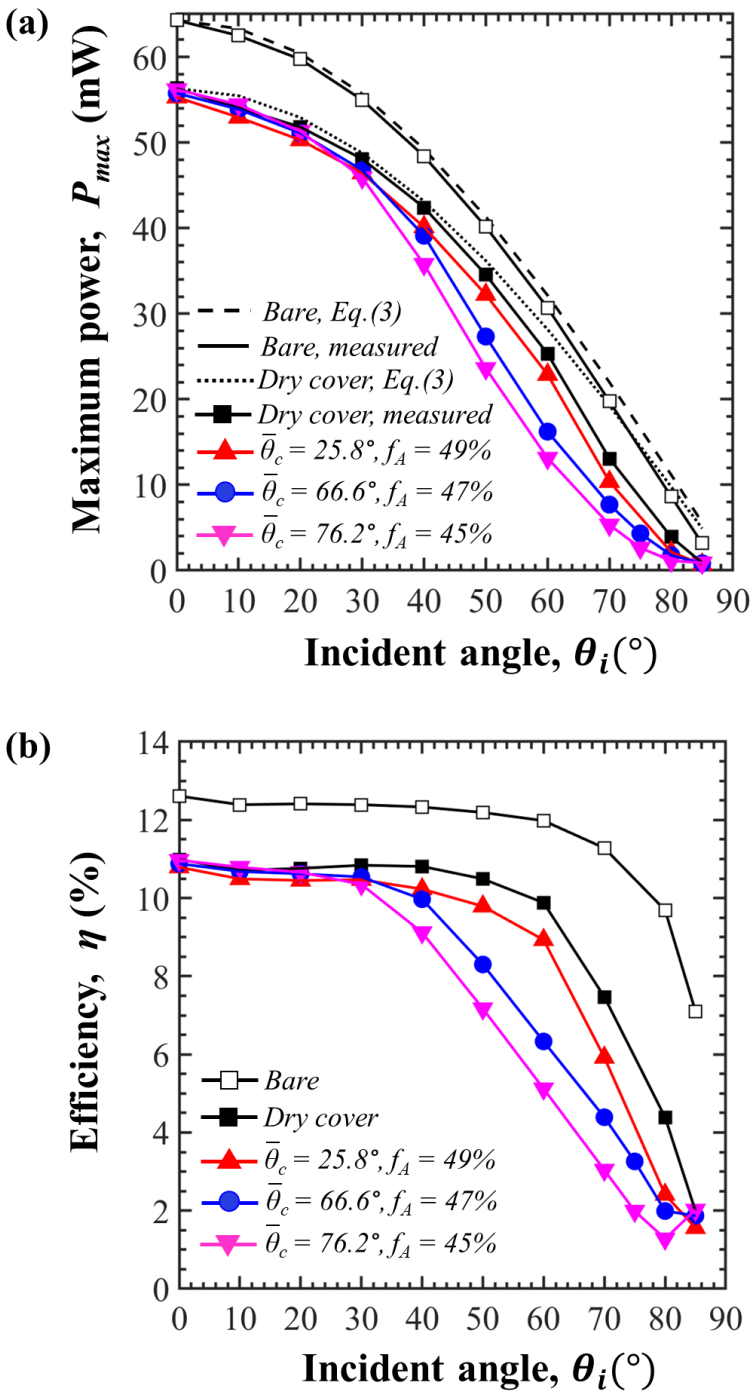

Figure 4.5. (a) Maximum power P_{max} and (b) energy conversion efficiency η as functions of incident angle θ_i for the solar cell without glass cover, with dry glass cover, and with droplet-covered glass cover droplet mean contact angle $\bar{\theta}_c$= 25.8°, 66.6°, and 76.2° and surface area coverages f_A = 45, 47, and 49%, respectively.

Moreover, it is interesting to note that, for $\bar{\theta}_c$ = 76.2° and f_A = 45%, the solar cell energy conversion efficiency η decreased with increasing incident angle θ_i until it reached a minimum at θ_i = 80° beyond which it increased. This was due to the fact that transmittance of the solar irradiance through the glass cover supporting droplets increased at large incident angles (θ_i > 80°), thus improving the energy conversion efficiency. In fact, this behavior was also observed by Zhu et al.[64] in the numerically predicted directional hemispherical transmittance through a 3 mm thick glass slab supporting water droplets with contact angle $\theta_c \geq 70°$. The authors attributed this behavior to the decrease in total internal reflection at the back window/air interface and to the increase in internal reflection at the droplet/air interfaces for glazing incident angles θ_i [64].

To isolate the effect of droplet surface area coverage f_A on the solar cell efficiency η, we define the efficiency ratio $\eta_r(\theta_i, \bar{\theta}_c, f_A)$ as the ratio of the energy conversion efficiency of the solar cell with droplet-covered glass $\eta(\theta_i, \bar{\theta}_c, f_A)$ to that of the dry glass cover $\eta(\theta_i, f_A = 0)$ under the same incident angle θ_i, i.e.,

$$\eta_r(\theta_i, \bar{\theta}_c, f_A) = \eta(\theta_i, \bar{\theta}_c, f_A)/\eta(\theta_i, f_A=0). \quad (4.4)$$

Figure 4.6 plots the energy conversion efficiency ratio $\eta_r(\theta_i, \bar{\theta}_c, f_A)$ as a function of incident angle θ_i for a solar cell with a droplet-covered glass cover with $\bar{\theta}_c$ = 76.2° and f_A = 19, 34, and 45%. Figure 4.6 indicates that the efficiency ratio η_r decreased significantly due to the presence of droplets for θ_i > 30°. The decrease was more significant for larger f_A. In fact, the presence of droplets caused the solar cell efficiency to decrease by up to 50-70% compared to a dry glass cover, for the range of f_A considered. This was due to the fact that an increasingly large fraction of the incident light was back-scattered as f_A increased, as previously explained. Note that for θ_i > 80°, the solar cell with a droplet-covered glass cover with f_A = 45% featured a slightly higher efficiency than the solar cell with a dry glass cover as droplets scattered the light back towards the solar cell.

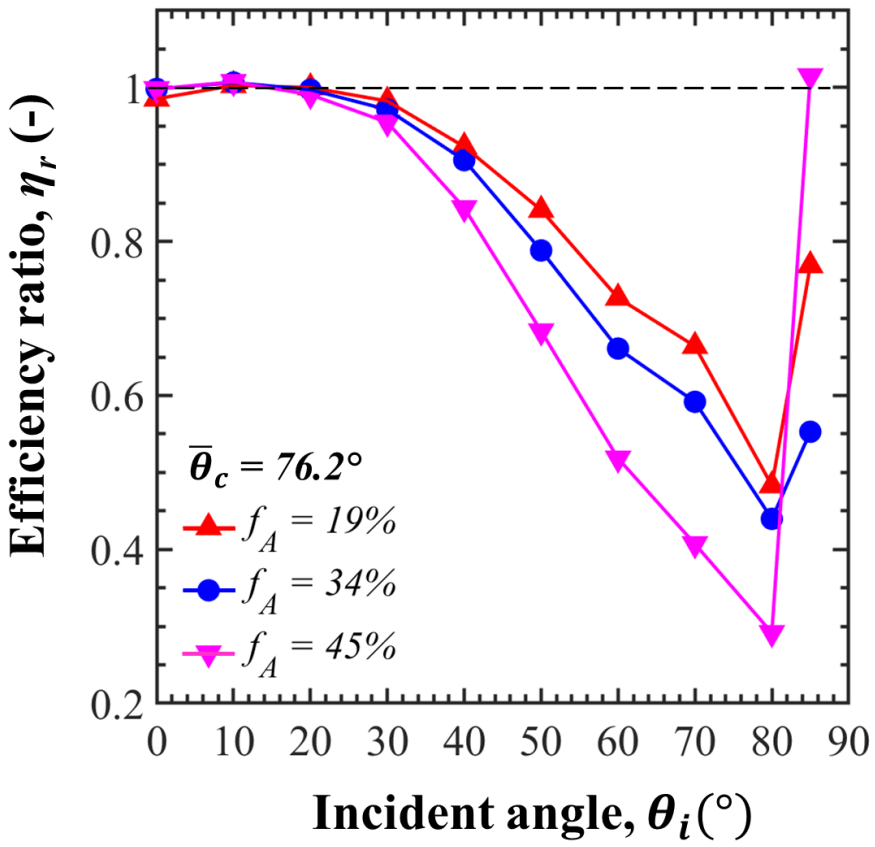

Figure 4.6. Energy conversion efficiency ratio η_r as a function of incident angle θ_i for solar cell with droplet-covered glass cover having a droplet contact angle $\bar{\theta}_c$ = 76.2° and surface area coverages f_A = 19, 34, 45%.

4.3.3 Impact of dew formation on hourly energy generation

Dew formation occurs at night [43,44] and is frequently observed on PV modules in the morning hours [120–122]. For certain locations/seasons, dew formation can persist during the daytime depending on weather conditions such as high humidity and wind speed [45,123], and field conditions such as the presence of hygroscopic dust [112]. To assess the impact of droplets on the power generation of solar cells deployed in the field, let us consider a field of PV solar cells located in San Francisco, CA (latitude: 37°N; longitude: 122°W) in December. San Francisco was selected for the widespread deployment of residential solar PV power generation in California [124] and

the frequent dew formation [125]. In order to predict the energy generated per unit surface area of PV solar cells, the following assumptions were made: (i) PV solar cells were facing South with the optimum tilt angle of θ_T = 30° [126,127], (ii) the PV solar cell temperature T_c (in °C) was predicted according to [128]

$$T_c(t) = 0.943T_a(t)+0.028G_s(t)–1.528u_w(t)+4.3. \quad (4.5)$$

Here, T_a is the ambient air temperature (in °C) and u_w is the wind velocity (in m/s). The average hourly solar irradiation and incident angle for a 30° tilted PV solar cell in San Francisco were taken from Refs.[129] and [130], respectively. The hourly weather hygrometric and wind speed data for San Francisco averaged over several years were taken from Ref.[131].

Moreover, the average hourly electrical energy production rate P_h (in W/m^2) can be expressed as

$$P_h(\theta_i(t)) = G_s(\theta_i)\eta(\theta_i, \bar{\theta}_c, f_A). \quad (4.6)$$

where the incident angle $\theta_i(t)$ depends on the time of the day and $\eta(\theta_i, \bar{\theta}_c, f_A)$ is the energy conversion efficiency previously measured for the different solar cell assembly configurations.

Figure 4.7 shows the hourly (a) ambient air $T_a(t)$, dew point, and PV cell $T_c(t)$ temperatures (in °C) and (b) average hourly electrical energy production rate (W/m^2) predicted by Equation (4.6) for a solar cell with (i) dry glass cover and (ii) droplet-covered glass cover with droplet mean contact angle $\bar{\theta}_c$ = 76.2° and surface area coverage f_A = 19, 34, and 45% on December 3. The use of hydrophobic coatings has been recommended for PV module glass covers [132–136] as a practical way to reduce dust adhesion [134–137] and remove soiling during droplet roll-off [138–140]. In addition, hydrophobic coatings inhibit condensation [112] and can be designed to reduce light reflection [138]. Therefore, the droplet contact angle $\bar{\theta}_c$ = 76.2° was taken as a baseline for our calculations.

Figures 4.7(a) and 4.7(b) indicate that the dew formation resulted in a drop in the average hourly electrical energy production rate in the morning and afternoon. For example, the energy generation at 9:00 am decreased by 14%, 38%, and 53% for droplet mean contact angle $\bar{\theta}_c = 76.2°$ and surface area coverage $f_A = 19$, 34, and 45% compared with the solar cells with dry glass covers, respectively. Note that cleaning of the dust accumulated on hydrophobic PV modules thanks to dew roll-off and/or rain was not considered. In addition, the temporal changes in the droplet surface area coverage due to the evaporation and/or condensation and tilting the PV module were not considered. Finally, differences in the droplet surface area coverage for hydrophilic and hydrophobic glass covers were not accounted for.

Overall, these results suggest that dew or rain can significantly affect the performance of solar cells particularly in the morning or afternoon when the solar radiation is incident at angle $\theta_i > 30°$. Hydrophilic covers or coatings can limit the negative effect of droplets provided their hydrophilicity can be maintained throughout the lifetime of the solar cells.

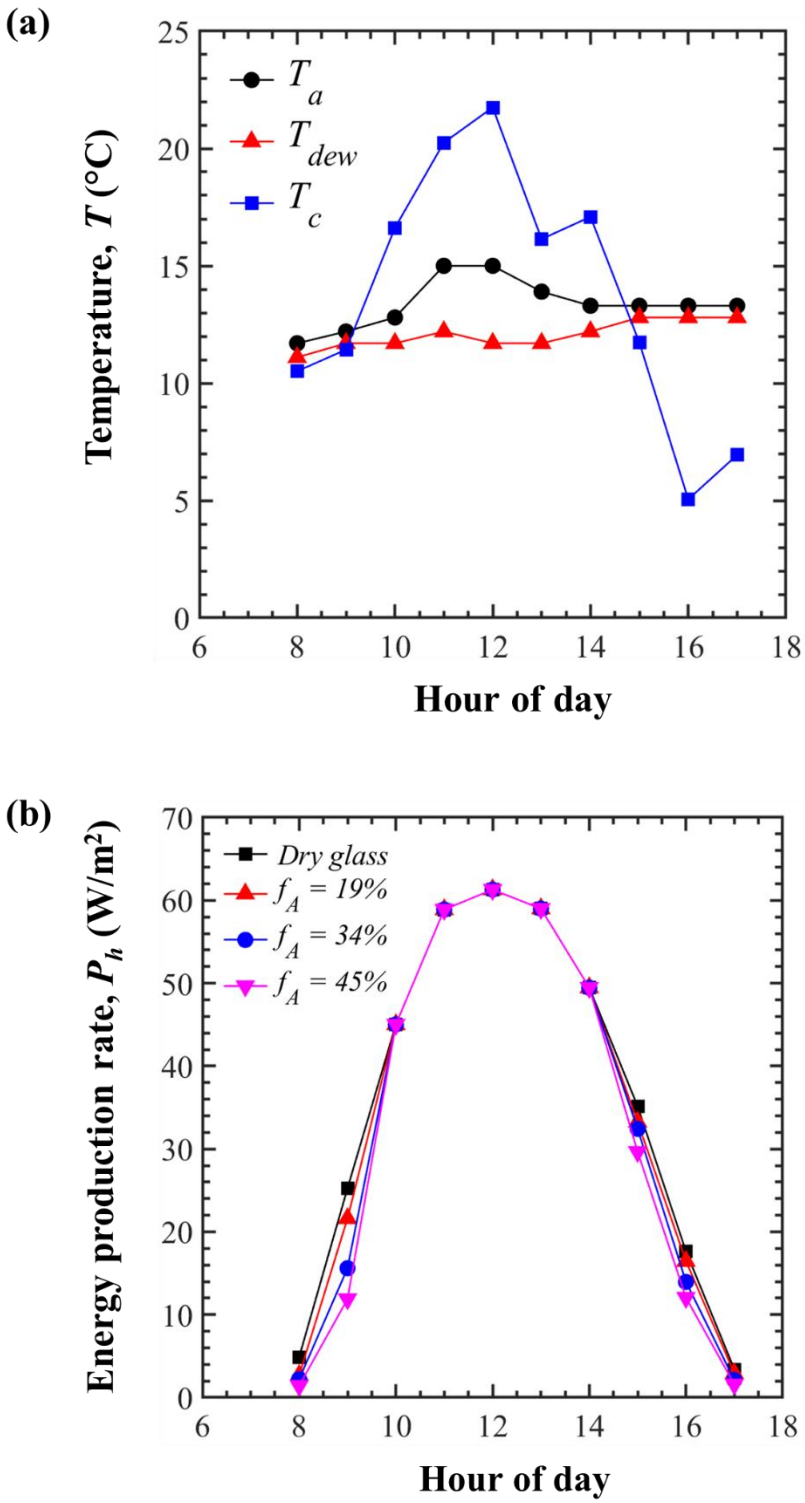

Figure 4.7. Hourly (a) ambient, dew point, and solar cell temperatures and (b) energy production rate on December 3 as functions of the hour in San Francisco, CA.

4.4 Conclusion

This chapter investigated experimentally the effect of droplets on the performance of PV solar cells due to dropwise condensation or rain falling on their glass cover. Polydisperse acrylic droplets were deposited on glass covers subjected to different surface treatments. The droplet contact angle was varied between 25° and 77° and their surface area coverage between 19% and 49%. The photovoltaic solar cells with a dry or droplet-covered glass cover were exposed to collimated simulated solar radiation with radiation flux up to 1 kW/m^2 with incident angle θ_i ranging between 0 to 85°. For incident angle $\theta_i \leq 30°$, the droplets had no effect on the generated current, the maximum power, and the energy conversion efficiency of the solar cells. However, for incident angle $\theta_i > 30°$, the droplet significantly decreased the solar cell performance, particularly for large droplet contact angle and/or the surface area coverage. This was attributed to the fact that the incident light was back-scattered through the droplets instead of being trapped due to total internal reflection at the cover/air interface before being eventually absorbed by the solar cell. In addition, the chapter showed that the hourly energy production may decrease significantly with dew formation on the solar cell cover, based on actual weather conditions. These results highlight the importance of selecting durable hydrophilic solar cell cover.

Chapter 5: Dropwise Condensation Enhances Emittance and Reduces Selectivity of Radiative Cooling Surfaces

Dew formation occurs frequently on the radiative cooling surfaces used for cooling of buildings and for harvesting atmospheric water as a result of dropwise condensation. These condensed droplets can alter both the emittance and spectral selectivity of radiative cooling surfaces. This study experimentally investigates the impact of dropwise condensation on the emittance and selectivity of a radiative cooling surface. Here, selective emitters supporting a large number of polydisperse acrylic droplets contact angle ranging between 39° and 62° and surface area coverage between 20% and 52% were prepared and characterized. Spectral characterization revealed that the spectral emittance of the radiative cooling surfaces increased and broadened significantly in the presence of droplets. This was attributed to the absorption by the acrylic droplets. The emittance inside the long-wavelength infrared (LWIR) atmospheric transparency window increased slightly while the emittance outside increased significantly with increasing surface area coverage and droplet contact angle. As a result of the loss of spectral selectivity and the resulting heat gain from radiation exchange outside the LWIR, droplet-covered emitters attained a higher sub-ambient cooling relative to the dry surfaces.

5.1 Materials and Methods

5.1.1 Sample preparation

The radiative cooling samples used in this study consisted of 60 μm-thick 3M Scotch™ Long-Lasting (SLL) tape (3M, USA) on 20 μm-thick aluminum (Al) foil with a surface area of 2.5 x 2.5

cm^2. The reference radiative cooling surface consisted of two layers of scotch tape manually applied to the Al foil, with care taken to prevent the formation of air bubbles below and between the layers. Nine different samples with or without hydrophobic coatings were prepared to achieve different droplet contact angles and projected surface area coverages including (1) the reference sample with droplet surface area coverage f_A ranging between 0% and 100% (Samples 1, 2, 3, 4, 5), (2) the reference sample coated with commercial water-repellent spray paint (NeverWet™, Rust-Oleum, USA) with f_A ranging between 0% and 51% (Samples 6, 7A, 7B), and (3) the reference sample coated with monolayer of perfluorinated silane (tridecafluoro-1,1,2,2,-tetrahydrooctyl)trichlorosilane (Gelest, USA) with f_A ranging between 0% and 52% (Samples 8, 9, 10A, 10B). The reference sample was used to represent the hydrophilic radiative cooling surface while NeverWet™ and perfluorinated silane coated samples were representatives of hydrophobic radiative cooling surfaces.

Samples 6 and 7 were made by coating the reference sample with water-repellent spray paint. First, NeverWet™ Step 1 Base Coat (275185, industrial size multi-purpose liquid repelling treatment kit) was sprayed directly on the sample surface and waited for one hour to dry. Then, NeverWet™ Step 2 Top Coat (275185, industrial size multi-purpose liquid repelling treatment kit) was sprayed onto the surface of the sample and left to for 12 hours.

Samples 8, 9, and 10A were prepared by coating the reference sample with perfluorinated silane. To do so, samples were placed inside a closed container with liquid perfluorinated silane. The silane vaporized and reacted with hydroxyl groups (–OH) present on the cellulose acetate - the main group of the non-sticking side of the SLL tape - and formed a hydrophobic coating on the surface of the sample [141].

Lastly, thousands of droplets made of acrylic polymer (Loctite AA 349, Henkel Adhesives, USA) were deposited manually with the tip of a needle on the surface of the uncoated and coated samples. After the deposition, acrylic droplets were cured with a UV lamp (Blak-Ray B-100A, Thermo Scientific Fisher, USA) emitting at a wavelength of 365 nm. Figure 5.1 shows the photograph of the reference sample supporting acrylic droplets with droplet mean contact angle $\bar{\theta}_c$ = 39° and surface area coverage f_A = 50%. In addition, an acrylic film 300 μm in thickness was deposited on an uncoated sample using a film applicator (EQ-Se-KTQ-150, MTI Corporation, USA) to achieve surface area coverage f_A = 100% to be used as a reference. Polymer droplets rather than water droplets were used to eliminate any change in the droplet diameter and surface area coverage throughout the measurements due to evaporation, rolling off, and/or merging of the droplets. As a result, the droplet size distribution and surface area coverage of each sample remained constant and could be thoroughly characterized. Both of the acrylic and water are transparent in the visible and near-infrared for wavelengths up to 1.2 μm and are broadband thermal emitters. Therefore, the optical effects caused by the presence of the acrylic droplets are expected to be similar to that of water droplets despite the difference in their refractive and absorption indices. A detailed comparison of the acrylic and water in terms of optics and thermal emissions have been presented in Section 5.2.

5.1.2 Droplet characterization

The contact angle of the acrylic droplets deposited on the uncoated and coated radiative cooling surfaces was measured with a goniometer (VCA-3000S, AST Products, USA). The mean droplet contact angle $\bar{\theta}_c$ was measured by averaging the contact angle measurements for at least 5 droplets. The images of droplet-covered samples were captured with a camera and analyzed with ImageJ

(National Institutes of Health, USA) to determine the surface area coverage f_A and the droplet projected diameter $\bar{d}_p$.

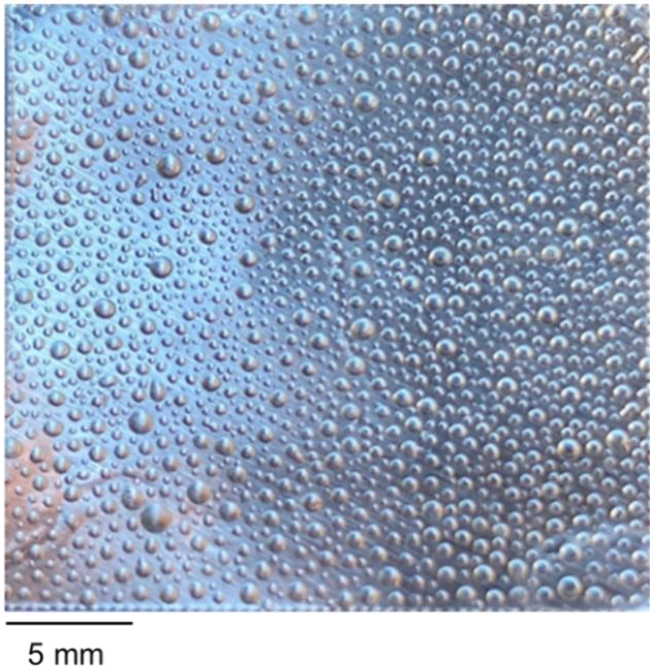

Figure 5.1. Photograph of a reference sample supporting acrylic droplets with droplet mean contact angle $\bar{\theta}_c$ = 39° and surface area coverage f_A = 50%.

5.1.3 Infrared characterization

A nitrogen-purged Fourier transform infrared (FTIR) spectrometer (Nicolet™ iS50, Thermo Scientific Fischer, USA) equipped with an integrating sphere (Upward IntegratIR™, PIKE Technologies, USA) was used to measure the spectral normal-hemispherical reflectance $R_{nh,\lambda}$ of the dry and droplet-covered samples. The spectral directional-hemispherical reflectance $R_{dh,\lambda}$ of the samples were measured using a FTIR spectrometer (INVENIO®, Bruker) equipped with a custom-made integrating sphere. For both measurements, a potassium bromide (KBr) beamsplitter and a liquid-nitrogen cooled mercury-cadmium-telluride (MCT) detector were used in the spectral range between 2 and 20 μm.

5.1.3.1 Spectral directional emittance

For opaque samples, the spectral directional emittance $\varepsilon_{d,\lambda}$ is given by Kirchhoff's law expressed as [46]

$$\varepsilon_{d,\lambda} = \alpha_{d,\lambda} = 1 - R_{dh,\lambda} \tag{5.1}$$

where $\alpha_{d,\lambda}$ is the spectral directional absorptance and $R_{dh,\lambda}$ is the directional-hemispherical reflectance. Note that, the directional spectral emittance in the normal direction $\theta_i = 0°$ is equal to the normal spectral emittance denoted by $\varepsilon_{n,\lambda}$, i.e. $\varepsilon_{d,\lambda}(\theta_i = 0°) = \varepsilon_{n,\lambda}$.

5.1.3.2 Total directional emittance

The total directional emittance ε_d can be calculated as [46]

$$\varepsilon_d = \frac{\int_0^{\infty} \varepsilon_{d,\lambda} E_{b,\lambda}(T_o) d\lambda}{\int_0^{\infty} E_{b,\lambda}(T_o) d\lambda} \approx \frac{\int_{2\ \mu m}^{20\ \mu m} \varepsilon_{d,\lambda} E_{b,\lambda}(T_o) d\lambda}{\int_{2\ \mu m}^{20\ \mu m} E_{b,\lambda}(T_o) d\lambda} \tag{5.2}$$

where $E_{b,\lambda}(T_o)$ is the blackbody spectral emissive power (in W/m^2·μm) at temperature T_o = 296 K. The integrals in both the numerator and denominator of Equation (5.2) were truncated to wavelengths between 2 - 20 μm as the samples were opaque in this spectral range. Here also, the directional emittance ε_d in the normal direction $\theta_i = 0°$ is the normal emittance denoted by ε_n so that $\varepsilon_{d,}(\theta_i = 0°) = \varepsilon_n$.

5.1.3.3 Directional emittance inside and outside the atmospheric window

The directional emittance $\varepsilon_{d,LWIR}$ inside the atmospheric transparency window, defined by the wavelength range between 8 - 13 μm [142], was defined as [31]

$$\varepsilon_{d,LWIR} = \frac{\int_{8\ \mu m}^{13\ \mu m} \varepsilon_{d,\lambda} E_{b,\lambda}(T_o) d\lambda}{\int_{8\ \mu m}^{13\ \mu m} E_{b,\lambda}(T_o) d\lambda}. \tag{5.3}$$

Similarly, the directional emittance outside the atmospheric transparency window $\varepsilon_{d,non\text{-}LWIR}$ was defined as [31]

$$\varepsilon_{d,non-LWIR} = \frac{\int_{2\ \mu m}^{20\ \mu m} \varepsilon_{d,\lambda} E_{b,\lambda}(T_o) d\lambda - \int_{8\ \mu m}^{13\ \mu m} \varepsilon_{d,\lambda} E_{b,\lambda}(T_o) d\lambda}{\int_{2\ \mu m}^{20\ \mu m} E_{b,\lambda}(T_o) d\lambda - \int_{8\ \mu m}^{13\ \mu m} E_{b,\lambda}(T_o) d\lambda}. \quad (5.4)$$

5.1.4 Outdoor nighttime demonstration

Outdoor nighttime experiments were conducted to assess the effect of droplets on the temperature of the radiative cooling surface under actual outdoor conditions. The experiments were performed at night to prevent differences in solar absorptance of the dry and droplet-covered samples from interfering with the effect of thermal emittance.

Figure 5.2(a) shows the experimental setup consisting of (i) dry and droplet covered samples used for outdoor experiments with a surface area of A = 10 x 10 cm^2, (ii) a data logger (RDXL6SD-USB, OMEGA Engineering, USA) used to record the temporal evolution of the samples' temperature, and (iii) a thermometer combined with a hygrometer (TP59, ThermoPro, USA) to measure the temperature and relative humidity of the ambient air.

Two different samples were prepared for outdoor experiments including a dry and a droplet-covered sample with droplet surface area coverage f_A = 52% and contact angle $\bar{\theta}_c$ = 39°, as shown in Figure 5.2(b). Samples were placed in an open-top Styrofoam casing to ensure thermal insulation from the horizontal support, as schematically illustrated in Figure 5.2(c). In addition, the top surface of the casing was covered with an infrared transparent low-density poly(ethylene) (PE) film to limit convective heat transfer. A calibrated T-type thermocouple (OMEGA Engineering, USA) was placed at the bottom of the sample and sealed with thermal tape. All experiments were conducted at nighttime on the rooftop of a parking lot in Los Angeles, California so that horizontal samples had an unobstructed view of the sky.

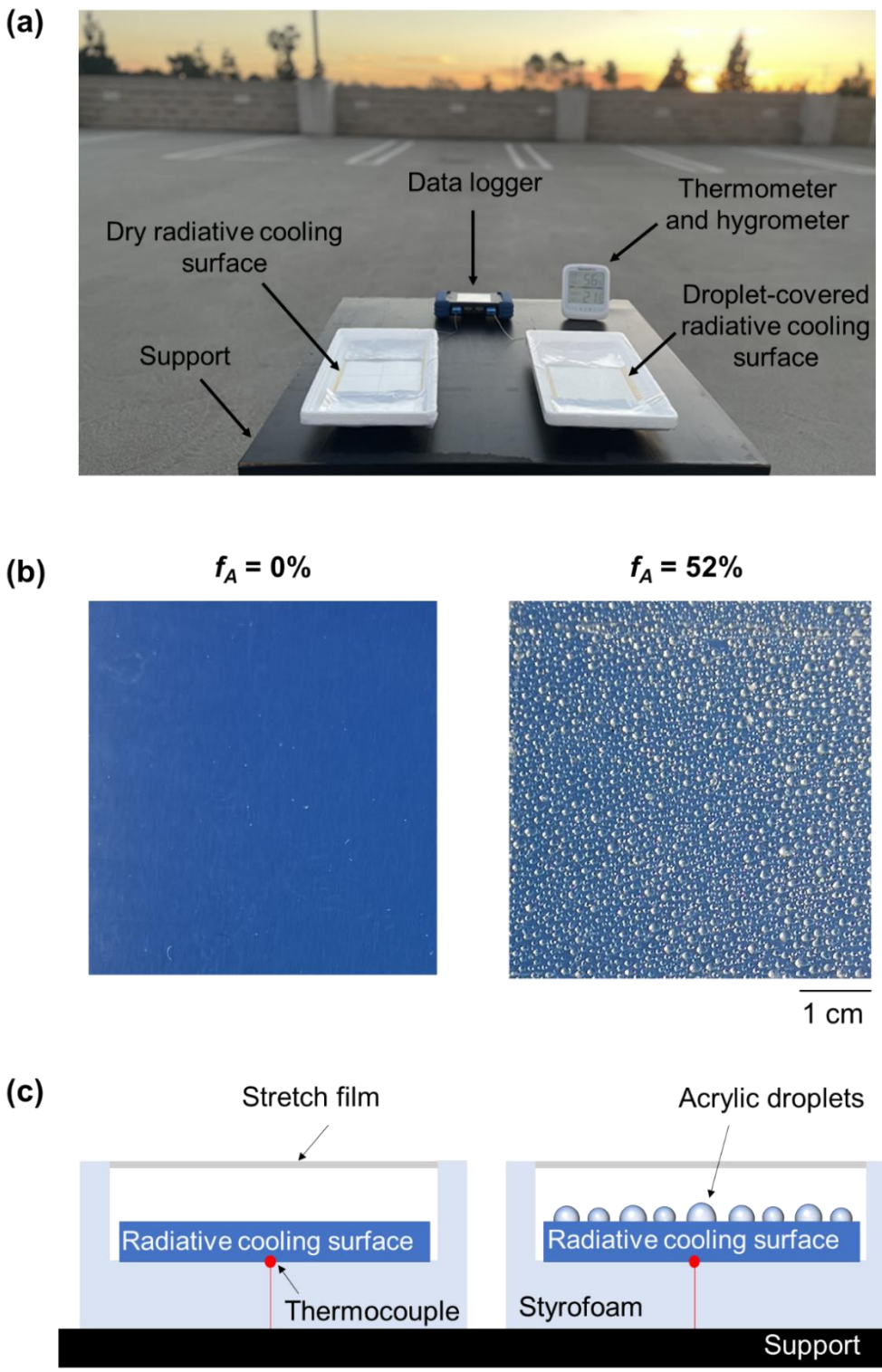

Figure 5.2. Photographs of the (a) experimental setup and of (b) uncoated dry and droplet-covered radiative cooling surfaces. (c) Schematic of the setup used in the outdoor nighttime experiments.

5.2 Analysis

In order to justify the use of acrylic droplets as a substitute for water droplets in terms of optics and thermal emissions, two different approaches were followed. First, the spectral normal emissivities of a semi-infinite slab made from acrylic or water were calculated and compared. Second, the spectral normal emittance of a slab supporting polydisperse acrylic or water droplets on its front side was numerically predicted using the Monte Carlo ray-tracing (MCRT) method previously developed [64,66] and experimentally validated in the visible [90] and infrared [143] parts of the electromagnetic spectrum.

5.2.1 Spectral normal emissivity of a semi-infinite slab

The normal-normal reflectance $R_{nn,s,\lambda}$ of an optically smooth semi-infinite slab with spectral refractive index $n_{d,\lambda}$ and absorption index $k_{d,\lambda}$, made of acrylic or water, is given by [81]

$$R_{nn,s,\lambda} = \frac{(n_{d,\lambda}-1)^2+k_{d,\lambda}^2}{(n_{d,\lambda}+1)^2+k_{d,\lambda}^2} \tag{5.5}$$

Then, the normal spectral emissivity $\varepsilon_{n,s,\lambda}$ of the semi-infinite slabs was calculated using Equation (5.1).

5.2.2 Spectral normal emittance of a surface supporting droplets

5.2.2.1 Problem statement

Figure 5.3 shows the schematic of an opaque slab with a complex refractive index $m_{s,\lambda} = n_{s,\lambda} + ik_{s,\lambda}$ supporting polydisperse droplets on its front side with contact angle θ_c, projected diameter d_p, and complex refractive index $m_{d,\lambda} = n_{d,\lambda} + ik_{d,\lambda}$. The droplet-covered surface is exposed to collimated and normally incident infrared radiation intensity I_λ at wavelength λ. To have realistic droplet size and surface area coverage f_A, the projected diameter d_p and coordinates (x, y) of 528 droplets deposited and characterized on Sample 10B with f_A = 52% were used in the numerical simulations.

Two different surfaces simulated namely soda-lime glass surface due to its high emissivity and aluminum surface due to its low emissivity [46].

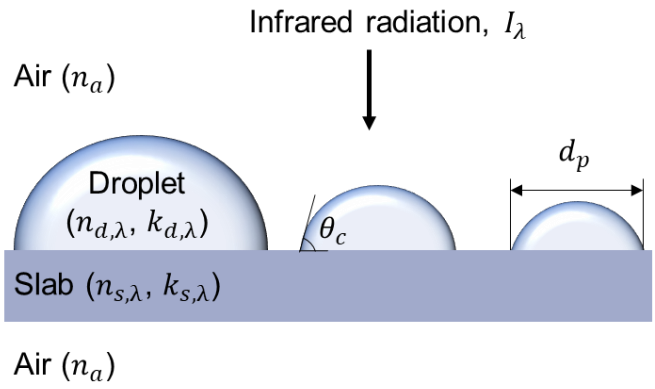

Figure 5.3. Schematic of a simulated horizontal semi-infinite opaque slab supporting polydisperse droplets on its front side.

5.2.2.2 Assumptions

The numerical simulations were performed based on the following assumptions: (1) all interfaces were optically smooth such that Fresnel equation and Snell's law were valid. (2) All droplets were cap-shaped with identical contact angle θ_c and constant curvature. (3) The droplet size and slab dimensions were much larger than the wavelength λ of the infrared radiation I_λ such that geometric optics prevailed.

5.2.2.3 Optical properties of droplets and substrates

The spectral refractive $n_{s,\lambda}$ and absorption $k_{s,\lambda}$ indices of the slab made from soda-lime glass and aluminum were taken from Refs.[80] and [144], respectively. Similarly, the spectral refractive $n_{d,\lambda}$ and absorption $k_{d,\lambda}$ indices of the droplets made from acrylic and water were taken from Refs.[92] and [98], respectively.

5.2.2.4 Method of solution

The normal-hemispherical reflectance $R_{nh,\lambda}$ the opaque substrate supporting acrylic or water droplets on its front side was numerically predicted using the Monte Carlo ray-tracing (MCRT) method described in Ref.[64]. Here, 10^6 photon bundles were used in each simulation to achieve numerical convergence. After determining the normal-hemispherical reflectance $R_{nh,\lambda}$, the spectral emittance $\varepsilon_{n,s,\lambda}$ of the droplet covered slabs was calculated from Equation (5.1).

5.2.3 Results and discussion

Figure 5.4 compares the spectral normal emissivity $\varepsilon_{n,\lambda}$ of acrylic and water for wavelengths λ between 2.4 μm and 20 μm. It indicates that water had an emittance $\varepsilon_{n,\lambda}$ slightly larger than the acrylic for $\lambda < 15$ μm and slightly lower for $\lambda > 15$ μm.

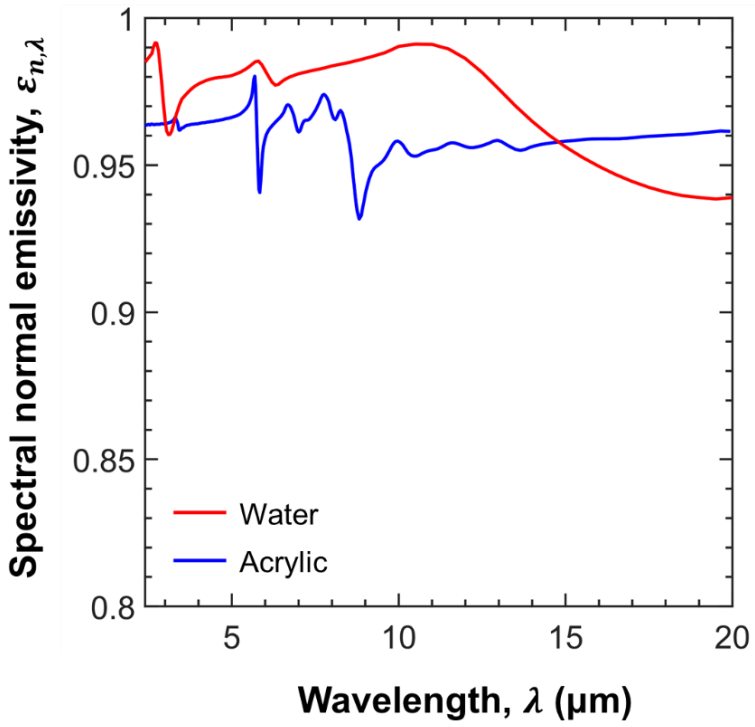

Figure 5.4. Spectral normal emissivity $\varepsilon_{n,\lambda}$ of the water and acrylic for wavelengths between 2.4 and 20 μm.

However, the total normal emissivities ε_n of the water and acrylic were both large, similar, and equal to 0.97 and 0.96, respectively. In addition, the total normal emissivities $\varepsilon_{n,LWIR}$ inside the atmospheric transparency window of the water and acrylic slabs were 0.99 and 0.96, respectively. Similarly, the ratio of the total normal emissivity inside and outside of the atmospheric transparency window ($\varepsilon_{n,LWIR}/\varepsilon_{n,non\text{-}LWIR}$) for water and acrylic were near unity, indicating that both water and acrylic are broadband emitters.

Figure 5.5 shows the spectral normal emittance $\varepsilon_{n,\lambda}$ of the dry soda-lime glass and soda-lime glass supporting acrylic or water droplets on their front side with droplet contact angle (a) θ_c = 30°, (b) θ_c = 60°, and (c) θ_c = 90° and surface area coverage f_A = 52% for wavelengths λ between 5 μm and 20 μm. Figure 5.5 indicates that the emittance $\varepsilon_{n,\lambda}$ of the dry glass increased slightly in the presence of acrylic or water droplets. In addition, it shows that the glass surface had slightly larger emittance $\varepsilon_{n,\lambda}$ when covered with water droplets than with acrylic droplets for droplet contact angle θ_c = 30°. However, for θ_c = 60° and θ_c = 90°, the emissivities $\varepsilon_{n,\lambda}$ of the glass surface supporting water or acrylic droplets were nearly identical. This was due to the fact that absorption of the radiation by the acrylic droplets increased with increasing contact angle θ_c as the droplet volume increased. Table 5.1 summarizes the total normal emittance ε_n and the emittance $\varepsilon_{n,LWIR}$ inside the atmospheric transparency window of the dry glass and glass supporting acrylic or water droplets.

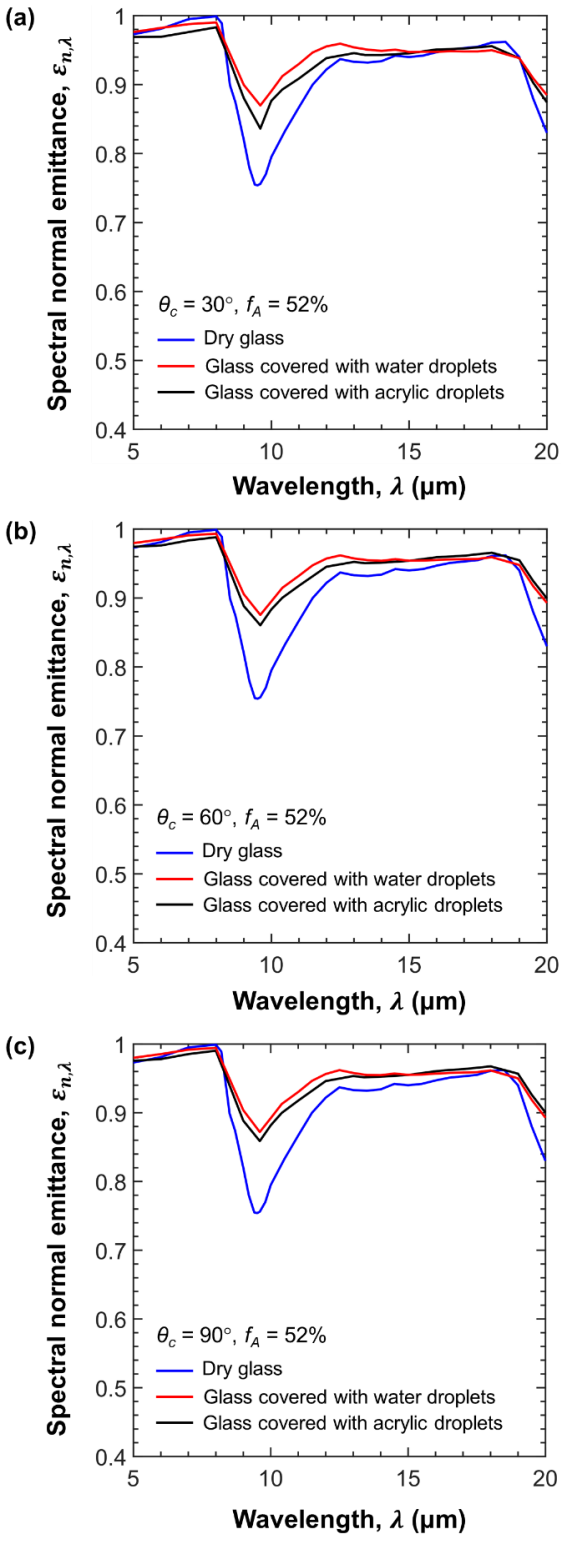

Figure 5.5. Spectral normal emittance $\varepsilon_{n,\lambda}$ of dry glass and glass covered with water or acrylic droplets with f_A = 52% and (a) θ_c = 30°, (b) θ_c = 60°, and (c) θ_c = 90°.

Table 5.1. Emittances of the dry glass and glass supporting acrylic or water droplets.

Droplet	**Droplet contact angle θ_c (°)**	**Total normal emittance ε_n**	**Emittance in atmospheric transparency window $\varepsilon_{n,LWIR}$ (-)**
N/A	N/A	0.91	0.87
Acrylic	30	0.93	0.91
Acrylic	60	0.94	0.92
Acrylic	90	0.94	0.92
Water	30	0.95	0.92
Water	60	0.95	0.93
Water	90	0.95	0.93

Similarly, Figure 5.6 plots the spectral normal emittance $\varepsilon_{n,\lambda}$ of the dry aluminum and aluminum supporting acrylic or water droplets on their front side with (a) θ_c = 30°, (b) θ_c = 60°, and (c) θ_c = 90° and f_A = 52% for wavelengths λ between 2 μm and 20 μm. Figure 5.6 indicates that the emittance $\varepsilon_{n,\lambda}$ of the dry aluminum increased drastically in the presence of either acrylic or water droplets. It also indicates that aluminum had larger spectral emittance $\varepsilon_{n,\lambda}$ when covered with water droplets than with acrylic droplets for θ_c = 30°. The difference in the emittance $\varepsilon_{n,\lambda}$ of the acrylic and water droplet covered surfaces decreased with increasing contact angle θ_c. Table 5.2 summarizes the total normal emittance ε_n and the emittance $\varepsilon_{n,LWIR}$ inside the atmospheric transparency window of the dry aluminum and aluminum supporting acrylic or water droplets. Overall, these results demonstrate that the optical effect caused by the presence of water droplets on the radiative cooling surface is similar to that of acrylic droplets. Thus, acrylic droplets can be used as an easier surrogate to water droplets.

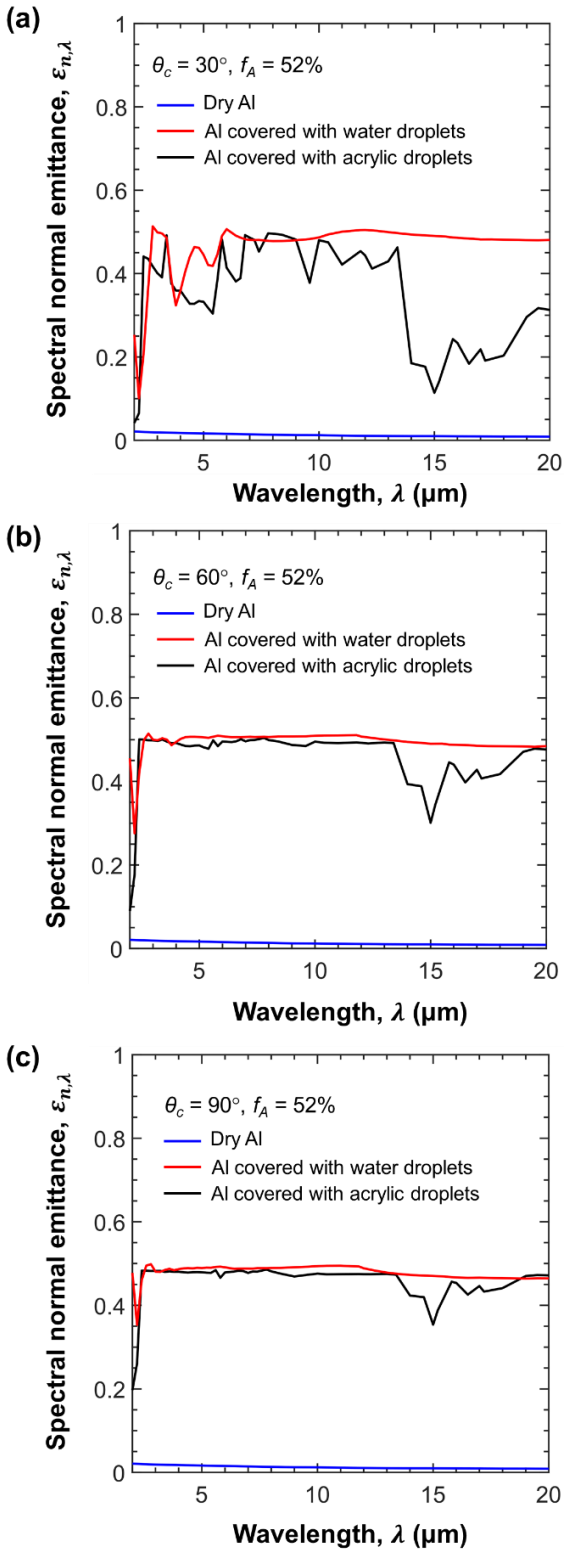

Figure 5.6. Spectral normal emittance $\varepsilon_{n,\lambda}$ of dry aluminum (Al) and Al covered with water or acrylic droplets with f_A = 52% and (a) θ_c = 30°, (b) θ_c = 60°, and (c) θ_c = 90°.

Table 5.2. Emittances of the dry aluminum and aluminum supporting acrylic or water droplets.

Droplet	**Droplet contact angle θ_c (°)**	**Total normal emittance ε_n**	**Emittance in atmospheric transparency window $\varepsilon_{n,LWIR}$ (-)**
N/A	N/A	0.01	0.01
Acrylic	30	0.37	0.45
Acrylic	60	0.47	0.49
Acrylic	90	0.46	0.47
Water	30	0.48	0.49
Water	60	0.49	0.49
Water	90	0.48	0.48

5.3 Results and discussion

5.3.1 Sample characterization

Table 5.3 summarizes the mean droplet contact angle $\bar{\theta}_c$, projected diameter d_p, and surface area coverage f_A of the dry and droplet-covered samples investigated in this chapter. The droplet mean contact angle was (i) $\bar{\theta}_c = 39.0 \pm 2.9°$ for the uncoated Samples 1-5, (ii) $\bar{\theta}_c = 50.2 \pm 1.4°$ for Samples 6-7B coated with NeverWet™, and (iii) $\bar{\theta}_c = 62.3 \pm 4.0°$ for Samples 8-10B coated with perfluorinated silane. The droplet contact angle measurements of the samples are reported in Figure D.1 in Appendix. The droplet surface area coverage f_A of the droplet-covered samples ranged between 20% and 52% while the droplet mean diameter ranged between 384 μm and 711 μm. The next two sections discuss the experimental measurements of the emittance and the outdoor nighttime temperature of the dry and droplet-covered samples.

Table 5.3. Summary of the characteristics of the dry and acrylic droplet-covered radiative cooling samples used in this chapter.

Sample #	Surface treatment	Droplet contact angle $\overline{\theta}_c$ (°)	Surface area coverage f_A (%)	Projected diameter $\overline{d}_p \pm \sigma$ (μm)	Total normal emittance $\varepsilon_{n,t}$ (-)	Emittance in atmospheric transparency window $\varepsilon_{n,LWIR}$ (-)
1	None	N/A	0	-	0.69	0.88
2	None	N/A	100	300 (film)	0.95	0.96
3	None	39.0 ± 2.9	22 ± 5	541 ± 158	0.74	0.89
4	None	39.0 ± 2.9	40 ± 5	417 ± 163	0.79	0.90
5	None	39.0 ± 2.9	50 ± 5	384 ± 166	0.81	0.91
6	NeverWet™	50.2 ± 1.4	0	-	0.75	0.89
7A	NeverWet™	50.2 ± 1.4	40 ± 5	711 ± 212	0.81	0.91
7B	NeverWet™	50.2 ± 1.4	51 ± 5	575 ± 293	0.83	0.92
8	perfluorinated silane	62.3 ± 4.0	0	-	0.71	0.88
9	perfluorinated silane	62.3 ± 4.0	20 ± 5	462 ± 137	0.76	0.90
10A	perfluorinated silane	62.3 ± 4.0	40 ± 5	475 ± 196	0.81	0.91
10B	perfluorinated silane	62.3 ± 4.0	52 ± 5	412 ± 212	0.84	0.93

5.3.2 Infrared characterization

5.3.2.1 Spectral normal emittance

Figure 5.7 plots the spectral normal emittance $\varepsilon_{n,\lambda}$ between 2 and 20 μm for the dry radiative cooling surface (Sample 1), the sample covered with a 300 mm thick acrylic film (Sample 2), and acrylic droplet-covered samples with (a) $\bar{\theta}_c$ = 39° and f_A = 22, 40, and 50% (Samples 3, 4, 5), (b) $\bar{\theta}_c$ = 50.2° and f_A = 0, 40, and 51% (Samples 6, 7A, 7B), and (c) $\bar{\theta}_c$ = 62.3° and f_A = 0, 20, 40, and 52% (Samples 8, 9, 10A, 10B). Figure 5.7(a) shows that the reference sample (Sample 1) had a high spectral normal emittance $\varepsilon_{n,\lambda}$ in the atmospheric transparency window (8 μm ≤ λ ≤ 13 μm) while it featured a lower $\varepsilon_{n,\lambda}$ in the rest of the spectrum. It establishes that the dry sample was a selective emitter. Figure 5.7 indicates that increasing the droplet surface area coverage f_A increased the emittance $\varepsilon_{n,\lambda}$ for any given contact angle considered. This was attributed to the fact that the number of photons absorbed by the acrylic droplets increased as the droplet surface area coverage f_A and the volume of droplets deposited increased. Note that the presence of droplets did not significantly increase the spectral normal emittance $\varepsilon_{n,\lambda}$ for wavelength λ between 7 and 11 μm as the dry sample already featured a large emittance. In addition, Figure 5.7(a) shows that the spectral normal emittance $\varepsilon_{n,\lambda}$ was constant and approached unity for wavelengths λ ≥ 6 μm for surface area coverage f_A = 100%. For the sake of completeness, Figure D.2 in Appendix plots the measured spectral normal-hemispherical reflectance $R_{nh,\lambda}$ of all samples.

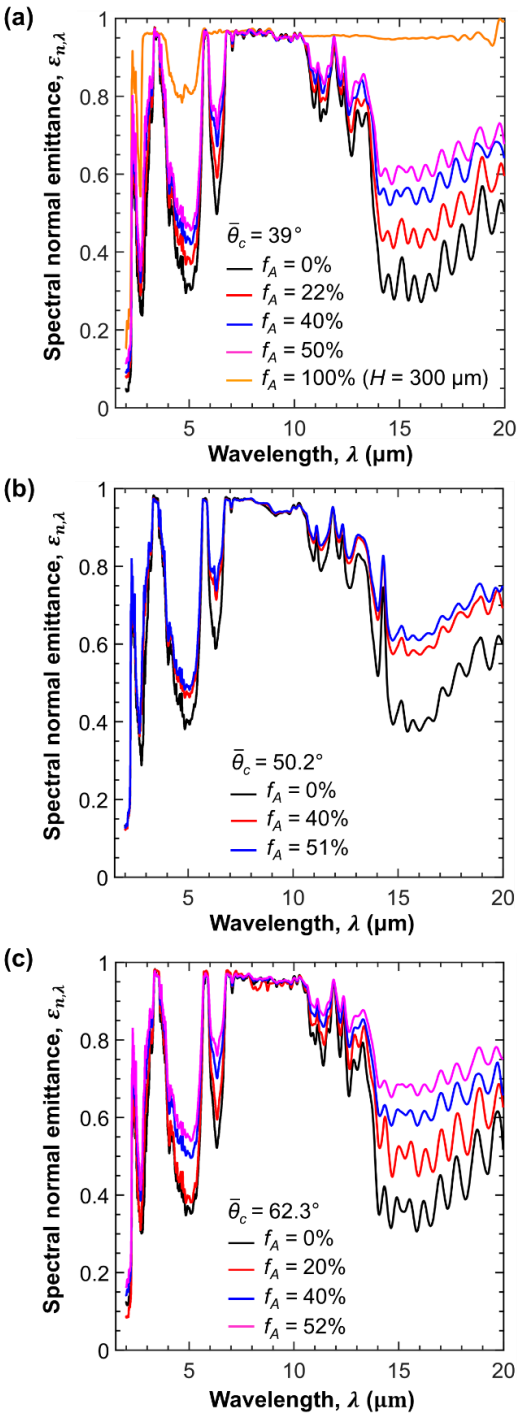

Figure 5.7. Spectral normal emittance $\varepsilon_{n,\lambda}$ as a function of wavelength λ for dry sample (Sample 1), sample covered with 300 mm thick acrylic film (Sample 2), and droplet-covered samples with (a) contact angle $\bar{\theta}_c$ = 39° and surface area coverage f_A between 22% and 50% (Samples 3 - 5), (b) $\bar{\theta}_c$ = 50.2° and f_A between 0% and 51% (Samples 6 - 7B), and (b) $\bar{\theta}_c$ = 62.3° and f_A between 0% and 52% (Samples 8 - 10B).

Figure 5.8 plots the spectral normal emittance $\varepsilon_{n,\lambda}$ as a function of wavelength λ for the dry and droplet-covered samples with droplet contact angles $\bar{\theta}_c$ ranging from 39° to 62.3° and surface area coverage (a) f_A = 0% (Sample 1, 6, 8), (b) f_A = 40% (Sample 3, 7A, 10A), and (c) $f_A \approx 51 \pm 1\%$ (Sample 4, 7B, 10B). Figure 5.8(a) indicates that the presence of silane coating did not affect significantly the spectral normal emittance $\varepsilon_{n,\lambda}$ of the SLL tape on Al sample. By contrast, the spectral normal emittance $\varepsilon_{n,\lambda}$ of the SLL tape on Al sample increased for $\lambda \geq 13$ μm when coated with NeverWet™. Moreover, Figures 5.8(b) and 5.8(c) indicate that, for a given surface area coverage f_A, the spectral normal emittance $\varepsilon_{n,\lambda}$ increased as the droplet contact angle $\bar{\theta}_c$ increased from 39° to 62.3°. This was attributed to absorption by the droplets since the volume of the droplets increased with increasing contact angle $\bar{\theta}_c$.

5.3.2.2. Total and atmospheric normal emittance

Figure 5.9 plots the calculated (a) total normal emittance ε_n, (b) normal emittance $\varepsilon_{n,LWIR}$ inside the atmospheric transparency window, (c) normal emittance outside the atmospheric transparency window $\varepsilon_{n,non-LWIR}$, and (d) ratio of $\varepsilon_{n,LWIR}$ to $\varepsilon_{n,non-LWIR}$ as functions of surface area coverage f_A for dry sample (Sample 1), sample covered with 300 mm thick acrylic film (Sample 2) and droplet-covered samples with droplet contact angle $\bar{\theta}_c$ = 39° (Samples 3, 4), $\bar{\theta}_c$ = 50.2° (Samples 5, 6, 7A, 7B), and $\bar{\theta}_c$ = 62.3° (Samples 8, 9, 10A, 10B). Figure 5.9(a) indicates that the total normal emittance ε_n [Equation (5.2) for θ_i = 0°] increased almost linearly with increasing droplet surface area coverage f_A for all droplet contact angles considered, as illustrated with the solid line connected the emittance for Sample 1 and 2. This was attributed to the fact that absorption by the droplets increased with increasing surface area coverage f_A.

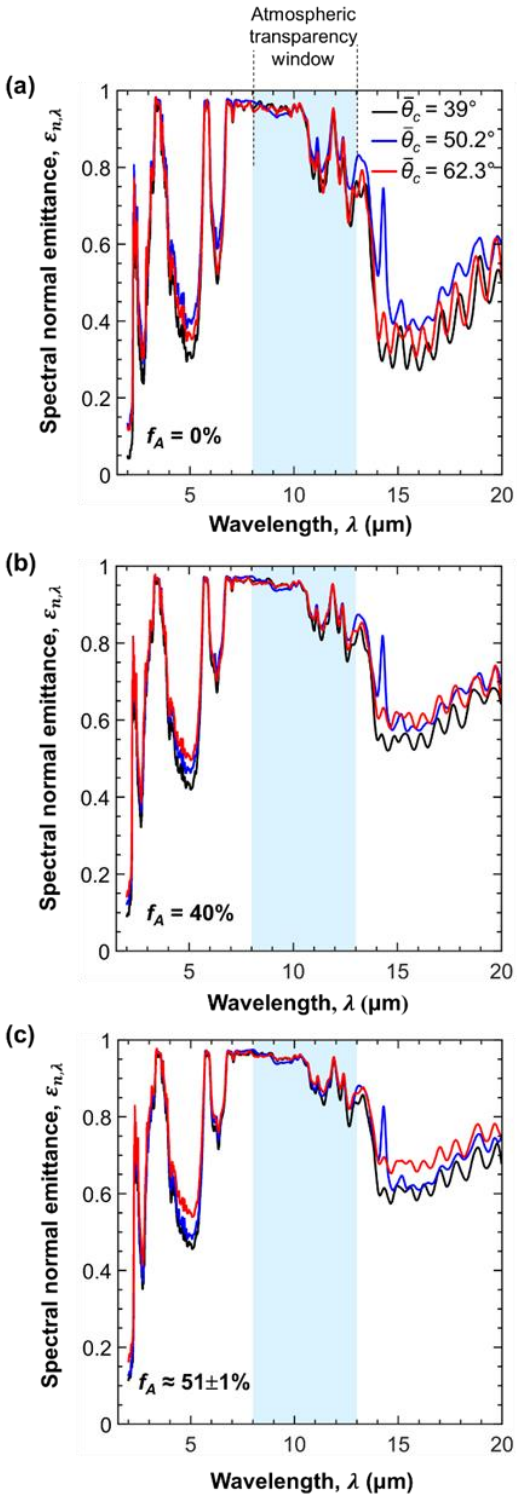

Figure 5.8. Spectral normal emittance $\varepsilon_{n,\lambda}$ for (a) dry samples (Samples 1, 6, 8) and droplet-covered samples with contact angle $\bar{\theta}_c$ = 39°, 50.2°, and 62.3° and surface area coverage, (b) f_A = 40% (Samples 4, 7A, and 10A), and (c) $f_A \approx 51 \pm 1\%$ (Samples 5, 7B, and 10B).

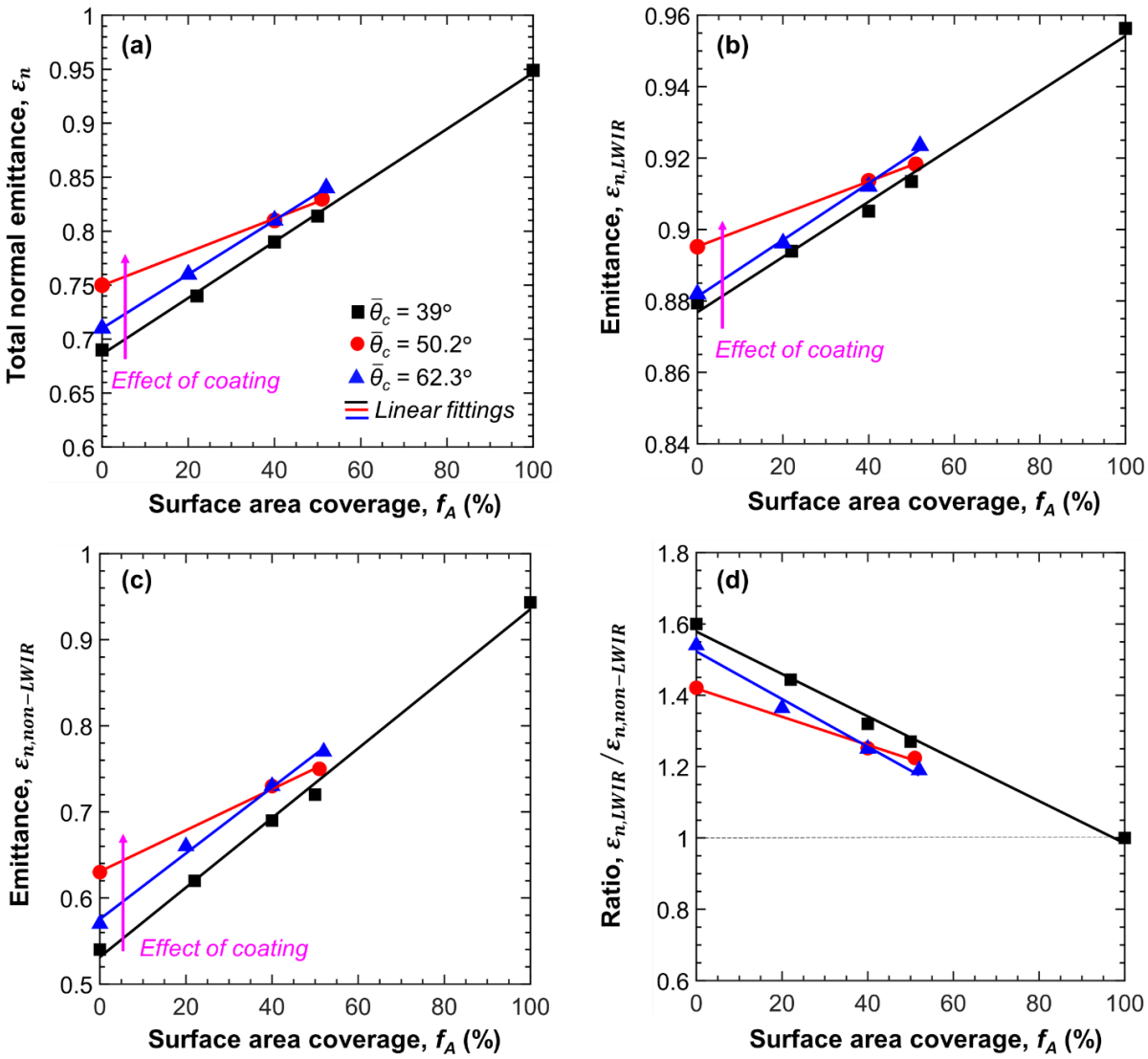

Figure 5.9. (a) Total normal emittance ε_n (b) normal emittance $\varepsilon_{n,LWIR}$ inside the atmospheric transparency window, (c) normal emittance $\varepsilon_{n,non\text{-}LWIR}$ outside the atmospheric transparency window, and (d) ratio of the emittance $\varepsilon_{n,LWIR}/\varepsilon_{n,non\text{-}LWIR}$ as functions of surface area coverage f_A for contact angles $\bar{\theta}_c$= 39°, 50.2°, and 62.3°.

In addition, Figure 5.9(b) indicates that the emittance $\varepsilon_{n,LWIR}$ inside the atmospheric transparency window increased slightly in the presence of droplets as the dry sample had already a large emittance $\varepsilon_{n,LWIR}$ of 0.88. Larger emittance inside the atmospheric transparency window $\varepsilon_{n,LWIR}$ is desired as it increases the radiative cooling [145]. Note that Table 5.3 summarizes the

total normal emittance ε_n and the emittance $\varepsilon_{n,LWIR}$ inside the atmospheric transparency window of the samples used in this chapter. Figure 5.9(c) shows that the normal emittance $\varepsilon_{n,non-LWIR}$ outside the atmospheric transparency window [Equation (5.4) for θ_i = 0°] increased significantly with increasing surface area coverage f_A. An increase in $\varepsilon_{n,non-LWIR}$ is undesired as it increases the absorption of radiation from ambient [31].

Figures 5.9(a) and 5.9(b) also show that dry samples (f_A = 0%) had different emittances ε_n and $\varepsilon_{n,LWIR}$ [Table 5.3] due to the presence of the NeverWet™ and silane coatings. This could be due to the fact that the silane ($\bar{\theta}_c$= 62.3˚) and NeverWet™ ($\bar{\theta}_c$= 50.2˚) coatings applied on the samples are themselves either broadband emissive or may have an antireflection effect. Moreover, to evaluate the selectivity of the radiative emitters [146], the ratio of emittance inside to outside the atmospheric transparency window [$\varepsilon_{n,LWIR}/\varepsilon_{n,non-LWIR}$] was plotted in Figure 5.9(d). It indicates that the ratio of emittance inside to outside the atmospheric transparency window [$\varepsilon_{n,LWIR}/\varepsilon_{n,non-LWIR}$] decreased in the presence of the droplets due to the larger increase in $\varepsilon_{n,LWIR}$. In the atmospheric transparency window (8 μm ≤ λ ≤ 13 μm), photons were mostly absorbed by the SLL tape on Al sample. However, for the wavelength λ > 13 μm, photons that reached the SLL tape on the Al sample were mostly reflected towards the droplets. As a result of the multiple reflections, more photons were absorbed by the droplets resulted in a larger increase in $\varepsilon_{n,non-LWIR}$. The ratio of emittance inside to outside the atmospheric transparency window [$\varepsilon_{n,LWIR}/\varepsilon_{n,non-LWIR}$] decreased to unity as surface area coverage f_A reached 100% such that the radiative emitter turns from selective to the broadband emitter.

5.3.2.3 Total and atmospheric directional emittance

Figure 5.10 shows the calculated (a, b) total directional emittance ε_d and (c,d) directional emittance $\varepsilon_{d,LWIR}$ inside the atmospheric transparency window as functions of incident angle θ_i for the dry

and droplet-covered samples with (a) $\bar{\theta}_c = 39°$ and f_A ranging from 0% to 50% (Sample 1, 3, 5) and $\bar{\theta}_c = 62.3°$ and f_A between 0% and 52% (Sample 8, 9, 10B).

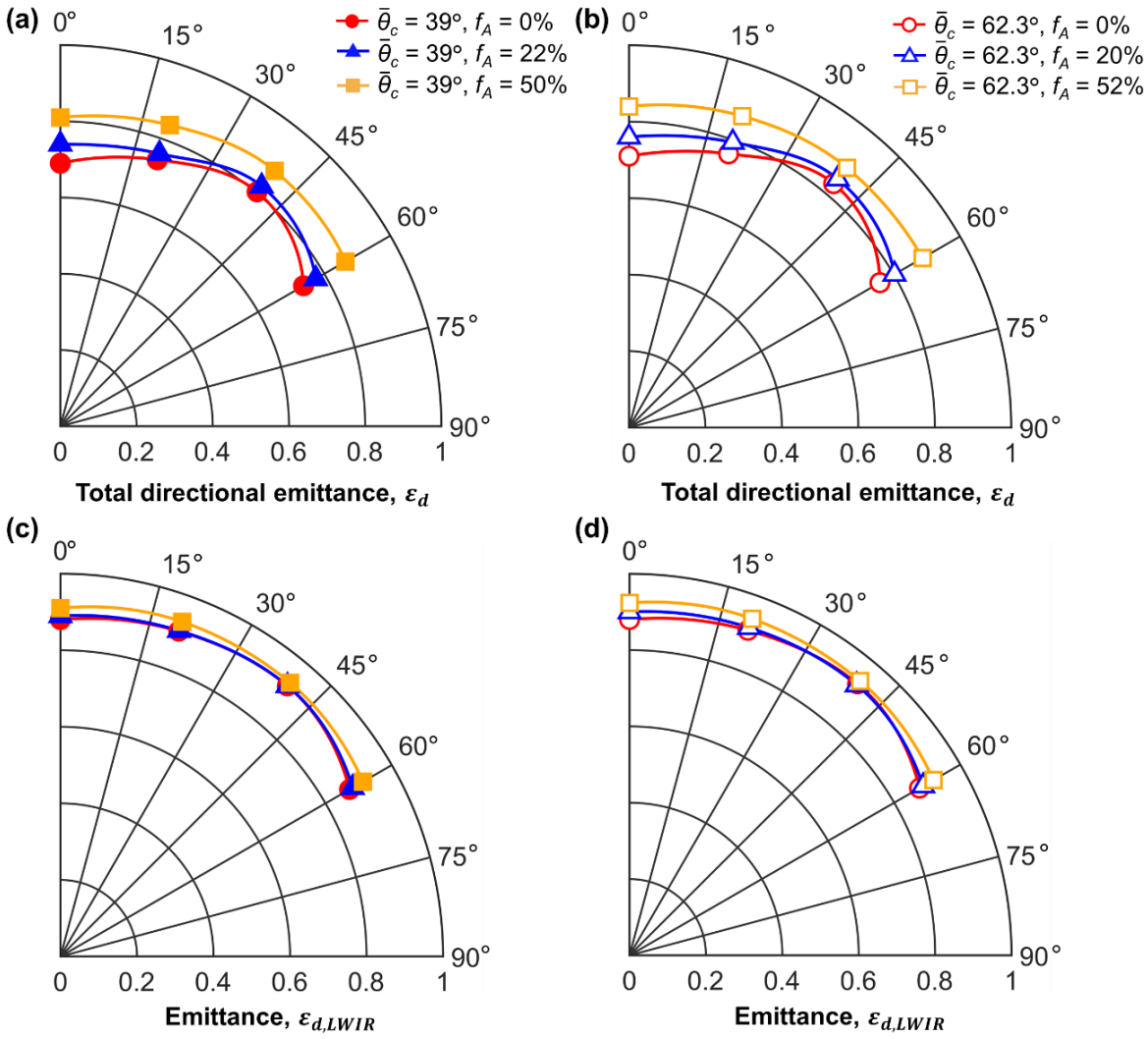

Figure 5.10. (a, b) Total directional emittance ε_d and (c, d) directional emittance in the atmospheric transparency window $\varepsilon_{d,LWIR}$ as functions of incident angle θ_i for dry and droplet-covered samples with droplet contact angle $\bar{\theta}_c$= 39°and 62.3° and surface area coverage between f_A = 0% and 52%.

Note that the spectral directional emittances $\varepsilon_{d,\lambda}$ at incident angles θ_i = 0°, 20°, 40°, and 60° used to compute ε_d and $\varepsilon_{d,LWIR}$ are plotted in Figure D.3 in Appendix. Figures 5.10(a) and 5.10(b) indicate that the total directional emittance ε_d of the dry and droplet-covered samples initially

increased with increasing incident angle θ_i and reached a maximum at θ_i = 40° before decreasing at θ_i = 60°. These results are qualitatively consistent with measurements reported by Huang et al.[68] for the reference sample. The emittance for the dry sample peaking at incident angle θ_i = 40° is likely due to two competing effects namely (i) its surface reflectivity increased with incident angle θ_i and (ii) its emittance increasing with incident angle θ_i due to the increased in optical thickness of the emissive SLL tape. In addition, the total directional emittance ε_d increased with increasing surface area coverage f_A for all incident angles θ_i considered due to absorption by droplets. However, directional emittance inside the atmospheric transparency window $\varepsilon_{d,LWIR}$ remained unchanged in the presence of droplets for all incident angles θ_i considered, as shown in Figures 5.10(c) and 5.10(d). Moreover, Figure 5.10 indicates that SLL tape on Al sample had large $\varepsilon_{d,LWIR}$ even at larger incident angles.

5.3.3 Outdoor nighttime demonstration

Figure 5.11 shows the measured temperature T of the dry and droplet-covered samples as a function of time t for $\bar{\theta}_c$ = 39° and f_A = 52% on (a) April 28, (b) May 21, (c) September 1, and (d) October 12, 2021. Note that the outdoor nighttime experiments were conducted on different months with different sky and humidity conditions to explore a wide range of realistic situations. Figure 5.11 indicates that the dry and droplet-covered samples had a lower temperature than the air due to the radiative cooling under the clear sky and partially cloudy conditions. The dry and droplet-covered samples had a slightly higher temperature than the air under cloud coverage, as observed in Figure 5.11(b). This could be attributed to the fact that the clouds obstructed the view to the sky. Then, the radiative heat transfer exchanges occurred between the samples and the clouds that were warmer than the clear sky, resulting in a higher sample temperature.

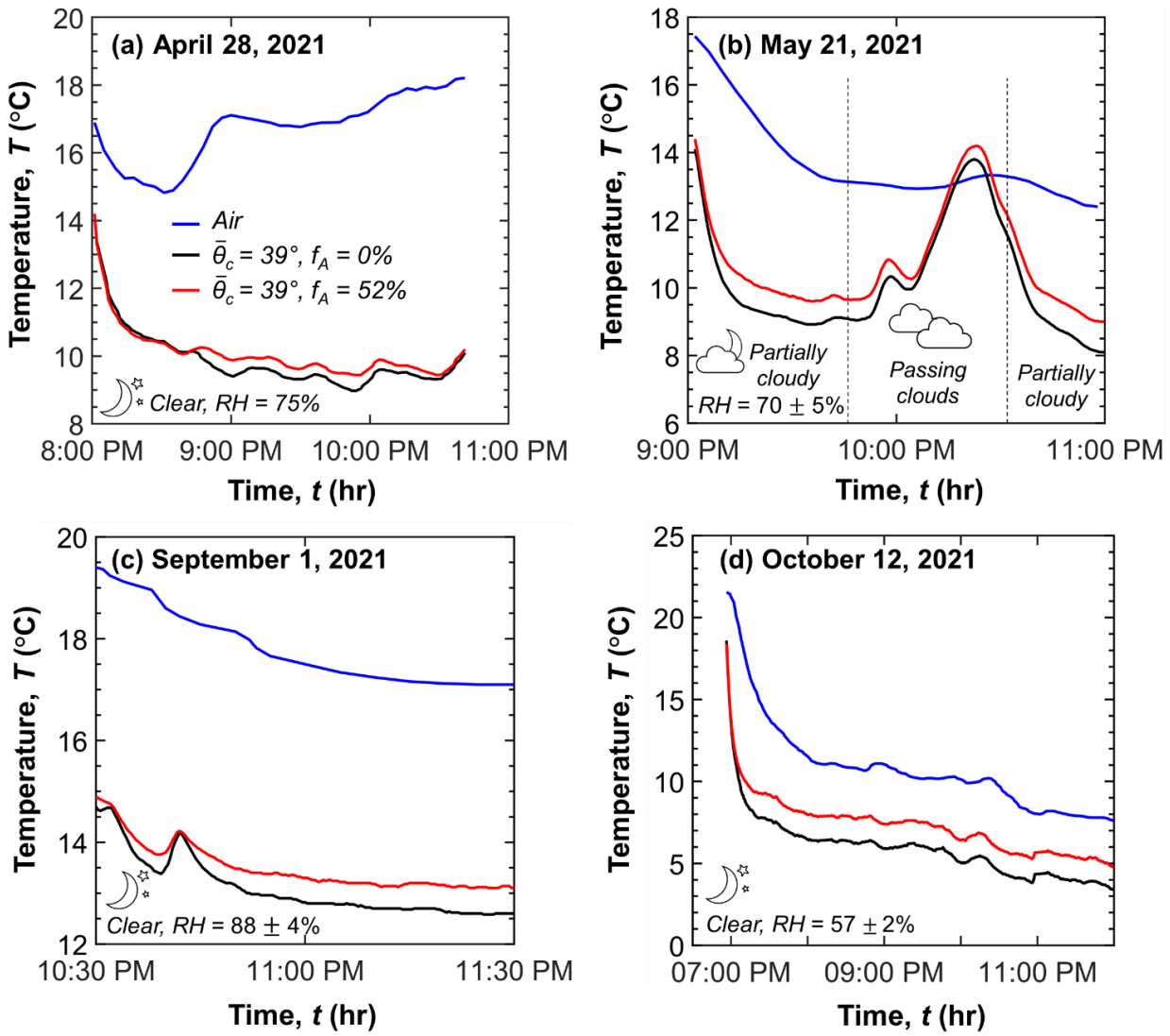

Figure 5.11. Temperature T as a function of time t of the dry (f_A = 0%) and droplet-covered sample with contact angle $\bar{\theta}_c$ = 39° and f_A = 52% at different days.

Moreover, Figure 5.11 indicates that the dry sample had a lower temperature than the droplet-covered sample. The temperature difference between the droplet-covered and dry sample reached 1.7°C, as illustrated in Figure 5.11(d). This can be attributed to the higher selectivity of the dry sample, which prevents undesirable heat gain from the relatively warm atmosphere. Although the dry sample was a selective emitter, it acted as a broadband emitter in the presence of the droplets,

as previously explained. Lower temperatures can be achieved by using a selective emitter, as explained in Refs.[31,142,147].

5.3.4 Extension to vertical radiative cooling surfaces

While this chapter has shown that dropwise condensation can affect the spectral properties of the radiative cooling surfaces to impart a broadband emittance, the dew formation depends on several factors such as the orientation of the surface. Horizontal, sky-facing radiative cooling surfaces that primarily have the sky in view can cool down to low temperatures and collect more dew due to their orientation. Vertically-oriented radiative emitters, which are exposed to both the cold sky and the warm earth, may not sufficiently cool down for dew formation on the surface or condensed droplets may roll-off due to gravity. This was experimentally demonstrated by exposing horizontally and vertically oriented uncoated SLL tape on Al sample to the sky on a humid night in Los Angeles.

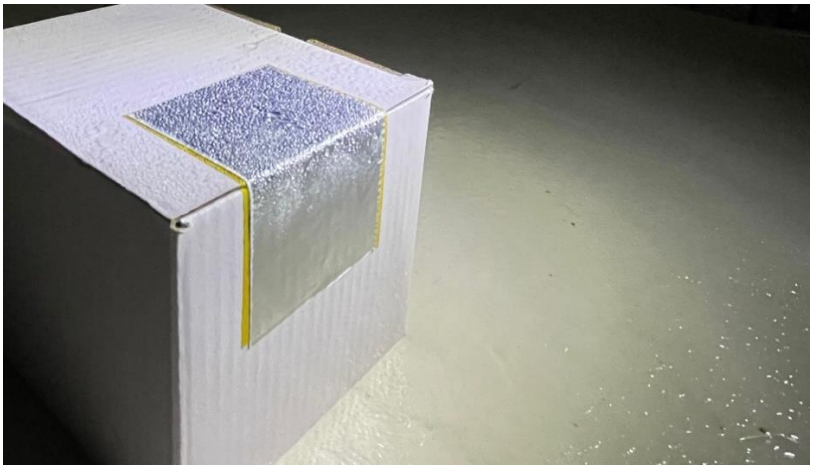

Figure 5.12. Photograph of the selectively emitter taped on a broadband emitter paper box, taken on a humid night in Los Angeles (September 28, 2021, 02:00 AM, T_a = 16°C, RH = 80%). The samples had been exposed to the sky for 2 hours.

Figure 5.12 shows that the horizontal section of the radiative cooling surface facing only the sky was covered with condensed water droplets. However, only a very little amount of water condensation was observed on the vertically oriented section of the radiative cooling surface even after being exposed to a highly humid environment for 2 hours. This is particularly important for building cooling applications, since broadband emitters are sufficiently good radiative cooling surfaces for sky-facing roofs [37], and their use instead of selective emitters would mean that dropwise condensation has little impact. By contrast, broadband emitters on vertical facades like walls and windows suffer from undesirable summertime terrestrial heat gains and wintertime losses. Selective emitters can mitigate this effect to achieve relative seasonal thermoregulation [146], and since dew formation appears unlikelier on vertical surfaces, enable this benefit in both humid and dry environments.

5.4 Conclusion

This chapter experimentally investigated the effect of dropwise condensation on the emittance and selectivity of radiative cooling surfaces. Radiative cooling surfaces with and without hydrophobic coatings were covered with acrylic droplets with droplet surface area coverage f_A between 0 and 52% and droplet mean contact angle $\bar{\theta}_c$ between 39° and 62°. This chapter demonstrated that the droplets significantly increased the spectral normal emittance $\varepsilon_{n,\lambda}$ of the radiative cooling surfaces. It increased with increasing droplet surface area coverage f_A and droplet contact angle $\bar{\theta}_c$. This was attributed to the fact that the absorption by the acrylic droplets increased as the volume of the droplets increased with increasing droplet surface area coverage f_A and/or droplet contact angle $\bar{\theta}_c$. The emittance $\varepsilon_{n,LWIR}$ inside the atmospheric transparency window increased slightly while the emittance $\varepsilon_{n,non-\,LWIR}$ outside the atmospheric transparency window increased significantly in the presence of droplets. Radiation transfer through droplet-covered selective radiative emitter was

controlled by absorption by the SLL tape on Al inside the atmospheric transparency window while it was controlled by absorption by the droplets outside the atmospheric transparency window especially for $\lambda > 13$ μm. In addition, outdoor nighttime experiments showed that the temperature of the radiative cooling surface increased in the presence of droplets due to the undesirable heat gain from the atmosphere. Overall, these results establish dropwise condensation can significantly affect the emittance and selectivity of the radiative cooling surfaces. Hydrophilic coating can be applied to the selective emitters especially for harvesting atmospheric water as it can limit the negative effect of the droplets and facilitate condensation. However, for cooling of vertical facades of buildings, a hydrophobic coating can be preferred as it can keep the selective emitter dry by inhibiting condensation [112].

Chapter 6: Conclusions and Future Work

6.1 Conclusions

The objectives of this dissertation were (1) to investigate the effect of the droplets on the *light* transmittance through semitransparent glass windows supporting pendant droplets on their back side, (2) to investigate the effect of the droplets on the *infrared* radiation transfer through semitransparent glass windows supporting droplets on their back or front sides, (3) to validate the numerical simulations based on the Monte Carlo ray-tracing method, and to extend this investigation to important applications including (4) power generation by PV solar cells and (5) water production by radiative cooling surfaces.

The first objective was achieved by depositing acrylic droplets on the soda-lime glass windows with or without hydrophobic surface treatment. The droplet-covered glass windows were systematically characterized and the normal-hemispherical transmittance and reflectance of these samples were measured in the visible and near-infrared parts of the electromagnetic spectrum when window and droplets are non-absorbing. The spectral normal-hemispherical transmittance $T_{nh,\lambda}$ was independent of surface area coverage f_A and increased slightly with increasing contact angle $\bar{\theta}_c$ for droplet contact angle $\bar{\theta}_c$ smaller than the critical angle θ_{cr} for total internal reflection at the droplet/air interface. However, for droplet contact angle such that $\theta_{cr} \leq \bar{\theta}_c < 90°$, the transmittance $T_{nh,\lambda}$ decreased while the reflectance $R_{nh,\lambda}$ increased with increasing contact angle $\bar{\theta}_c$ and surface area coverage f_A due to total internal reflection at the droplet/air interfaces.

The second objective was achieved by measuring the normal-hemispherical transmittance and reflectance of the glass windows supporting droplets on their back or front side in the infrared part of the electromagnetic spectrum. Radiation transfer through glass windows supporting droplets on

their back side was dominated by total internal reflection at the droplet/air interface and absorption by the glass window and/or the droplets. In the spectral range when the droplets and the glass window were slightly absorbing, the normal-hemispherical transmittance $T_{nh,\lambda}$ was independent of droplet surface area coverage f_A and increased slightly with increasing droplet contact angle $\bar{\theta}_c$ smaller than the critical angle θ_{cr}. However, for droplet contact angles $\bar{\theta}_c \geq \theta_{cr}$, the transmittance $T_{nh,\lambda}$ decreased with increasing contact angle $\bar{\theta}_c$ and surface area coverage f_A due to total internal reflection at the droplet/air interface. In the spectral range when the droplets were strongly absorbing and the glass was weakly absorbing, the transmittance $T_{nh,\lambda}$ decreased with increasing droplet contact angle $\bar{\theta}_c$ and surface area coverage f_A due to absorption by both the droplets and the glass. In the spectral range when the glass window was strongly absorbing, the transmittance $T_{nh,\lambda}$ vanished while the reflectance $R_{nh,\lambda}$ was independent of droplet contact angle $\bar{\theta}_c$ and surface area coverage f_A. Radiation transfer through glass windows supporting droplets on their front side was controlled by the antireflecting effects of droplets and by absorption by the droplets and/or the glass window. In the spectral range when the droplets and the glass window were slightly absorbing, the transmittance $T_{nh,\lambda}$ increased while the reflectance $R_{nh,\lambda}$ decreased with increasing surface area coverage f_A. In the spectral range when the glass was weakly absorbing and the droplets were strongly absorbing, the transmittance $T_{nh,\lambda}$ decreased with increasing droplet contact angle $\bar{\theta}_c$ and surface area coverage f_A. In the spectral range when the glass was strongly absorbing, the transmittance $T_{nh,\lambda}$ vanished and the reflectance $R_{nh,\lambda}$ decreased with increasing droplet surface area coverage f_A.

The third objective was achieved by predicting the spectral normal-hemispherical transmittance $T_{nh,\lambda}$ and reflectance $R_{nh,\lambda}$ in the visible and infrared by using previously developed numerical code based on the Monte Carlo ray-tracing (MCRT) method. The numerically predicted

transmittance and reflectance of the droplet-covered glass windows were in good agreement with experimental measurements obtained in both the visible and infrared parts of the spectrum.

The fourth objective was achieved by measuring the current vs. voltage curves of polycrystalline silicon solar cells with dry and droplet-covered glass covers under simulated solar irradiation under different incidence angles. The droplets had no effect on the generated current, the maximum power, and the energy conversion efficiency of the solar cells for incident angle $\theta_i \leq 30°$. However, for incident angle $\theta_i > 30°$, the solar cell performance decreased significantly in the presence of droplets. This was due to the fact that incident light was back-scattered through the droplets instead of being trapped due to total internal reflection at the cover/air interface.

The final objective was achieved by preparing and characterizing selective emitters supporting acrylic droplets with different droplet contact angles and surface area coverages. The spectral directional-hemispherical reflectance of the prepared samples was measured in the infrared part of the electromagnetic spectrum. The spectral normal emittance $\varepsilon_{n,\lambda}$ of the radiative cooling surfaces increased with increasing droplet contact angle $\bar{\theta}_c$ and surface area coverage f_A. This was due to the fact that the absorption by the droplets increased as the volume of the droplets increased. In the presence of droplets, the emittance inside the atmospheric transparency window increased slightly while the emittance outside the atmospheric transparency window increased significantly. In addition, outdoor nighttime experiments showed that the temperature of the radiative cooling surface increased in the presence of droplets due to the undesirable radiative heat gain from the atmosphere.

6.2 Future work

6.2.1 Improving existing numerical code

Numerical simulations have been performed to predict the radiation transfer through droplet-covered substrates by using a previously-developed numerical code based on the Monte Carlo ray-tracing method (MCRT) [55,64,66]. The existing numerical code ignores the presence of the coating on the substrate surface. However, experimental measurements reported in Chapters 2 and 3 established that the normal-hemispherical transmittance and reflectance of the droplet-covered substrates were altered by the presence of coatings especially in the visible part of the electromagnetic spectrum. Thus, it will be beneficial to extend the existing numerical code to account for optical interferences occurring in the coatings.

6.2.2 Extending the discussion for superhydrophobic surfaces

Hydrophobic surface treatments including perfluorinated silane, perfluorinated silane-coated silica nanoparticle monolayer, or Teflon coatings have been applied to the glass windows to achieve droplet contact angle ranging from 26° to 77°. Chapter 2 confirmed the existence of optical Regimes I ($\bar{\theta}_c < \theta_{cr}$) and II ($\theta_{cr} \leq \bar{\theta}_c < 90°$) observed in the normal-hemispherical transmittance and reflectance measurements, as defined by Zhu et al.[55]. However, Zhu et al.[55] established the existence of two more regimes, Regime III ($90° \leq \theta_c < 180°-\theta_{cr}$) and Regime IV ($\theta_c \geq 180°-\theta_{cr}$), that have not yet been validated experimentally. Thus, additional transmittance and reflectance measurements should be performed in the visible to confirm the existence of optical Regimes III and IV By depositing different superhydrophobic coatings and micro/nanostructures onto glass windows.

6.2.3 Extending the discussion for non-cap shaped droplets

In this dissertation, the experimental measurements were used to validate the previously developed numerical code that assumed droplets to be cap-shaped. However, condensation may occur over the course of hours and the droplets may merge such that the droplets cannot be assumed to be cap-shaped. Recently, Hoegnies et al.[56] used a numerical code based on the Monte Carlo ray-tracing method to predict the light transfer through horizontal and titled transparent windows supporting pendant non-absorbing and non-cap shaped droplets. This study showed that assuming droplets to be cap-shaped caused the transmittance to be overestimated by up to 37% for droplet volumes $V > 10$ µL and contact angles $\theta_c > \theta_{cr}$. However, the experimental validation of this numerical simulation has not been reported in the literature. Thus, it will be beneficial to experimentally validate the existing numerical code that predicts the normal-hemispherical transmittance of glass windows supporting pendant non-cap-shaped droplets. To do that, larger droplets need to be deposited onto the glass slabs with or without surface treatments. This can be achieved by using a larger tip of the needle. After the deposition, the droplet-covered glass slabs will be placed on a sample holder coupled with a goniometer to alter the tilt angle of the glass slab. Then, this sample holder will be placed under the UV lamp and droplets will be cured. As a result, horizontal and titled glass slabs supporting polydisperse non-cap shaped droplets will be prepared and characterized optically.

6.2.4 Extending the applications to solar stills

In this dissertation, the effect of the presence of droplets on the performance of photovoltaic solar cells and the emittance of radiative cooling surfaces have been investigated experimentally. Another suggestion is to investigate the effect of the droplets on the performance of solar stills that use solar energy to desalinate saline water [148]. To do that, laboratory-scale simulated solar still

will be fabricated and will be placed under the solar simulator. Glass covers with or without surface treatment will be used as a cover for a solar simulator to investigate the effect of the droplet contact angle and surface area coverage. During the experiments, photographs of the glass covers will be taken to estimate the droplet size distribution and surface area coverage by using image analysis software ImageJ. Extending the applications to solar still will be beneficial to understand how droplets affect the transmittance of the glass cover and to improve water production.

APPENDIX A: Supplementary Materials for Chapter 2

A.1 Droplet contact angle

Figure A.1 shows the droplet contact angle of the (i) bare glass slab, and glass slabs coated with (ii) Rain-X®, (iii) perfluorinated silane, (iv) perfluorinated silane-treated monolayer of silica nanoparticles, and (v) Teflon. The contact angles of the several droplets were averaged to find the mean contact angle $\bar{\theta}_c$.

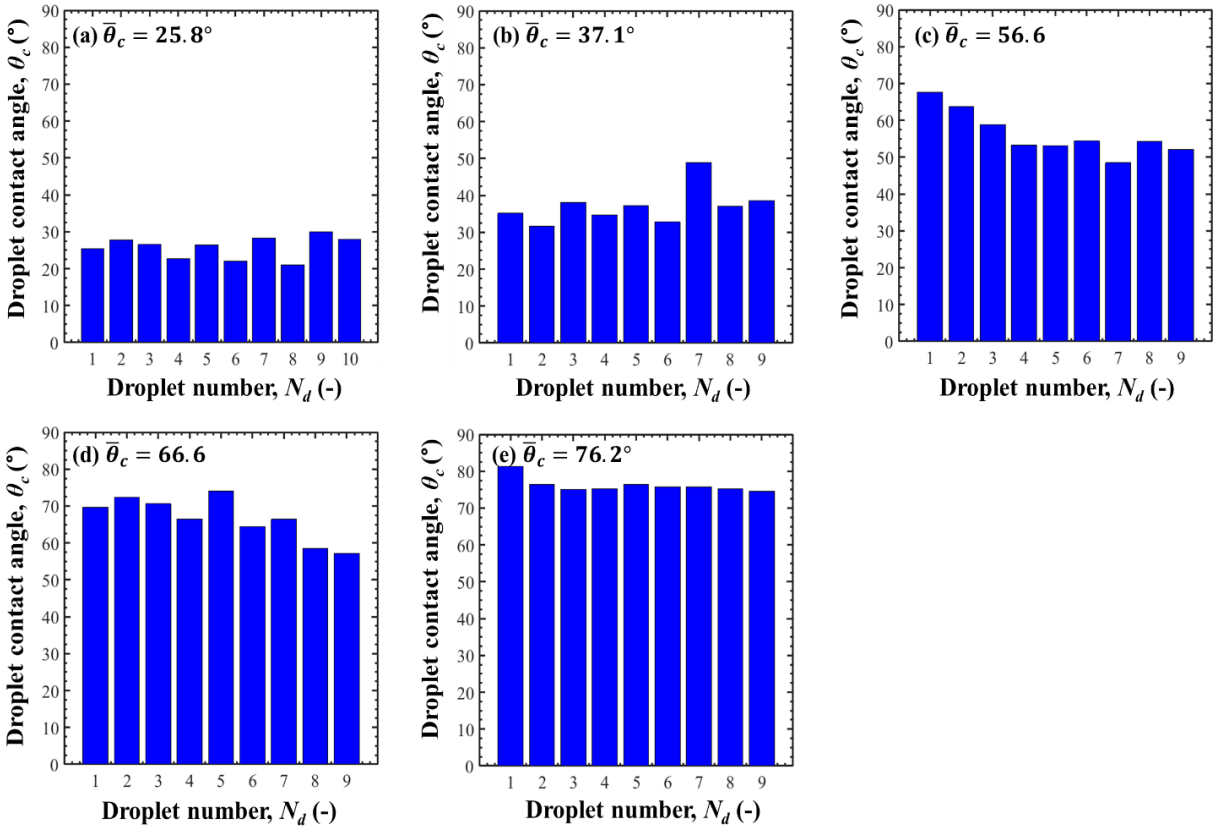

Figure A.1. Droplet contact angle θ_c of the (a) bare glass slab and glass slab coated with (b) Rain-X, (c) perfluorinated silane, (d) perfluorinated silane-treated silica nanoparticle monolayer, and (e) Teflon.

A.2 Microscope images of Sample 2, 4-6, and 9

Figure A.2 shows the microscope images of the acrylic droplets on the (i) bare glass slab and glass slabs coated with (ii) Rain-X®, (iii) perfluorinated silane, (iv) perfluorinated silane-treated monolayer of silica nanoparticles, and (v) Teflon.

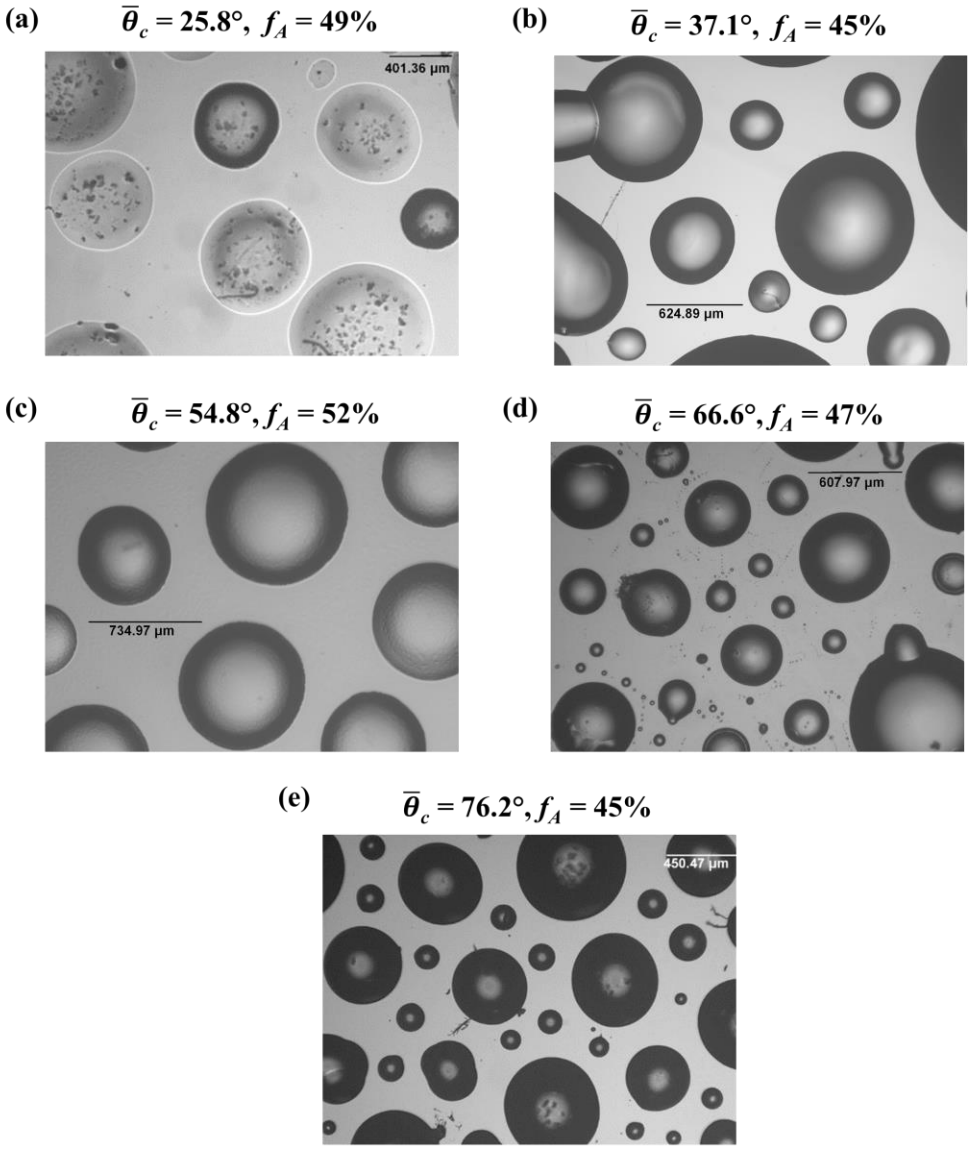

Figure A.2. Microscope images of the acrylic droplets on the (a) clean glass, (b) Rain-X, (c) perfluorinated silane, (d) perfluorinated silane-treated silica nanoparticle monolayer, and (e) Teflon coated glass slabs.

A.3 Droplet size distribution

Figure A.3 shows the droplet size distribution on the bare glass slabs with (a) f_A = 40%, (b) f_A = 49%, (c) f_A = 59%, and (d) Rain-X® coated glass slab, (e) perfluorinated silane coated glass slab, (f) perfluorinated silane-treated silica nanoparticle monolayer coated glass slab, and Teflon coated glass slabs with (g) f_A = 19%, (h) f_A = 34%, and (i) f_A = 45%.

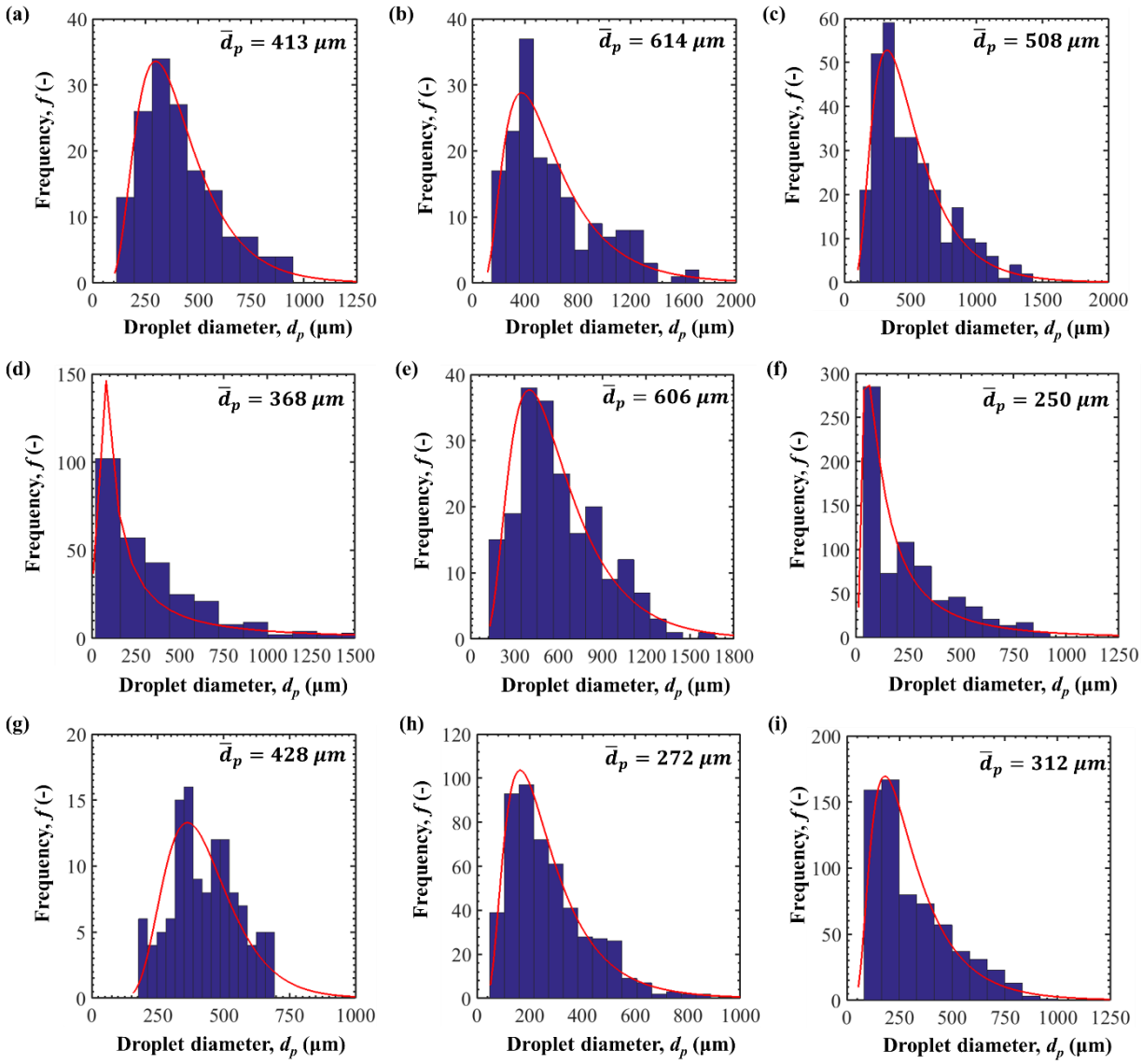

Figure A.3. Droplet size distribution on the bare glass slabs with surface area coverage (a) f_A = 40%, (b) f_A = 49%, (c) f_A = 59%, (d) Rain-X coated glass slab, (e) perfluorinated silane coated glass slab, (f) perfluorinated silane-treated silica nanoparticle monolayer coated glass, Teflon coated glass slabs with (g) f_A = 19%, (h) f_A = 34%, and (i) f_A = 45%.

A.4 Complex index of refraction

Figure A.4 shows the spectral (a) refractive index and (b) absorption index of the soda-lime glass, Teflon AF-2400, acrylic, and air. The refractive index of Teflon AF-2400 was taken from Ref. [83] and its absorption index was retrieved from the measured normal-normal transmittance of a 6.3 mm thick Teflon AF-2400 slab reported in Ref. [84].

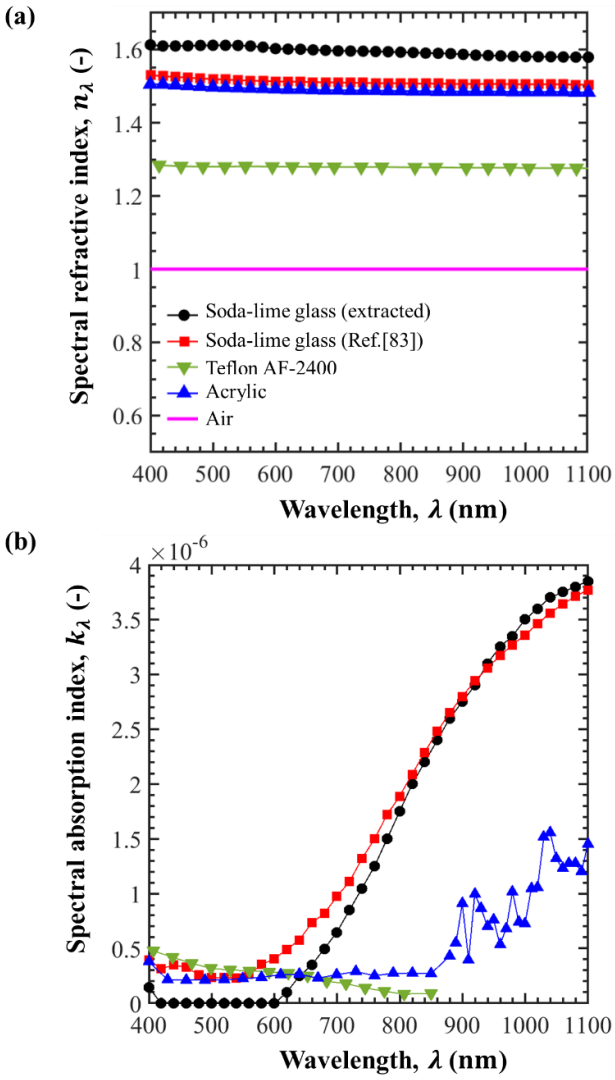

Figure A.4. Spectral (a) refractive index and (b) absorption index $n_{g,\lambda}$ and $k_{g,\lambda}$ of soda-lime glass obtained from measurements and taken from the literature [85] as well as $n_{d,\lambda}$ and $k_{d,\lambda}$ for acrylic obtained from the literature [79,82] along with Teflon AF-2400 [83,84].

A.5 Transmittance, reflectance, and absorptance of dry glass samples

Figure A.5 shows the spectral normal-hemispherical (a) transmittance $T_{nh,\lambda}$ and (b) reflectance $R_{nh,\lambda}$, and (c) the absorptance $A_{nh,\lambda} = 1 - T_{nh,\lambda} - R_{nh,\lambda}$ of the dry glass samples without coating and with Rain-X, perfluorinated silane, perfluorinated silane-treated silica nanoparticles, and Teflon coating.

Figures A.5 (a) and A.5(b) indicate that the normal-hemispherical transmittance increased while the normal-hemispherical reflectance decreased in presence of the coating. This can be attributed to the fact that the presence of the perfluorinated silane ($n = 1.32$) [149] and Teflon film ($n = 1.28$) [83] reduced the index mismatch at the window/air interface and thus reduced the amount of total internal reflection at the back surface of the window. In addition, Figures A.5(c) shows that the absorptance $A_{nh,\lambda} = 1 - T_{nh,\lambda} - R_{nh,\lambda}$ for the dry glass slabs with coating was approximately equal to that of dry glass without coating. It also indicates that absorption by the glass window increased monotonously with wavelengths above 550 nm to reach 13% at 1100 nm.

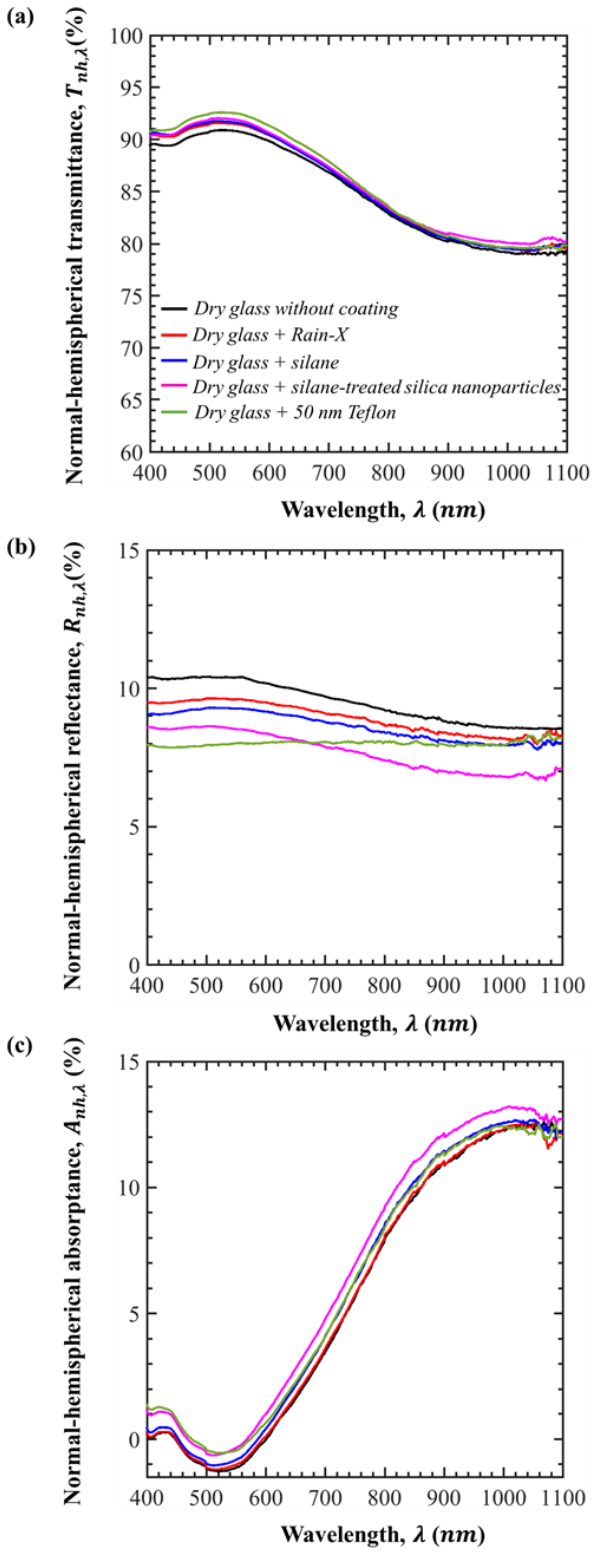

Figure A.5. Spectral normal-hemispherical (a) transmittance $T_{nh,\lambda}$, (b) reflectance $R_{nh,\lambda}$, and (c) absorptance $A_{nh,\lambda}$ as functions of wavelength λ for dry glass with and without coating.

A.6 Effect of droplet refractive index on transmittance

Figure A.6 plots the normal-hemispherical transmittance as a function of droplet contact angle θ_c for windows supporting droplets on their back side with refractive index n_d = 1.33 or 1.6, and surface area coverage f_A = 90% [55].

It indicates that the normal-hemispherical transmittance features the same trends and similar magnitude for both values of n_d considered. Note that the critical angle for internal reflection at the droplet/air interface ($\theta_{cr} = \sin^{-1}(n_a/n_d)$) decreased with increasing droplet refractive index. In addition, the normal-hemispherical transmittance decreased with increasing droplet refractive index in all regimes.

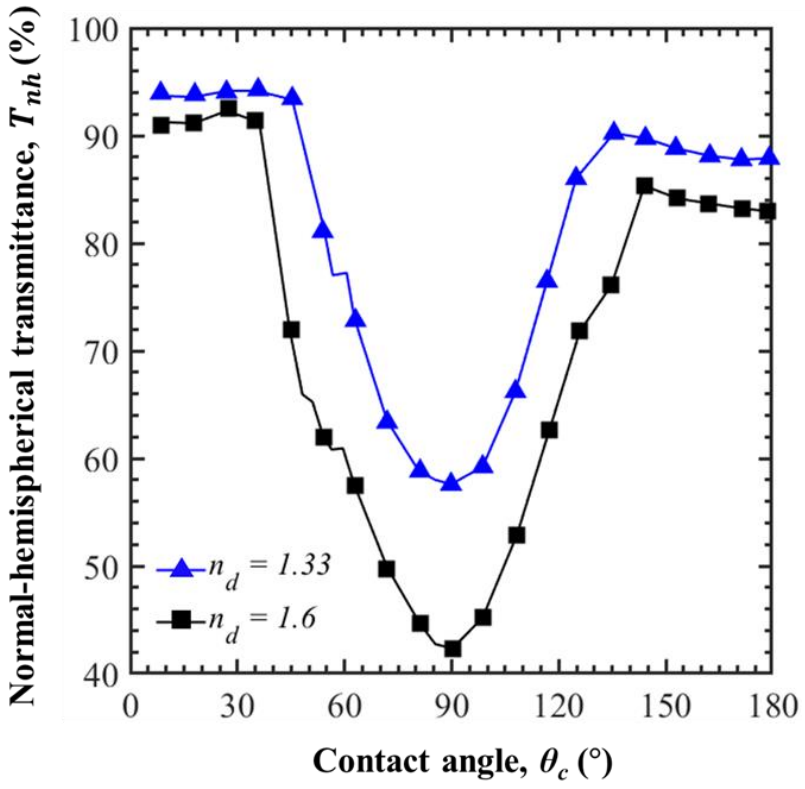

Figure A.6. Comparison of the normal-hemispherical transmittance T_{nh} of droplet-covered windows as a function of droplet contact angle θ_c for droplet refractive index n_d = 1.33 or 1.6, as computed in Ref.[55]. In both cases, the surface area coverage was f_A = 90% and the window refractive index was n_w = 1.5.

A.7 Absorptance of droplet-covered glass samples

Figure A.7 shows the normal-hemispherical absorptance $A_{nh,\lambda}$ of the samples with the droplet contact angle (a) $\bar{\theta}_c < \theta_{cr} = 42°$ and (b) $\theta_{cr} < \bar{\theta}_c \leq 90°$ as well as the corresponding dry sample. The normal-hemispherical absorptance $A_{nh,\lambda}$ of Samples 1–4 ($\bar{\theta}_c < \theta_{cr} = 42°$ - Regime I) was close to that of dry glass, as shown in Figure 0.7(a). However, the normal-hemispherical absorptance $A_{nh,\lambda}$ of Samples 5–9 ($\theta_{cr} < \bar{\theta}_c \leq 90°$ - Regime II) was larger than that of the dry glass.

The observation that, in Regime II, both $R_{nh,\lambda}$ and $A_{nh,\lambda}$ increase with increasing droplet surface area coverage can be attributed to the fact that, unlike in Regime I, droplets in Regime II reflected photons at the droplet/air interface back through the absorbing acrylic droplets and soda-lime glass window, as illustrated in Figures 8(a)-8(b) of Ref.[55]. As a result, more photons were not only reflected but also absorbed by the droplets and the window in the presence of a hydrophobic coating. Note also that the increase in the normal-hemispherical absorptance $A_{nh,\lambda}$ follow similar trends as the increase in the absorption index spectra of the soda-lime glass and acrylic, as shown in Figure A.4(b).

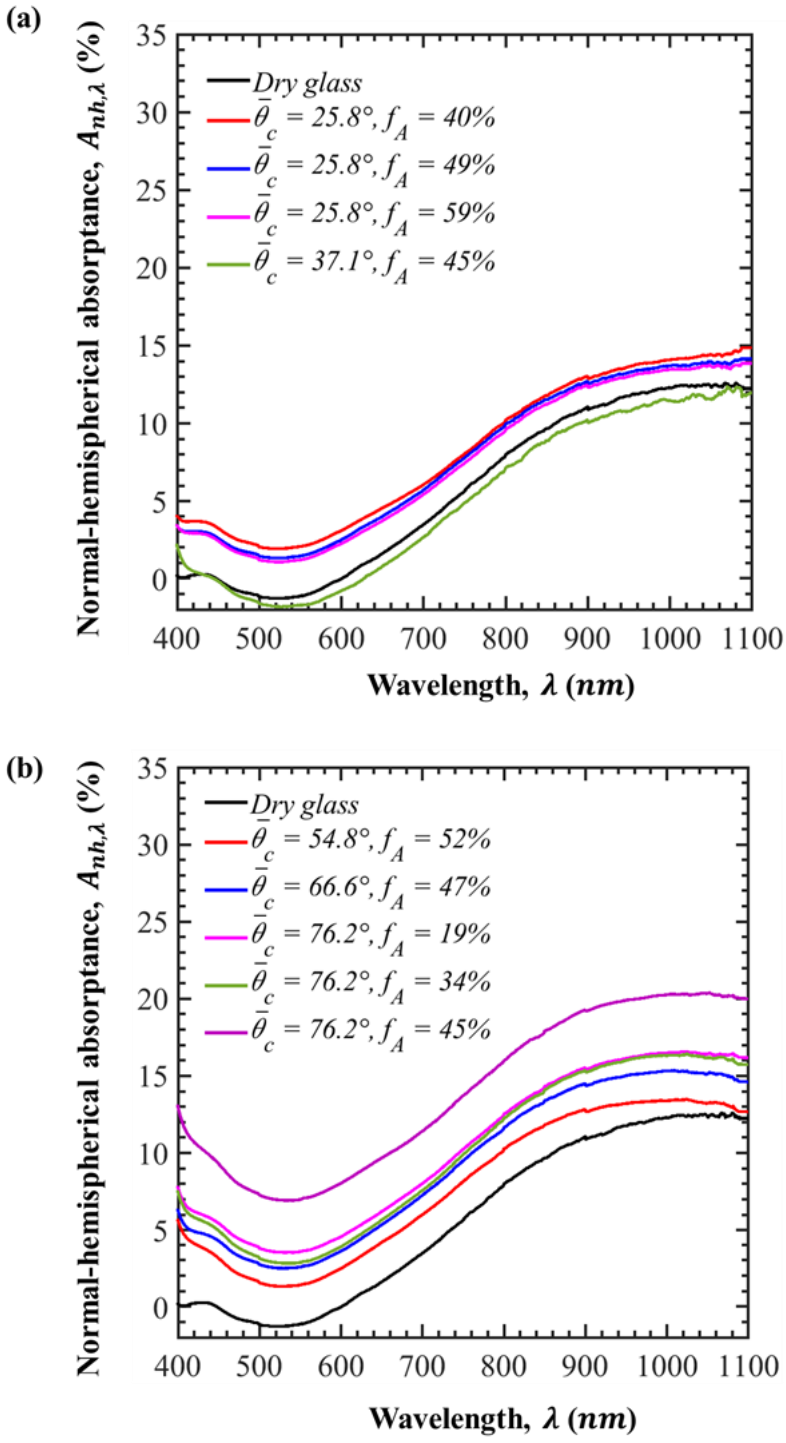

Figure A.7. Normal-hemispherical absorptance $A_{nh,\lambda}$ of the samples with a droplet contact angle (a) $\bar{\theta}_c < \theta_{cr} = 42°$ and (b) $\theta_{cr} < \bar{\theta}_c \leq 90°$.

A.8 Uncertainty analysis

Two main sources of uncertainty, instrumentation and random variation, were considered. Instrumentation uncertainty of the transmittance and reflectance measurements were calculated from the specifications of the UV-Vis spectrophotometer. The accuracy of the contact angle measurements was taken from the specifications of Drop Shape Analyzer. Random variation uncertainty u_r was expressed as [150]

$$u_r = \sigma/\sqrt{N}. \quad \text{(A.1)}$$

Here, σ is the standard deviation and N is the total number of measurements. Individual instrumentation and random variation uncertainties were combined as [150]

$$u_{com} = \sqrt{u_i^2 + u_r^2}. \quad \text{(A.2)}$$

where u_{com} is the combined uncertainty. Expanded uncertainty U was expressed as [150]

$$U = a u_{com}. \quad \text{(A.3)}$$

where a is a coverage factor for a confidence level of 95%. Table A.1 shows the calculated expanded uncertainties of the contact angle, normal-hemispherical transmittance, and reflectance. Expanded uncertainty of the surface area coverage was taken as 5% for all samples.

Table A.1. Uncertainty analysis at wavelength λ = 410 nm.

Sample #	**Contact angle** θ_c **(°)**	**Surface area coverage** f_A **(%)**	**Contact angle uncertainty** U_c **(°)**	**Transmittance uncertainty** U_T **(%)**	**Reflectance uncertainty** U_R **(%)**
Dry glass	N/A	N/A	N/A	1.8	0.6
1	25.8	40	2.2	2.3	0.5
2	25.8	49	2.2	2.5	0.5
3	25.8	59	2.2	2.3	0.4
4	37.1	52	3.8	2.7	0.5
5	54.8	47	4.6	4.4	0.5
6	66.6	47	4.5	2.1	0.9
7	76.2	19	1.6	2.3	0.9
8	76.2	34	1.6	2.2	0.9
9	76.2	45	1.6	2.9	1.3

A.9 Detailed explanation of the total internal reflection at the glass/air interface

Figure A.8 schematically illustrates light transmittance through a glass window featuring pendant droplets on its backside for droplet contact angle (a) $55° < \theta_c < 60°$ and (b) $\theta_c = 60°$. For both cases, the droplet contact angle was larger than the critical angle for total internal reflection at the droplet/air interface ($\theta_{cr} = \sin^{-1}(n_a/n_d) \approx 42.2°$). For $55° < \theta_c < 60°$ [Figure A.8 (a)], photons were reflected back towards to glass/droplet or glass/air interface due to the total internal reflection at the glass/air interface.

The droplet contact angle for total internal reflection at the glass/air interface was predicted using Snell's law [81]

$$n_d \sin(4\theta_c - 180°) = n_g \sin\theta_i = n_a. \quad \text{(A.4)}$$

Here, $4\theta_c - 180°$ and θ_i are the incident angles at the droplet/glass interface and glass/air interface, respectively. The contact angle initiating total internal reflection at the glass/air interface predicted by Equation (A.4) was $\theta_c = 55.5°$. In the end, the photons were transmitted through the glass and droplet, thus normal-hemispherical transmittance and reflectance remained constant. For $\theta_c = 60°$ [Figure A.8(b)], photons were internally reflected at the droplet/air interface and then entered vertically into the glass. As a result, the normal-hemispherical transmittance decreased.

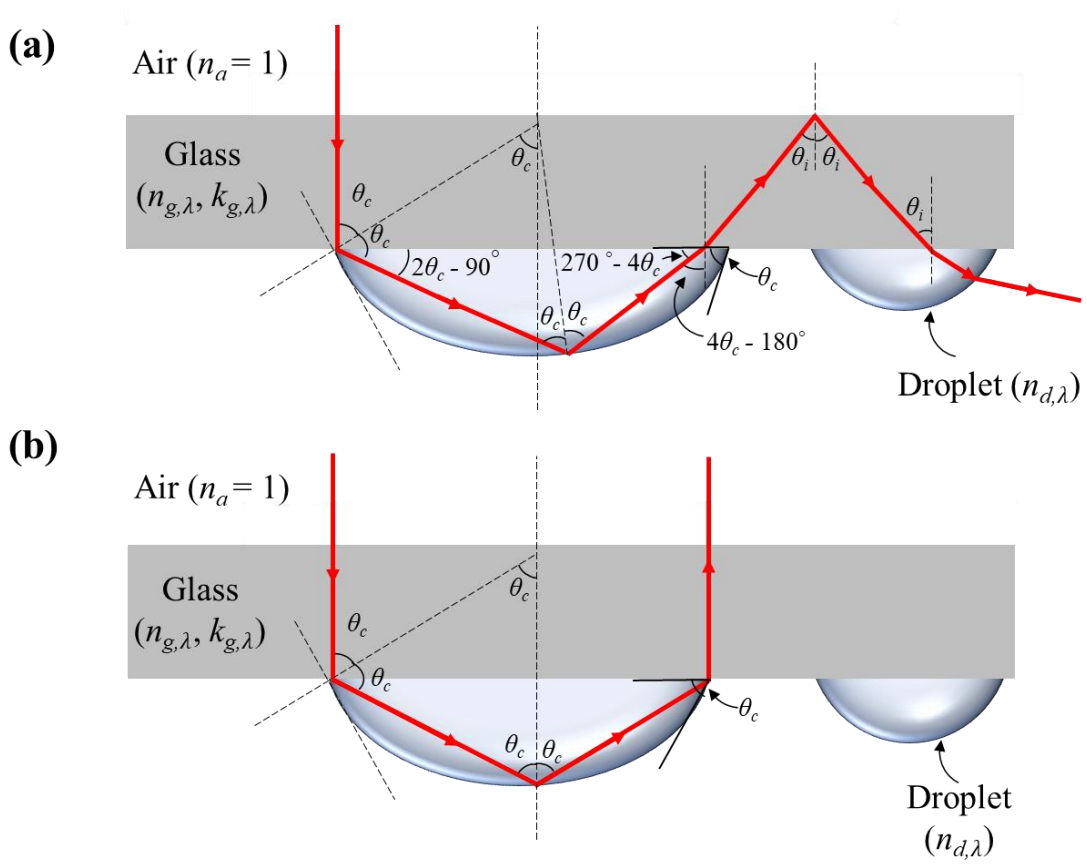

Figure A.8. Schematic of a glass having pendant droplets on their backside with droplet contact angle (a) 55°< θ_c < 60° and (b) θ_c = 60°.

Further simulations were performed to investigate the effect of the glass and droplet refractive index on the starting contact angle for the constant normal-hemispherical transmittance and reflectance. Figure A.9 shows the normal-hemispherical transmittance T_{nh} of droplet-covered glass as a function of contact angle θ_c between 50° and 65°for non-absorbing droplet-covered glass slabs with (i) n_g= 1.61 and n_d = 1.49, (ii) n_g = 1.61 and n_d = 1.33, and (iii) n_g = 1.50 and n_d = 1.33 with surface area coverage f_A = 45%. Figure A.9 indicates that for glass slabs with n_g = 1.61 and n_d = 1.49, the normal-hemispherical transmittance T_{nh} remained constant for contact angles 55.5° ≤ θ_c < 60°, as also observed experimentally.

However, for glass slabs with n_g = 1.61 and n_d = 1.33, and n_g = 1.50 and n_d = 1.33, the normal-hemispherical transmittance T_{nh} remained constant for contact angles 57.2° ≤ θ_c < 60°. Figure A.9 indicates that the starting contact angle for the constant normal-hemispherical transmittance and reflectance was independent of the refractive index of the glass n_g and depended on the refractive index of the droplet n_d.

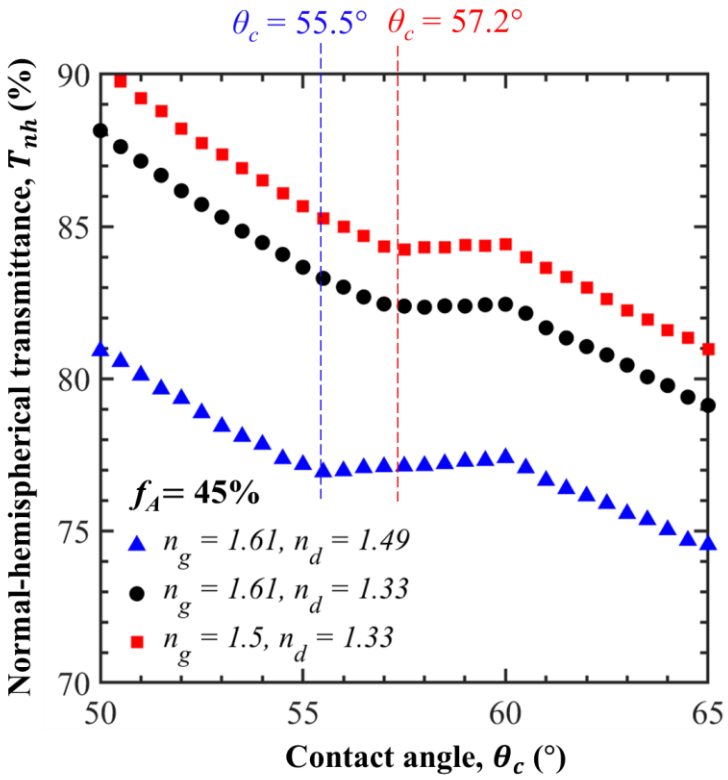

Figure A.9. Normal-hemispherical transmittance T_{nh} as a function of droplet contact angle θ_c for droplet-covered samples with n_g = 1.61 or 1.5, n_d = 1.49 or 1.33, and f_A = 45%.

APPENDIX B: Supplementary Materials for Chapter 3

B.1 Optical properties of soda-lime silica glass window and water

Figure B.1 plots the spectral refractive n_λ and absorption k_λ indices of soda-lime silica glass and water between 0.3 and 50 μm taken from Refs.[80,98], respectively.

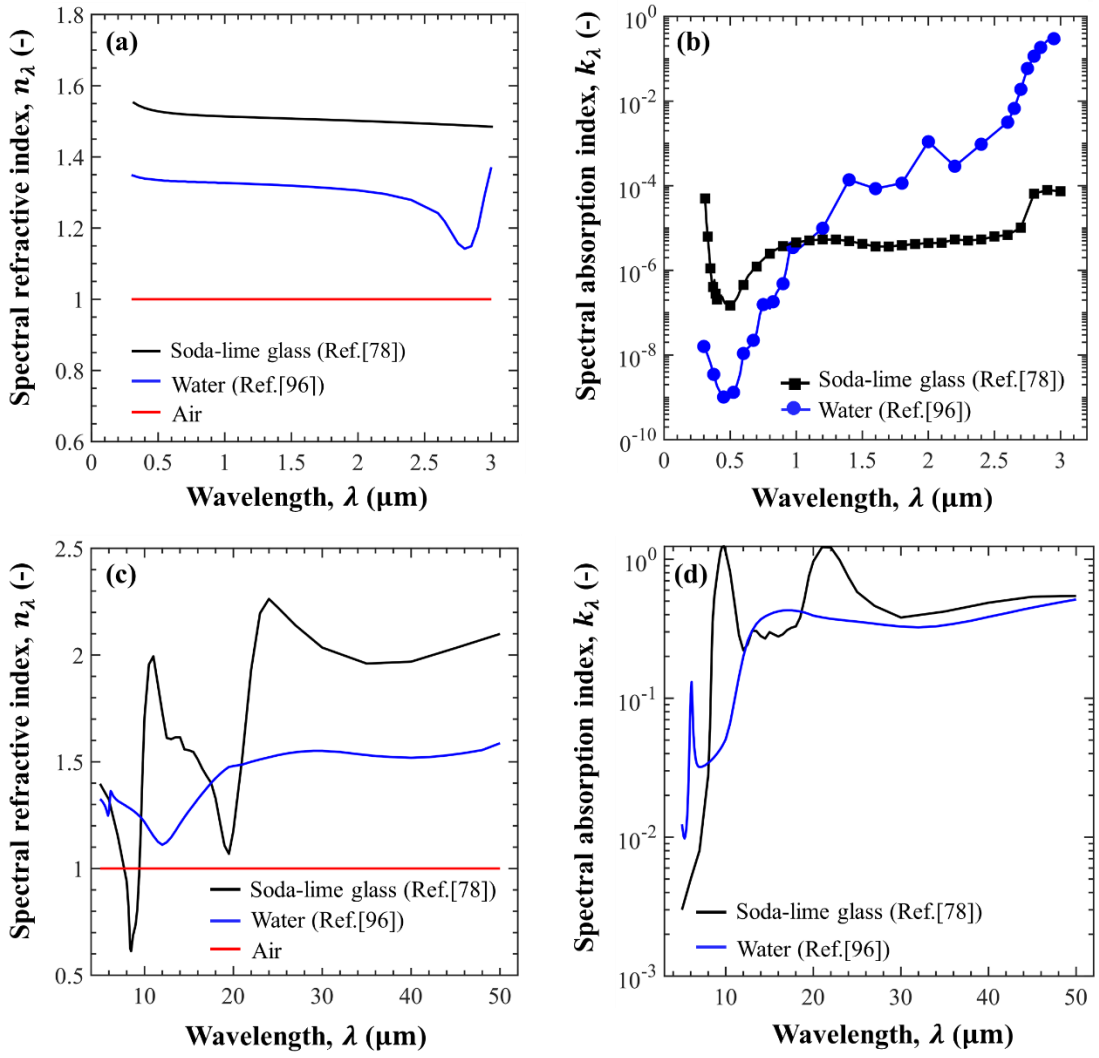

Figure B.1. Spectral refractive n_λ and absorption indices k_λ of the glass and water taken from Refs.[80] and [98], respectively for λ between (a, b) 0.3 and 3 μm and (c, d) 5 and 50 μm

B.2 Spectral directional-hemispherical transmittance

Figure B.2 plots the predicted directional-hemispherical transmittance $T_{dh,\lambda}$ between 0.3 and 3 μm for the glass window supporting water droplets on its (a, b, c) back side or (d, e, f) front side with droplet contact angle θ_c = 30°, 60°, and 90°, and surface area coverage f_A = 59% on June 21st in Los Angeles between 8 AM and 5 PM.

For back side condensation, the directional-hemispherical transmittance $T_{dh,\lambda}$ decreased with increasing droplet contact angle θ_c at all wavelengths and times considered. This was caused by increased reflection by the droplets at wavelengths $\lambda \leq 1.2$ μm when the absorption index $k_{d,\lambda}$ of water was small, as shown in Figure B.1.

However, for front side condensation, $T_{dh,\lambda}$ was independent of contact angle θ_c at t = 11 AM and 2 PM for wavelengths $\lambda \leq 1.2$ μm due to the small values of $k_{d,\lambda}$ and the near-normal solar zenith angles ($\theta_z \leq 30°$). For $\lambda > 1.2$ μm, $T_{dh,\lambda}$ of the glass window supporting water droplets on its either back or front side decreased with increasing θ_c due to the fact that the volume of the droplets increased and that water was strongly absorbing in this spectral window, as shown in Figure B.1. The transmittance $T_{dh,\lambda}$ reached a local minimum at λ = 2 μm due to the peak in the water absorption index $k_{d,\lambda}$ for both back and front side configurations at all times considered. In addition, $T_{dh,\lambda}$ was minimum at t = 8 AM and reached a maximum at t = 2 PM as the solar zenith angle θ_z decreased from 64° to 18°.

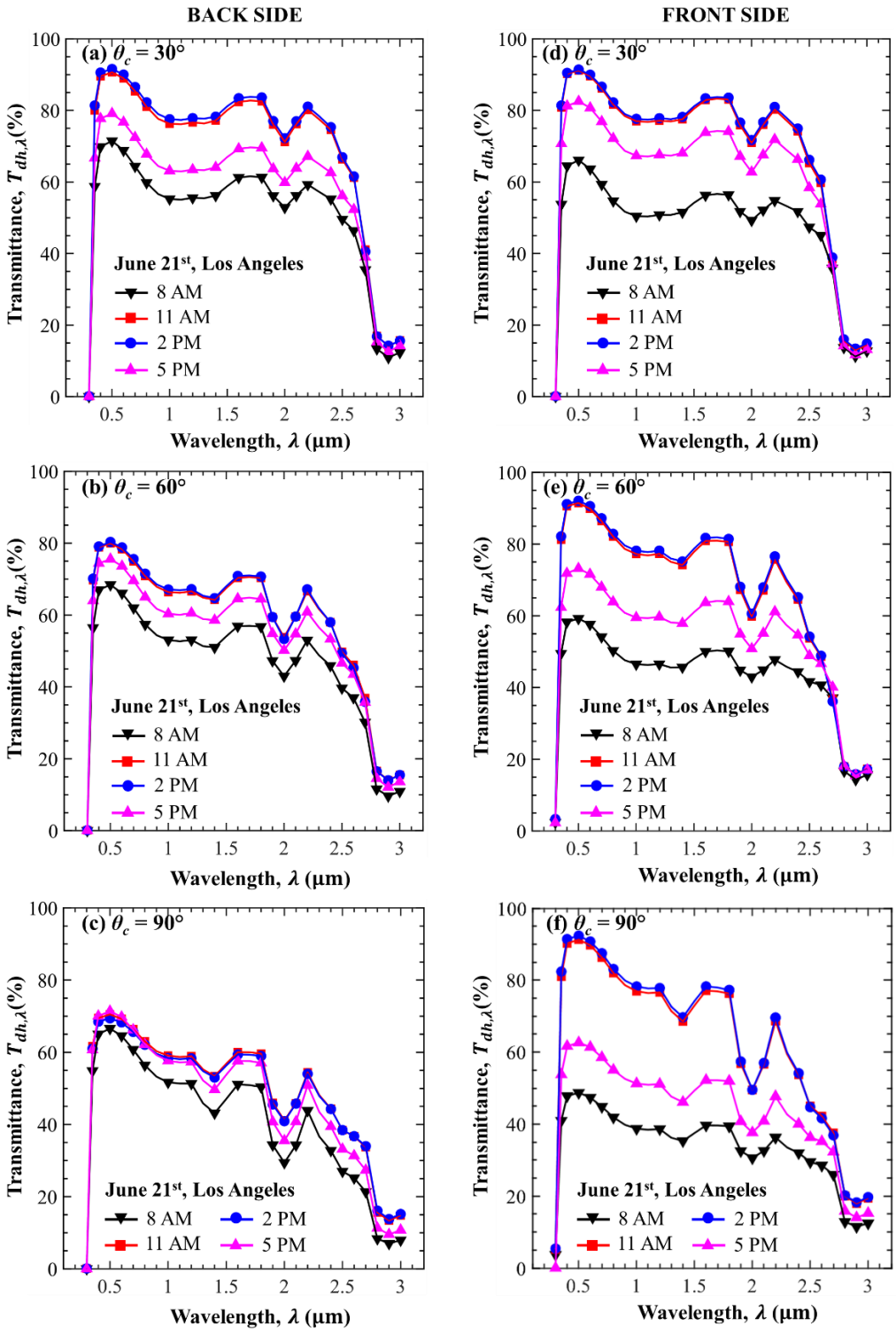

Figure B.2. Directional-hemispherical transmittance $T_{dh,\lambda}$ as a function of wavelength λ for glass window with water droplets on its (a, b, c) back and (d, e, f) front side for droplet contact angle θ_c = 30°, 60°, and 90°, and surface area coverage f_A = 59% on June 21st, in Los Angeles, CA.

B.3 Truncation approach for total hemispherical emissivity calculation

Table B.1 shows the total hemispherical emissivity of the soda-lime glass calculated for different upper integration limits of Equation (5.6) by using reported refractive and absorption indices of the soda-lime silica glass [80].

Table B.1. The total hemispherical emissivity of soda-lime glass calculated for different upper integration limits.

Lower integration limit (μm)	**Upper integration limit (μm)**	**Total hemispherical emissivity, ε**
5	50	0.8956
5	100	0.8940
5	200	0.8937
5	300	0.8937

B.4 Reflectance and total hemispherical emissivity

Figure B.3 plots $R_{nh,\lambda}$ for the dry and glass windows with water droplets on their (a) back and (b) front side with θ_c = 30°, 60°, and 90° and f_A = 59% and (c) ε as a function θ_c with f_A = 59%.

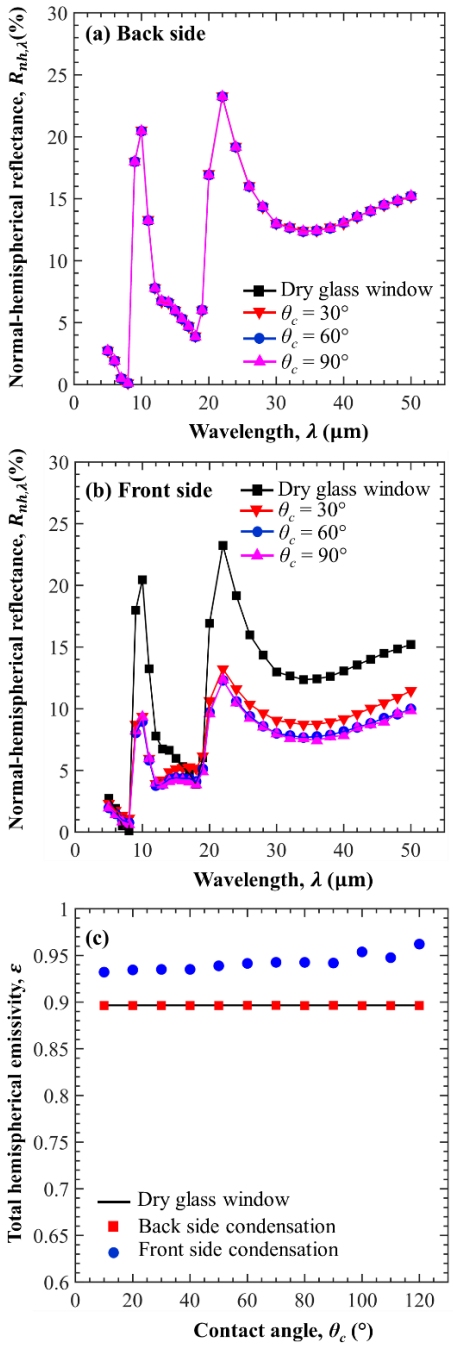

Figure B.3. Reflectance $R_{nh,\lambda}$ for the glass windows supporting water droplets on their (a) back and (b) front for θ_c = 30°, 60°, and 90° and (c) emissivity ε as a function of θ_c. Here, f_A = 59%.

APPENDIX C: Supplementary Materials for Chapter 4

C.1 Silica nanoparticle synthesis

For the silica nanoparticle synthesis, tetraethyl orthosilicate (TEOS, 97.0+%, TCI America^{TM}), ethanol (EtOH, 200 proof, Rossville Gold Shield), ammonium hydroxide (NH_4OH, VWR Chemicals BDH), and deionized (DI) water were used without any further purification. EtOH (8 mL), NH_4OH (0.31 mL), and DI water (1.4 mL) were mixed under vigorous magnetic stirring under atmospheric conditions. After 2 minutes of stirring, TEOS (1.5 mL) was added in a single step. The solution was left to stir for 24 hours to allow for the complete growth of nanoparticles.

C.2 Effect of droplet refractive index on the transmittance

Figure C.1 plots the directional-hemispherical transmittance as a function of incident angle θ_i for windows supporting droplets on their frontside with refractive index n_d = 1.33 or 1.5, contact angle θ_c = 90°, and surface area coverage f_A = 50% [64]. The results indicate that the directional-hemispherical transmittance features the same trends and similar magnitude for both values of n_d considered.

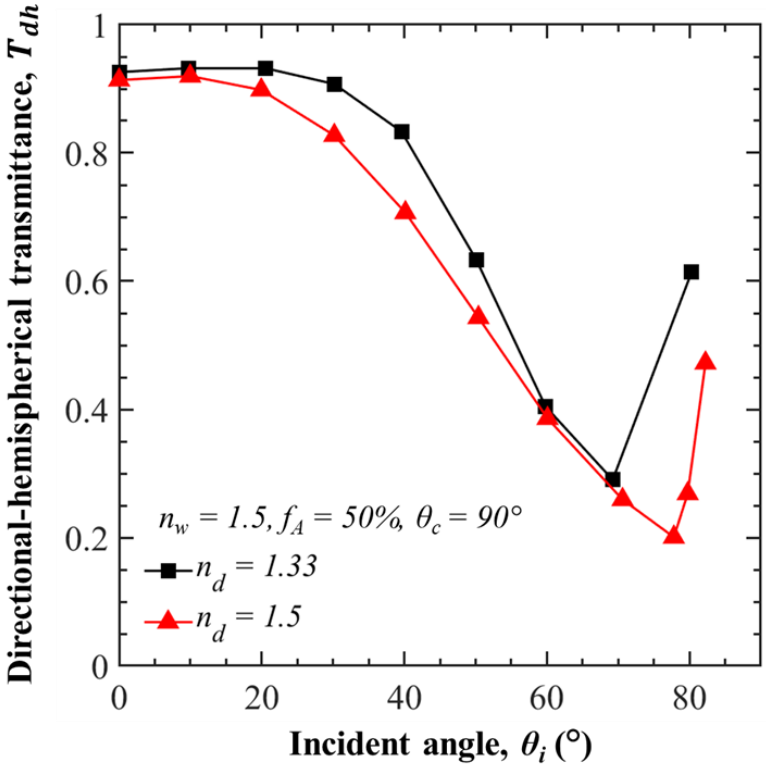

Figure C.1. Comparison of the directional-hemispherical transmittance T_{dh} of droplet-covered windows as a function of incident angle θ_i for droplet refractive index n_d = 1.33 or 1.5, as reported in Ref.[64]. In both cases, the droplet contact angle was θ_c = 90°, the surface area coverage was f_A = 50%, and the window refractive index was n_w = 1.5.

C.3 *i-V* curve

Figure C.2 shows the *i-V* curve for the bare solar cell at incident angle θ_i = 0° and irradiation G_s = 1 kW/m^2 at different times during the experiment. Figure C.2 indicates that the solar irradiation supplied by the solar simulator did not fluctuate during the experiments.

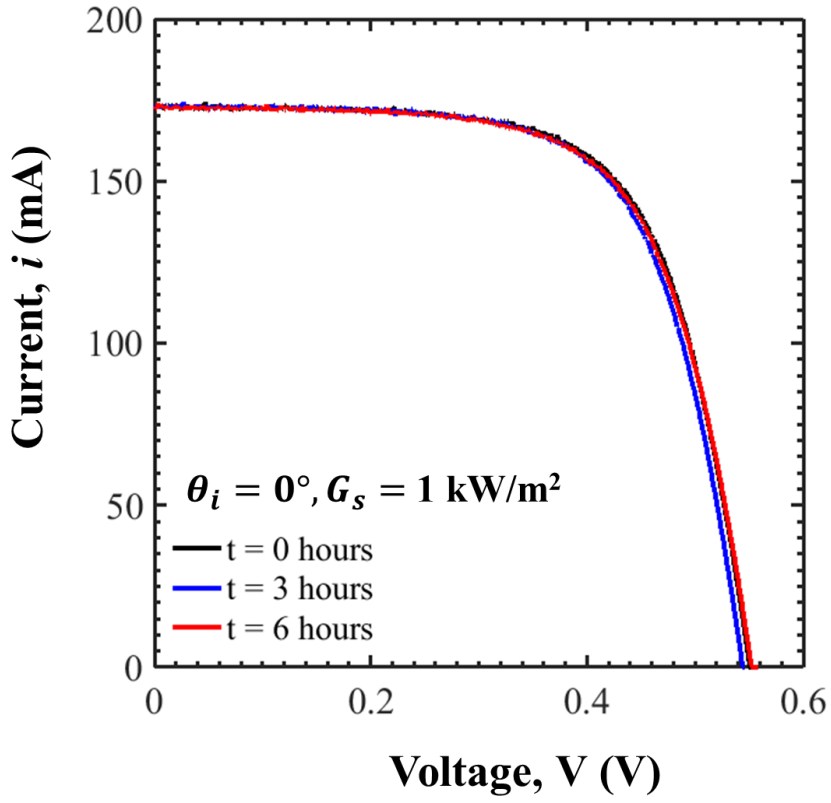

Figure C.2. *i-V* for the bare solar cell at incident angle θ_i = 0° and irradiation G_s = 1 kW/m^2 at different times during the experiments.

C.4 *i-V* curve of solar cell with glass cover supporting droplets

In order to demonstrate the impact of water droplets on the performance of solar cells, the glass cover was placed on top of the bare solar cell and water droplets were sprayed on it using a push spray bottle. The contact angle of water droplets on the glass cover was measured using a Drop Shape Analyzer (DSA100, Kruss Scientific, Germany). The contact angle measurements were repeated for 7 different droplets. The mean contact angle of water droplets on the clean glass cover was $\bar{\theta}_c = 33.2° \pm 5.3°$. For each value of incident angle θ_i, all droplets were wiped out, new water droplets were sprayed on the solar cell glass cover, and the current vs. voltage curves (*i-V* curves) were collected over a duration of 5 minutes. Figure C.3 compares the *i-V* curves obtained from (i) a bare solar cell, (ii) a solar cell with a dry glass cover, (iii) a solar cell with glass covers supporting acrylic droplets with mean contact angle $\bar{\theta}_c = 25.8°$ and surface area coverage $f_A = 45\%$, and (iv) a solar cell with glass covers supporting water droplets with mean contact angle $\bar{\theta}_c = 33.2°$ for (a) incident angle $\theta_i = 0°$ and irradiation $G_s = 1$ kW/m^2, (b) $\theta_i = 30°$ and $G_s = 0.86$ kW/m^2, (c) $\theta_i = 50°$ and $G_s = 0.64$ kW/m^2, and (d) $\theta_i = 70°$ and $G_s = 0.34$ kW/m^2. Figures C.3(a) and C.3(b) indicate that the presence of water and acrylic droplets did not affect the *i-V* curve of the solar cells for $\theta_i \leq 30°$. However, Figures C.3(c) and C.3(d) show that the generated current *i* decreased for both acrylic and water droplets for incident angles $\theta_i = 50°$ and 70°. The current *i* generated by the solar cell covered with water droplets was smaller than that covered with acrylic droplets. This may be attributed to the larger surface area coverage f_A and/or droplet contact angle θ_c of the water droplets. Furthermore, Figure C.3(d) indicates that, for the solar cell with water droplets, the generated current *i* increased at low voltages due to the decreases in surface area coverage f_A as the droplet evaporated. The surface area coverage f_A of the water droplets decreased during the course of the experiments due to droplet evaporation, merger, and/or roll-off from the glass surface.

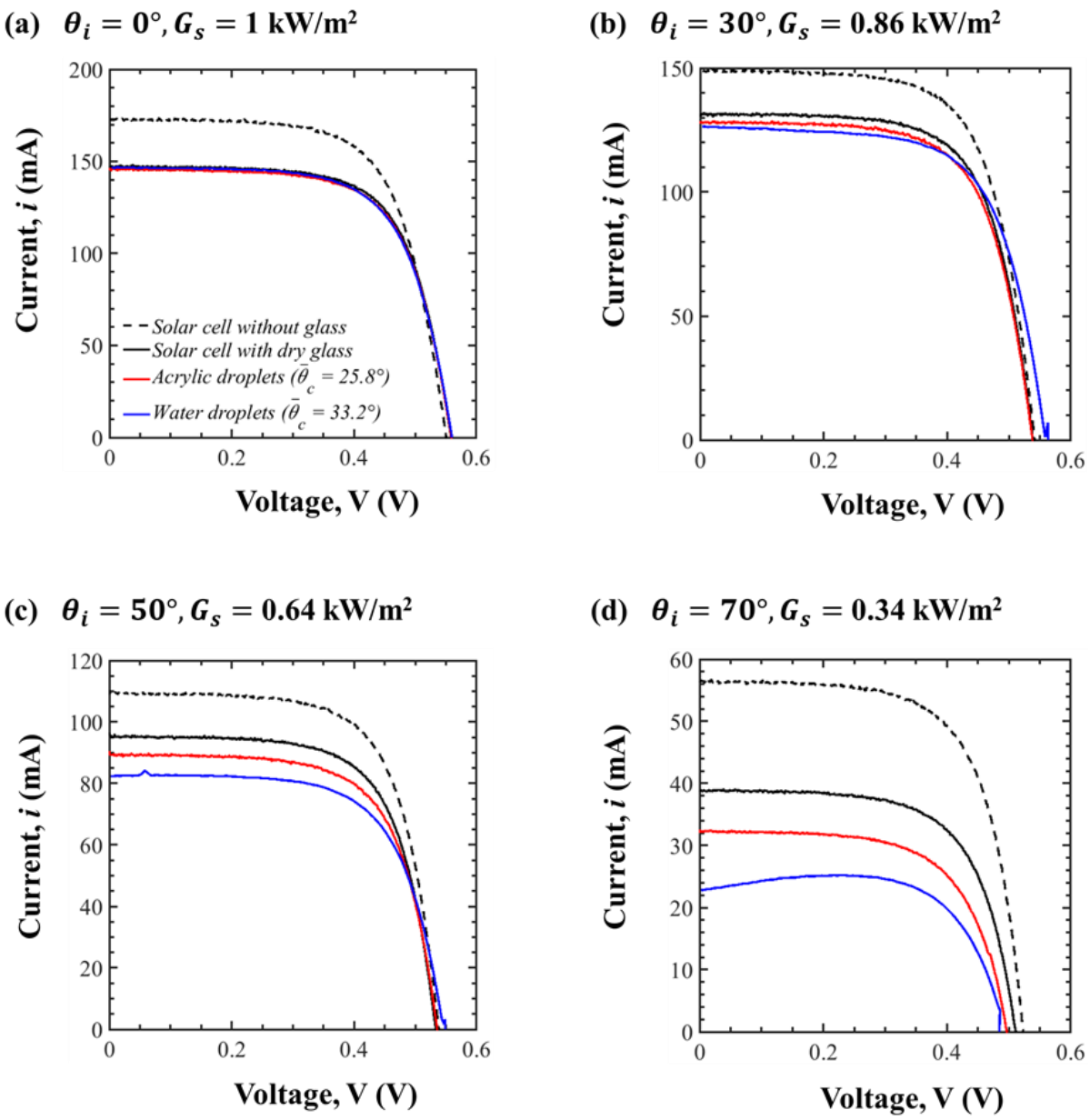

Figure C.3. Current i as a function of voltage V for (a) incident angle θ_i = 0° and irradiation G_s = 1 kW/m^2, (b) θ_i = 30° and G_s = 0.86 kW/m^2, (c) θ_i = 50° and G_s = 0.64 kW/m^2, and (d) θ_i = 70° and G_s = 0.34 kW/m^2.

C.5 The reflectivity of the glass/solar cell interface

Figure C.4 shows reflectivity R_{gc} of the glass/solar cell interface as a function of incident angle θ_i ranging between 0 and 85°. Figure C.4 indicates that reflectivity R_{gc} of the glass/solar cell interface remained nearly constant around 19%.

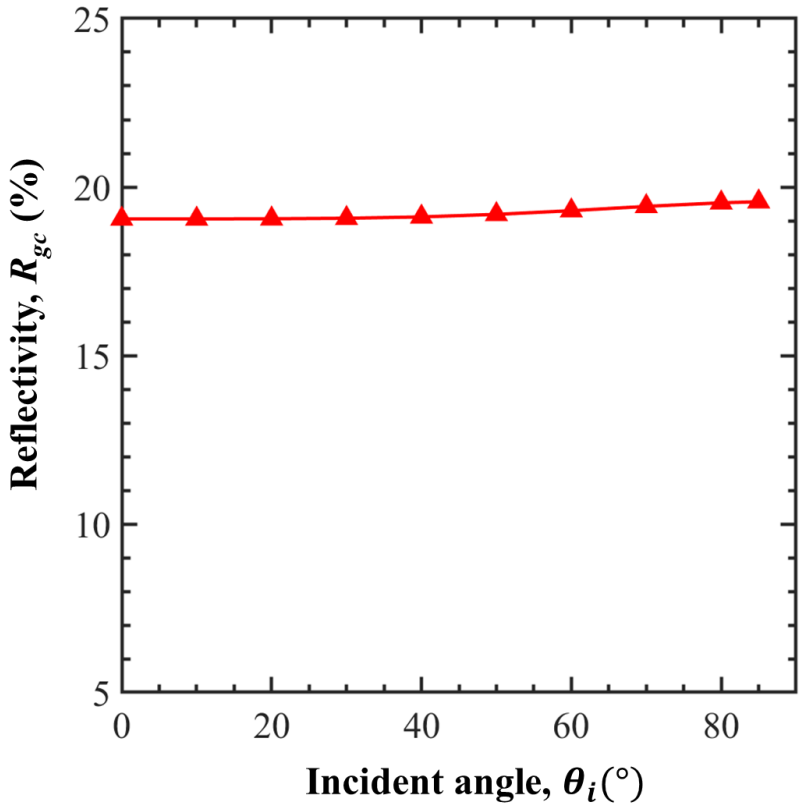

Figure C.4. Reflectivity of the glass/solar cell R_{gc} interface as a function incident angle θ_i.

APPENDIX D: Supplementary Materials for Chapter 5

D.1 Droplet contact angle on radiative cooling surfaces

Figure D.1 shows the contact angle of the acrylic droplets on the radiative cooling surfaces.

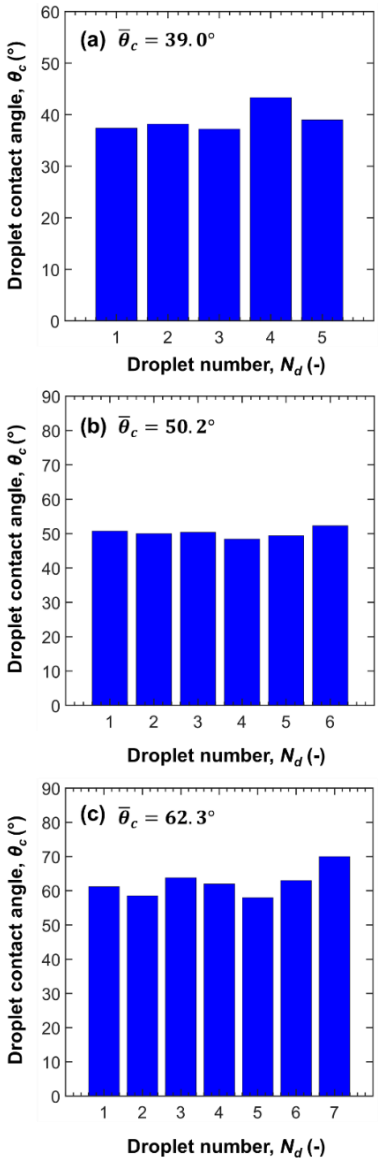

Figure D.1 Droplet contact angle θ_c measurements of the (a) uncoated sample and samples coated with (b) NeverWet and (c) perfluorinated silane.

D.2 Reflectance measurements of radiative cooling surfaces

Figure D.2 plots the reflectance $R_{nh,\lambda}$ of the dry and droplet-covered samples (a) without coating, (b) with NeverWet™, and (c) silane coating with $\bar{\theta}_c$ = 39°, 50.2°, and 62.3°, respectively.

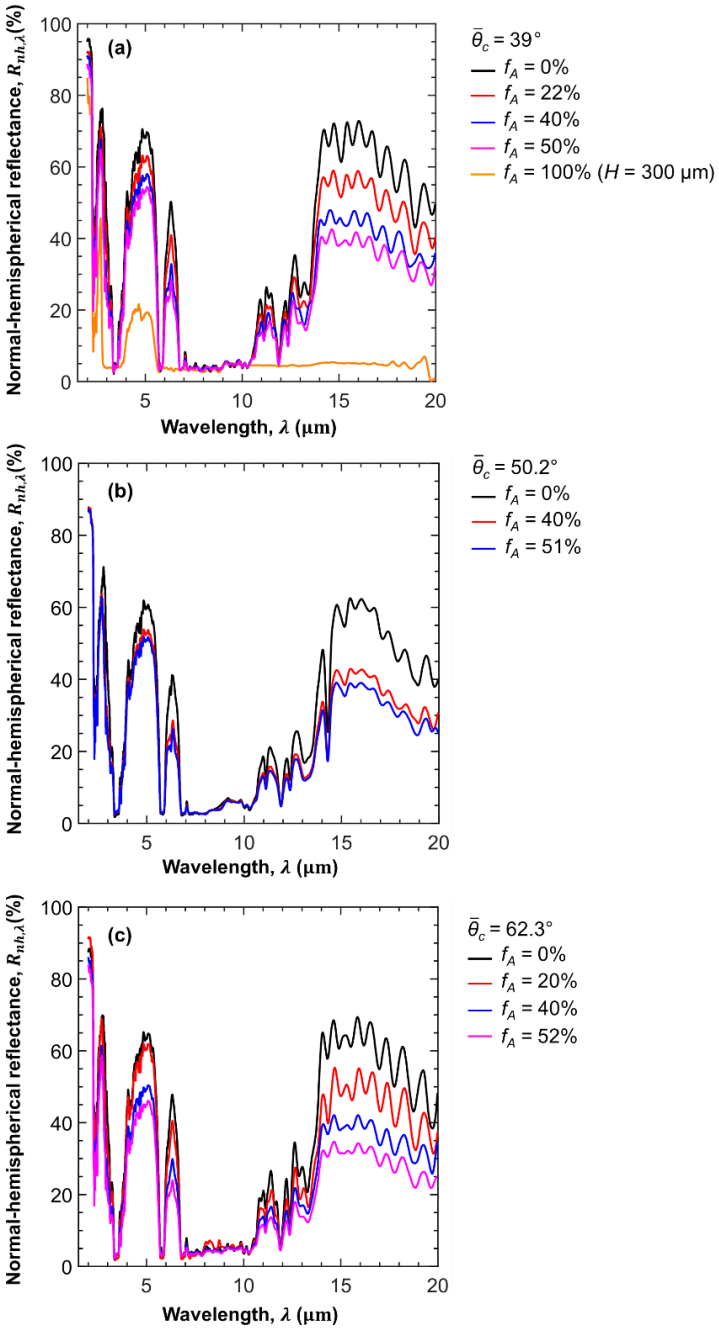

Figure D.2. Spectral normal-hemispherical reflectance $R_{nh,\lambda}$ for dry and droplet-covered samples (a) without coating, coated with (b) NeverWet™, and (c) silane with $\bar{\theta}_c$ = 39°, 50.2°, and 62.3°.

D.3 Spectral directional emittance of radiative cooling surfaces

Figure D.3 plots the spectral directional emittance $\varepsilon_{d,\lambda}$ between 2 and 20 μm for the droplet-covered samples with (a) droplet mean contact angle $\bar{\theta}_c$ = 39° (Sample 5) and (b) $\bar{\theta}_c$ = 62.3° (Sample 10B) and surface area coverage $f_A \approx 51 \pm 1\%$ at incident angles θ_i = 0°, 20°, 40°, and 60°.

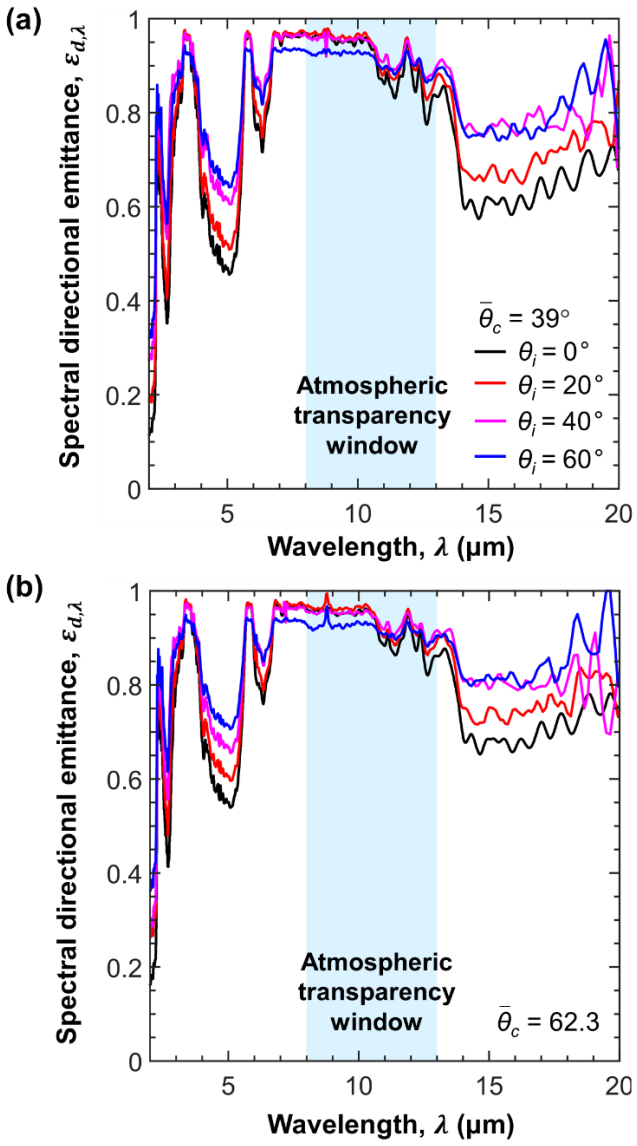

Figure D.3. Spectral directional emittance $\varepsilon_{d,\lambda}$ for dry and droplet-covered samples with contact angle (a) $\bar{\theta}_c$ = 39° (Sample 5) and (b) $\bar{\theta}_c$= 62.3° (Sample 10B) with surface area coverage $f_A \approx 51 \pm 1\%$ for incident angles θ_i = 0°, 20°, 45°, and 60°.

Bibliography

[1] M. N. Nieuwoudt and E. H. Mathews, “A mobile solar water heater for rural housing in Southern Africa,” *Building and Environment*, vol. 40, pp. 1217–1234, 2005.

[2] J. Oshikiri and T. N. Anderson, “Condensation Control in Glazed Flat Plate Solar Water Heaters,” in *Proceedings of the 23rd International Symposium on Transport Phenomena*, Auckland, New Zealand, November 19–22, 2013.

[3] H. H. Al-Kayeim, M. A. Aurybi, and S. I. U. Gilani, “Influence of canopy condensate film on the performance of solar chimney power plant,” *Renewable Energy*, vol. 136, pp. 1012–1021, 2019.

[4] J. G. Pieters, J. M. J. J. Deltour, and M. J. G. Debruyckere, “Onset of condensation on the inner and outer surface of greenhouse covers during night,” *Journal of Agricultural and Engineering Research*, vol. 61, pp. 165–171, 1994.

[5] G. Papadakis, D. Briassoulis, G. Scarascia Mugnozza, G. Vox, P. Feuilloley, and J. A. Stoffers, “Radiometric and thermal properties of, and testing methods for, greenhouse covering materials,” *Journal of Agricultural and Engineering Research*, vol. 77. pp. 7–38, 2000.

[6] F. Geoola, Y. Kashti, A. Levi, and R. Brickman, “Quality evaluation of anti-drop properties of greenhouse cladding materials,” *Polymer Testing*, vol. 23, no. 7, pp. 755–761, 2004.

[7] I. V. Pollet and J. G. Pieters, “Condensation and Radiation Transmittance of Greenhouse Cladding Materials, Part 2: Results for a Complete Condensation Cycle,” *Journal of Agricultural and Engineering Research*, vol. 75, pp. 65–72, 2000.

[8] I. V. Pollet and J. G. Pieters, “Condensation and Radiation Transmittance of Greenhouse Cladding Materials: Part 1, Laboratory Measuring Unit and Performance,” *Journal of Agricultural and Engineering Research*, vol. 74, pp. 369–377, 1999.

[9] I. V. Pollet and J. G. Pieters, “Condensation and radiation transmittance of greenhouse cladding materials, Part 3: Results for glass plates and plastic films,” *Journal of Agricultural and Engineering Research*, vol. 77, no. 4, pp. 419–428, 2000.

[10] National Research Council, *Sustainable Development of Algal Biofuels in the United States*. National Academies Press, Washington, DC, 2012.

[11] B. K. Behera and A. Varma, *Microbial Resources for Sustainable Energy*. Springer International Publishing, Cham, Switzerland, 2016.

[12] K. H. Mangi, Z. Larbi, J. Legrand, J. Pruvost, and E. K. Si-Ahmed, “Passive thermal regulation approach for Algofilm© photobioreactor through phase change,” *Chemical Engineering Research and Design*, vol. 168, pp. 411–425, 2021.

[13] J. Hoeniges, K. Zhu, J. Pruvost, J. Legrand, E. Si-Ahmed, and L. Pilon, “Impact of Dropwise Condensation on the Biomass Production Rate in Covered Raceway Ponds,” *Energies*, vol. 14, no. 2, 268, 2021.

[14] R. El Dlasty and I. Budaiwi, “External Condensation on Windows,” *Construction & Building Materials*, vol. 3, no. 2, pp. 135–139, 1989.

[15] A. Werner and A. Roos, “Condensation tests on glass samples for energy efficient windows,” *Solar Energy Materials and Solar Cells*, vol. 91, pp. 609–615, 2007.

[16] A. Werner and A. Roos, “Simulations of coatings to avoid external condensation on low U-value windows,” *Optical Materials*, vol. 30, no. 6. pp. 968–978, 2008.

[17] A. Laukkarinen, P. Kero, and J. Vinha, “Condensation at the exterior surface of windows,” *Journal of Building Engineering*, vol. 19, pp. 592–601, 2018.

[18] L. Zuo, Y. Zheng, Z. Li, and Y. Sha, “Experimental investigation on the effect of cover material on the performance of solar still,” in *Proceedings of International Conference on Sustainable Power Generation and Supply (SUPERGEN)*, Hangzhou, China, September 8–9, 2012.

[19] P. Zanganeh, A. S. Goharrizi, S. Ayatollahi, and M. Feilizadeh, “Productivity enhancement of solar stills by nano-coating of condensing surface,” *Desalination*, vol. 454, pp. 1–9, 2019.

[20] P. Zanganeh, A. S. Goharrizi, S. Ayatollahi, and M. Feilizadeh, “Nano-coated condensation surfaces enhanced the productivity of the single-slope solar still by changing the condensation mechanism,” *Journal of Cleaner Production*, vol. 265, 121758, 2020.

[21] K. V. Modi and K. H. Nayi, “Efficacy of forced condensation and forced evaporation with thermal energy storage material on square pyramid solar still,” *Renewable Energy*, vol. 153, pp. 1307–1319, 2020.

[22] R. Bhardwaj, M. V. ten Kortenaar, and R. F. Mudde, “Influence of condensation surface on solar distillation,” *Desalination*, vol. 326, pp. 37–45, 2013.

[23] G. Ni, S. H. Zandavi, S. M. Javid, S. v. Boriskina, T. A. Cooper, and G. Chen, “A salt-rejecting floating solar still for low-cost desalination,” *Energy and Environmental Science*, vol. 11, pp. 1510–1519, 2018.

[24] T. Kita, Y. Harada, and S. Asahi, *Energy Conversion Efficiency of Solar Cells*. Springer Singapore, Singapore, 2019.

[25] International Energy Agency (IEA), “World Energy Outlook.” https://www.iea.org/reports/world-energy-outlook-2019 (accessed Nov. 14, 2021).

[26] National Renewable Energy Laboratory, “Best Research-Cell Efficiency Chart.” https://www.nrel.gov/pv/cell-efficiency.html (accessed Nov. 14, 2021).

[27] K. Ilse, B. Figgis, M. Z. Khan, V. Naumann, and C. Hagendorf, “Dew as a Detrimental Influencing Factor for Soiling of PV Modules,” *IEEE Journal of Photovoltaics*, vol. 9, no. 1, pp. 287–294, 2019.

[28] C. Del Pero, N. Aste, and F. Leonforte, “The effect of rain on photovoltaic systems,” *Renewable Energy*, vol. 179, pp. 1803–1814, 2021.

[29] S. A. Hosseini, A. M. Kermani, and A. Arabhosseini, “Experimental study of the dew formation effect on the performance of photovoltaic modules,” *Renewable Energy*, vol. 130, pp. 352–359, 2019.

[30] F. Trombe, “Perspectives sur l’utilisation des rayonnements solaires et terrestres dans certaines régions du monde,” *Revue Générale Thermique*, vol. 6, pp. 1285–1314, 1967.

[31] X. Sun, Y. Sun, Z. Zhou, M. A. Alam, and P. Bermel, “Radiative sky cooling: Fundamental physics, materials, structures, and applications,” *Nanophotonics*, vol. 6, no. 5, pp. 997–1015, 2017.

[32] M. Santamouris and J. Feng, “Recent progress in daytime radiative cooling: Is it the air conditioner of the future?,” *Buildings*, vol. 8, no. 12, 168, 2018.

[33] T. L. Bergman, “Active daytime radiative cooling using spectrally selective surfaces for air conditioning and refrigeration systems,” *Solar Energy*, vol. 174, pp. 16–23, 2018.

[34] J. N. Munday, “Tackling climate change through radiative cooling,” *Joule*, vol. 3, pp. 2057–2060, 2019.

[35] X. Lu, P. Xu, H. Wang, T. Yang, and J. Hou, “Cooling potential and applications prospects of passive radiative cooling in buildings: The current state-of-the-art,” *Renewable and Sustainable Energy Reviews*, vol. 65, pp. 1079–1097, 2016.

[36] A. Baniassadi, D. J. Sailor, and G. A. Ban-Weiss, “Potential energy and climate benefits of super-cool materials as a rooftop strategy,” *Urban Climate*, vol. 29, 100495, 2019.

[37] J. Mandal, Y. Yang, N. Yu, and A. P. Raman, “Paints as a scalable and effective radiative cooling technology for buildings,” *Joule*, vol. 4, pp. 1350–1356, 2020.

[38] N. Agam and P. R. Berliner, “Dew formation and water vapor adsorption in semi-arid environments - A review,” *Journal of Arid Environments*, vol. 65, pp. 572–590, 2006.

[39] K. K. Ilse, B. W. Figgis, V. Naumann, C. Hagendorf, and J. Bagdahn, “Fundamentals of soiling processes on photovoltaic modules,” *Renewable and Sustainable Energy Reviews*, vol. 98, pp. 239–254, 2018.

[40] G. Yang, D. Chai, Z. Fan, and X. Li, “Capillary condensation of single and multicomponent fluids in nanopores,” *Industrial and Engineering Chemistry Research*, vol. 58, no. 41, pp. 19302–19315, 2019.

[41] L. Chen, R. Meissner, Y. Zhang, and H. Xiao, “Studies on dew formation and its meteorological factors,” *Agriculture & Environment*, vol. 11, pp. 1063–1068, 2013.

[42] K. Richards, “Observation and simulation of dew in rural and urban environments,” *Progress in Physical Geography*, vol. 28, pp. 76–94, 2004.

[43] O. Uclés, L. Villagarcía, M. J. Moro, Y. Canton, and F. Domingo, “Role of dewfall in the water balance of a semiarid coastal steppe ecosystem,” *Hydrological Processes*, vol. 28, no. 4, pp. 2271–2280, 2014.

[44] F. Ritter, M. Berkelhammer, and D. Beysens, “Dew frequency across the US from a network of in situ radiometers,” *Hydrology and Earth System Sciences*, vol. 23, no. 2, pp. 1179–1197, 2019.

[45] X. Guo, T. Zha, X. Jia, B. Wu, W. Feng, J. Xie, J. Gong, Y. Zhang, and H. Peltola., “Dynamics of dew in a cold desert-shrub ecosystem and its abiotic controls,” *Atmosphere*, vol. 7, no. 3, 2016.

[46] T. L. Bergman, A. S. Lavine, F. P. Incropera, and D. P. Dewitt, *Fundamentals of Heat and Mass Transfer*, John Wiley & Sons, Hoboken, NJ, 7th edition, 2011.

[47] A. K. Kota, G. Kwon, and A. Tuteja, “The design and applications of superomniphobic surfaces,” *NPG Asia Materials*, vol. 6, 109, 2014.

[48] J. T. Simpson, S. R. Hunter, and T. Aytug, “Superhydrophobic materials and coatings: A review,” *Reports on Progress in Physics*, vol. 78, 086501, 2015.

[49] G. Wu, Y. Yang, Y. Lei, D. Fu, Y. Li, Y. Zhan, J. Zhen, M. Teng, “Hydrophilic nano-SiO_2/PVA-based coating with durable antifogging properties,” *Journal of Coatings Technology and Research*, vol. 17, pp. 1145–1155, 2020.

[50] D. Ahmad, I. van den Boogaert, J. Miller, R. Presswell, and H. Jouhara, “Hydrophilic and hydrophobic materials and their applications,” *Energy Sources, Part A: Recovery, Utilization and Environmental Effects*, vol. 40, no. 22, pp. 2686–2725, 2018.

[51] J. B. Boreyko and C. H. Chen, “Self-propelled dropwise condensate on superhydrophobic surfaces,” *Physical Review Letters*, vol. 103, 184501, 2009.

[52] B. J. Briscoe and K. P. Galvin, “The effect of surface fog on the transmittance of light,” *Solar Energy*, vol. 46, no. 4, pp. 191–197, 1991.

[53] R. Wen, S. Xu, D. Zhao, Y. C. Lee, X. Ma, and R. Yang, “Hierarchical superhydrophobic surfaces with micropatterned nanowire arrays for high-efficiency jumping droplet condensation,” *ACS Applied Materials and Interfaces*, vol. 9, no. 51, pp. 44911–44921, 2017.

[54] R. Wen, S. Xu, X. Ma, Y. C. Lee, and R. Yang, “Three-dimensional superhydrophobic nanowire networks for enhancing condensation heat transfer,” *Joule*, vol. 2, no. 2, pp. 269–279, 2018.

[55] K. Zhu, Y. Huang, J. Pruvost, J. Legrand, and L. Pilon, “Transmittance of transparent windows with non-absorbing cap-shaped droplets condensed on their backside,” *Journal of Quantitative Spectroscopy and Radiative Transfer*, vol. 194, pp. 98–107, 2017.

[56] J. Hoeniges, K. Zhu, W. Welch, E. Simsek, and L. Pilon, “Transmittance of transparent horizontal and tilted windows supporting large non-absorbing pendant droplets,” *Journal of Quantitative Spectroscopy and Radiative Transfer*, vol. 275, 107876, 2021.

[57] I. V. Pollet and J. G. Pieters, “Laboratory measurements of PAR transmittance of wet and dry greenhouse cladding materials,” *Agricultural and Forest Meteorology*, vol. 93, no. 2, pp. 149–152, 1999.

[58] M. S. Ahamed, H. Guo, and K. Tanino, “Energy saving techniques for reducing the heating cost of conventional greenhouses,” *Biosystems Engineering*, vol. 178, pp. 9–33, 2019.

[59] B. Cemek and Y. Demir, “Testing of the condensation characteristics and light transmissions of different plastic film covering materials,” *Polymer Testing*, vol. 24, no. 3, pp. 284–289, 2005.

[60] C. Stanghellini, M. Bruins, V. Mohammadkhani, G. J. Swinkels, and P. J. Sonneveld, "Effect of Condensation on Light Transmission and Energy Budget of Seven Greenhouse Cover Materials," *Acta Horticulturae*, vol. 952, pp. 249–254, 2012.

[61] F. Geoola, Y. Kashti, and U. M. Peiper, "Solar radiation transmissivity of greenhouse cladding materials," *Acta Horticulturae*, vol. 534, pp. 109–116, 2000.

[62] E. Simsek, M. J. Williams, and L. Pilon, "Effect of dew and rain on photovoltaic solar cell performances," *Solar Energy Materials and Solar Cells*, vol. 222, 110908, 2021.

[63] Y. Huang, C. Feng, J. Hoeniges, K. Zhu, and L. Pilon, "Bidirectional transmittance of transparent windows with external or backside condensation of nonabsorbing cap-shaped droplets," *Journal of Quantitative Spectroscopy and Radiative Transfer*, vol. 251, 107039, 2020.

[64] K. Zhu, S. Li, and L. Pilon, "Light transfer through windows with external condensation," *Journal of Quantitative Spectroscopy and Radiative Transfer*, vol. 208, pp. 164–171, 2018.

[65] C. K. Hsieh and A. K. Rajvanshi, "The effect of dropwise condensation on glass solar properties," *Solar Energy*, vol. 19, pp. 389–393, 1977.

[66] K. Zhu and L. Pilon, "Transmittance of semitransparent windows with absorbing cap-shaped droplets condensed on their backside," *Journal of Quantitative Spectroscopy and Radiative Transfer*, vol. 201, pp. 53–63, 2017.

[67] E. W. Tow, "The antireflective potential of dropwise condensation," *Journal of the Optical Society of America A*, vol. 31, no. 3, 493, 2014.

[68] X. Huang, J. Mandal, and A. P. Raman, "Do-it-yourself radiative cooler as a radiative cooling standard and cooling component for device design," *Journal of Photonics for Energy*, vol. 12, 012112, 2021.

[69] J. G. Pieters, J. M. Deltour, and M. J. Debruyckere, “Light transmission through condensation on glass and polyethylene,” *Agricultural and Forest Meteorology*, vol. 85, pp. 51–62, 1997.

[70] F. Geoola and U. M. Peiper, “Outdoor testing of the condensation characteristics of plastic film covering materials using a model greenhouse,” *Journal of Agricultural Engineering Research*, vol. 57, pp. 167–172, 1994.

[71] M. T. Chaibi and T. Jilar, “Effects of a solar desalination module integrated in a greenhouse roof on light transmission and crop growth,” *Biosystems Engineering*, vol. 90, no. 3, pp. 319–330, 2005.

[72] K. Gotoh, Y. Nakata, M. Tagawa, and M. Tagawa, “Wettability of ultraviolet excimer-exposed PE, PI and PTFE films determined by the contact angle measurements,” *Colloids and Surfaces A: Physicochemical and Engineering Aspects*, vol. 224, pp. 165–173, 2003.

[73] P. Jankowski, D. Ogonczyk, A. Kosinski, W. Lisowski, and P. Garstecki, “Hydrophobic modification of polycarbonate for reproducible and stable formation of biocompatible microparticles,” *Lab on a Chip*, vol. 11, no. 4, pp. 748–752, 2011.

[74] S. Ebnesajjad and C. Ebnesajjad, *Surface Treatment of Materials for Adhesive Bonding*, 2nd Edition, Elsevier Science, 2014.

[75] W. Stober, A. Fink, and D. Ernst Bohn, “Controlled Growth of Monodisperse Silica Spheres in the Micron Size Range,” *Journal of Colloid and Interface Science*, vol. 26, pp. 62–69, 1968.

[76] K. Nozawa, H. Gailhanou, L. Raison, P. Panizza, H. Ushiki, E. Sellier, J. P. Delville, and M. H. Delville, “Smart control of monodisperse stöber silica particles: Effect of reactant addition rate on growth process,” *Langmuir*, vol. 21, no. 4, pp. 1516–1523, 2005.

[77] Matteo. Mannini, *Molecular Magnetic Materials on Solid Surfaces*. Firenze University Press, Firenze, Italy, 2008.

[78] J. Scheirs, Ed., *Modern Fluoropolymers High Performance Polymers for Diverse Applications*. John Wiley & Sons, New Jersey, NJ, 1997.

[79] G. Beadie, M. Brindza, R. A. Flynn, A. Rosenberg, and J. S. Shirk, "Refractive index measurements of poly(methyl methacrylate) (PMMA) from 0.4 – 16 μm," *Applied Optics*, vol. 54, no. 31, pp. 139–143, 2015.

[80] M. Rubin, "Optical properties of soda lime silica glasses," *Solar Energy Materials*, vol. 12, pp. 275–288, 1985.

[81] J. R. Howell, R. Siegel, and M. P. Mengüc, *Thermal Radiation Heat Transfer*, 5th edition, CRC Press, New York, NY, 2010.

[82] X. Zhang, J. Qiu, X. Li, J. Zhao, and L. Liu, "Complex refractive indices measurements of polymers in visible and near-infrared bands," *Applied Optics*, vol. 59, no. 8, 2337, 2020.

[83] M. K. Yang, "Optical properties of Teflon® AF amorphous fluoropolymers," *Journal of Micro/Nanolithography, MEMS, and MOEMS*, vol. 7, no. 3, 033010, 2008.

[84] J. H. Lowry, J. S. Mendlowitz, and N. S. Subramanian, "Optical characteristics of Teflon AF® fluoroplastic materials," *Optical Engineering*, vol. 31, no. 9, pp. 1982–1985, 1992.

[85] M. R. Vogt, H. Hahn, H. Holst, M. Winter, C. Schinke, M. Kontges, R. Brendel, and P. P. Altermatt, "Measurement of the optical constants of soda-lime glasses in dependence of iron content and modeling of iron-related power losses in crystalline Si solar cell modules," *IEEE Journal of Photovoltaics*, vol. 6, no. 1, pp. 111–118, 2016.

[86] R. A. Synowicki, B. D. Johs, and A. C. Martin, "Optical properties of soda-lime float glass from spectroscopic ellipsometry," *Thin Solid Films*, vol. 519, no. 9, pp. 2907–2913, 2011.

[87] Z. Liu, X. Zhang, T. Murakami, and A. Fujishima, “Sol-gel SiO_2/TiO_2 bilayer films with self-cleaning and antireflection properties,” *Solar Energy Materials and Solar Cells*, vol. 92, no. 11, pp. 1434–1438, 2008.

[88] L. Zhang, R. Dillert, D. Bahnemann, and M. Vormoor, “Photo-induced hydrophilicity and self-cleaning: Models and reality,” *Energy and Environmental Science*, vol. 5, no. 6. pp. 7491–7507, 2012.

[89] J. Deubener, G. Helsch, A. Moiseev, and H. Bornhöft, “Glasses for solar energy conversion systems,” *Journal of the European Ceramic Society*, vol. 29, no. 7, pp. 1203–1210, 2009.

[90] E. Simsek, K. Zhu, G. N. Kashanchi, M. J. Williams, T. Galy, M. Marszewski, S. H. Tolbert, and L. Pilon, “Light transfer through semi-transparent glass panes supporting pendant droplets,” *Journal of Quantitative Spectroscopy and Radiative Transfer*, vol. 261, 107493, 2021.

[91] J. Nocedal and S. J. Wright, *Numerical optimization*, Springer-Verlag, New York, NY, 2nd edition, 2006.

[92] X. Zhang, J. Qiu, J. Zhao, X. Li, and L. Liu, “Complex refractive indices measurements of polymers in infrared bands,” *Journal of Quantitative Spectroscopy and Radiative Transfer*, vol. 252, 107063, 2020.

[93] H. High-Technologies Corporation, “Measurement of optical characteristic of plastic by UH4150 spectrophotometer- An example of high throughput measurements" https://www.hitachi-hightech.com/products/images/12272/uh4150_data1_e.pdf (accessed April 15, 2021).

[94] S. I. Amma, S. H. Kim, and C. G. Pantano, “Analysis of water and hydroxyl species in soda lime glass surfaces using attenuated total reflection (ATR)-IR Spectroscopy,” *Journal of the American Ceramic Society*, vol. 99, no. 1, pp. 128–134, 2016.

[95] R. A. Alawajji, G. K. Kannarpady, Z. A. Nima, N. Kelly, F. Watanabe, and A. S. Biris, “High temperature, transparent, superhydrophobic Teflon AF-2400/Indium tin oxide nanocomposite thin films,” *Nanotechnology*, vol. 30, no. 17, 175702, 2019.

[96] G. Vox and E. Schettini, “Evaluation of the radiometric properties of starch-based biodegradable films for crop protection,” *Polymer Testing*, vol. 26, no. 5, pp. 639–651, 2007.

[97] C. Gueymard, “Simple Model of the Atmospheric Radiative Transfer of Sunshine (SMARTS). Version 2.9.5. 2005.” https://www.nrel.gov/grid/solar-resource/smarts.html (accessed Aug. 10, 2021).

[98] G. M. Hale and M. R. Querry, “Optical constants of water in the 200-nm to 200-μm wavelength region,” *Applied Optics*, vol. 12, no. 3, pp. 555–563, 1973.

[99] A. El-Sebaii and A. E. M. Khallaf, “Mathematical modeling and experimental validation for square pyramid solar still,” *Environmental Science and Pollution Research*, vol. 27, pp. 32283–32295, 2020.

[100] N. Choab, A. Allouhi, A. el Maakoul, T. Kousksou, S. Saadeddine, and A. Jamil, “Review on greenhouse microclimate and application: Design parameters, thermal modeling and simulation, climate controlling technologies,” *Solar Energy*, vol. 191, pp. 109–137, 2019.

[101] S. A. Kalogirou, *Solar Energy Engineering: Processes and Systems*, Academic Press, London, UK, 2nd edition, 2014.

[102] F. M. Zaihidee, S. Mekhilef, M. Seyedmahmoudian, and B. Horan, “Dust as an unalterable deteriorative factor affecting PV panel’s efficiency: Why and how,” *Renewable and Sustainable Energy Reviews*, vol. 65, pp. 1267–1278, 2016.

[103] H. A. Kazem and M. T. Chaichan, “Effect of environmental variables on photovoltaic performance-based on experimental studies,” *International Journal of Civil, Mechanical and Energy Science (IJCMES)*, vol. 2, no. 4, pp. 1–8, 2016.

[104] M. Santhakumari and N. Sagar, “A review of the environmental factors degrading the performance of silicon wafer-based photovoltaic modules: Failure detection methods and essential mitigation techniques,” *Renewable and Sustainable Energy Reviews*, vol. 110, pp. 83–100, 2019.

[105] N. S. M. Hussin, N. A. M. Amin, M. J. A. Safar, R. S. Zulkafli, M. S. A. Majid, M. A. Rojan, and I. Zaman, “Performance Factors of the Photovoltaic System: A Review,” in *MATEC Web of Conferences*, vol. 225, pp. 1–8, 2018.

[106] H. Jiang, L. Lu, and K. Sun, “Experimental investigation of the impact of airborne dust deposition on the performance of solar photovoltaic (PV) modules,” *Atmospheric Environment*, vol. 45, no. 25, pp. 4299–4304, 2011.

[107] A. Massi Pavan, A. Mellit, and D. de Pieri, “The effect of soiling on energy production for large-scale photovoltaic plants,” *Solar Energy*, vol. 85, no. 5, pp. 1128–1136, 2011.

[108] H. K. Elminir, A. E. Ghitas, R. H. Hamid, F. El-Hussainy, M. M. Beheary, and K. M. Abdel-Moneim, “Effect of dust on the transparent cover of solar collectors,” *Energy Conversion and Management*, vol. 47, no. 18–19, pp. 3192–3203, 2006.

[109] R. Appels, B. Lefevre, B. Herteleer, H. Goverde, A. Beerten, R. Paesen, K. D. Medts, J. Driesen, and J. Poortmans,"Effect of soiling on photovoltaic modules," *Solar Energy*, vol. 96, pp. 283–291, 2013.

[110] M. R. Maghami, H. Hizam, C. Gomes, M. A. Radzi, M. I. Rezadad, and S. Hajighorbani, "Power loss due to soiling on solar panel: A review," *Renewable and Sustainable Energy Reviews*, vol. 59, pp. 1307–1316, 2016.

[111] K. K. Ilse, B. W. Figgis, M. Werner, V. Naumann, C.Hagendorf, H. Pollmann, and J. Bagdahn, "Comprehensive analysis of soiling and cementation processes on PV modules in Qatar," *Solar Energy Materials and Solar Cells*, vol. 186, pp. 309–323, 2018.

[112] B. Figgis, A. Nouviaire, Y. Wubulikasimu, W. Javed, B. Guo, A. Ait-Mokhtar, R. Belarbi, S. Ahzi, Y. Remond, and A. Ennaoui, "Investigation of factors affecting condensation on soiled PV modules," *Solar Energy*, vol. 159, pp. 488–500, 2018.

[113] H. A. Kazem and M. T. Chaichan, "Effect of humidity on photovoltaic performance based on experimental study," *International Journal of Applied Engineering Research*, vol. 10, no. 23, pp. 43572–43577, 2015.

[114] M. A. Green, "Self-consistent optical parameters of intrinsic silicon at 300 K including temperature coefficients," *Solar Energy Materials and Solar Cells*, vol. 92, no. 11, pp. 1305–1310, 2008.

[115] D. Dahlioui, B. Laarabi, M. A. Sebbar, and A. Barhdadi, "Soiling effect on photovoltaic modules performance: New experimental results," in *International renewable and sustainable energy conference (IRSEC)*, Marrakech, Morocco, November 14-17, 2016.

[116] S. A. Sulaiman, A. K. Singh, M. M. M. Mokhtar, and M. A. Bou-Rabee, "Influence of dirt accumulation on performance of PV panels," *Energy Procedia*, vol. 50, pp. 50–56, 2014.

[117] H. Baig, H. Kanda, A. M. Asiri, M. K. Nazeeruddin, and T. Mallick, “Increasing efficiency of perovskite solar cells using low concentrating photovoltaic systems,” *Sustainable Energy and Fuels*, vol. 4, no. 2, pp. 528–537, 2020.

[118] P. Mialhe, S. Mouhamed, and A. Haydar, “The solar cell output power dependence on the angle of incident radiation,” *Renewable Energy*, vol. 1, no. 4, pp. 519–521, 1991.

[119] H. L. Willis and W. G. Scott, *Distributed Power Generation: Planning and Evaluation.* Marcel Dekker, New York, NY, 2000.

[120] W. Luo, Y. S. Sheng, P. Hacke, V. Naumann, D. Lausch, S. V. Harvey, J. P. Singh, J. Chai, Y. Wang, A. G. Aberle, and S. Ramakrishna, “Potential-induced degradation in photovoltaic modules: A critical review,” *Energy and Environmental Science*, vol. 10, no. 1, pp. 43–68, 2017.

[121] R. R. Cordero, A. Damiani, D. Laroze, S. MacDonell, J. Jorquera, E. Sepúlveda, S. Feron, P. Llanillo, F. Labbe, J. Carrasco, J. Ferrer, and G. Torres, “Effects of soiling on photovoltaic (PV) modules in the Atacama Desert,” *Scientific Reports*, vol. 8, no. 1, pp. 1–14, 2018.

[122] A. Sayyah, M. N. Horenstein, and M. K. Mazumder, “Energy yield loss caused by dust deposition on photovoltaic panels,” *Solar Energy*, vol. 107, pp. 576–604, 2014.

[123] B. Khalil, J. Adamowski, A. Shabbir, C. Jang, M. Rojas, K. Reilly, and B. Ozga-Zielinski, “A review: dew water collection from radiative passive collectors to recent developments of active collectors,” *Sustainable Water Resources Management*, vol. 2, no. 1, pp. 71–86, 2016.

[124] Cape Analytics, “Cape Analytics Data Report: The Most Solar Places in America.” https://capeanalytics.com/cape-analytics-data-report-the-most-solar-places-in-america/ (accessed October 28, 2020).

[125] Current Results Weather and Science Facts, “Most Humid Cities in the United States.” https://www.currentresults.com/Weather-Extremes/US/most-humid-cities.php (accessed October 28, 2020).

[126] C. Steven Sanchez and C.-L. Cheng, “Verification of optimal angle for south orientated tilted plans according to the latitude, concept for BIPV,” in *Proceedings of ISES Solar World Congress 2007*, D. Y. Goswami and Y. Zhao, Ed., Beijing, China, September 18–21, 2007.

[127] C. L. Cheng, C. S. Sanchez Jimenez, and M. C. Lee, “Research of BIPV optimal tilted angle, use of latitude concept for south orientated plans,” *Renewable Energy*, vol. 34, no. 6, pp. 1644–1650, 2009.

[128] R. Chenni, M. Makhlouf, T. Kerbache, and A. Bouzid, “A detailed modeling method for photovoltaic cells,” *Energy*, vol. 32, no. 9, pp. 1724–1730, 2007.

[129] European Comission, “Photovoltaic Geographical Information System (PVGIS),” https://ec.europa.eu/jrc/en/pvgis (accessed June 01, 2020).

[130] National Renewable Energy Laboratory, “Solar position and intensity (SOLPOS),” https://midcdmz.nrel.gov/solpos/solpos.html (accessed June 05, 2020).

[131] Energy Design Tools, “Climate Consultant, Energy Design Tools,” http://www.energy-design-tools.aud.ucla.edu/ (accessed June 26, 2020).

[132] G. C. Oehler, F. Lisco, F. Bukhari, S. Ulicna, B. Strauss, K. L. Barth, and J. M. Walls, "Testing the durability of anti-soiling coatings for solar cover glass by outdoor exposure in Denmark," *Energies*, vol. 13, no. 2, 299, 2020.

[133] M. Fathi, M. Abderrezek, and M. Friedrich, "Reducing dust effects on photovoltaic panels by hydrophobic coating," *Clean Technologies and Environmental Policy*, vol. 19, no. 2, pp. 577–585, 2017.

[134] Y. Y. Quan and L. Z. Zhang, "Experimental investigation of the anti-dust effect of transparent hydrophobic coatings applied for solar cell covering glass," *Solar Energy Materials and Solar Cells*, vol. 160, pp. 382–389, 2017.

[135] Y. Yuan, Y. Chen, W. L. Chen, and R. J. Hong, "Preparation, durability and thermostability of hydrophobic antireflective coatings for solar glass covers," *Solar Energy*, vol. 118, pp. 222–231, 2015.

[136] M. A. M. L. de Jesus, G. Timò, C. Agustín-Sáenz, I. Braceras, M. Cornelli, and A. de M. Ferreira, "Anti-soiling coatings for solar cell cover glass: Climate and surface properties influence," *Solar Energy Materials and Solar Cells*, vol. 185, pp. 517–523, 2018.

[137] K. Isbilir, F. Lisco, G. Womack, A. Abbas, and J. M. Walls, "Testing of an Anti-Soiling Coating for PV Module Cover Glass," in *IEEE 7th World Conference on Photovoltaic Energy Conversion*, pp. 3426–3431, Hawaii, June 10-15, 2018.

[138] S. Sutha, S. Suresh, B. Raj, and K. R. Ravi, "Transparent alumina based superhydrophobic self–cleaning coatings for solar cell cover glass applications," *Solar Energy Materials and Solar Cells*, vol. 165, pp. 128–137, 2017.

[139] S. Maharjan, K. Liao, A. J. Wang, K. Barton, A. Haldar, N. J. Alley, H. J. Byrne, and S. A. Curran, "Self-cleaning hydrophobic nanocoating on glass: A scalable manufacturing process," *Materials Chemistry and Physics*, vol. 239, 122000, 2020.

[140] A. Pan, H. Lu, and L. Z. Zhang, "Experimental investigation of dust deposition reduction on solar cell covering glass by different self-cleaning coatings," *Energy*, vol. 181, pp. 645–653, 2019.

[141] C. S. K. Achoundong, N. Bhuwania, S. K. Burgess, O. Karvan, J. R. Johnson, and W. J. Koros, "Silane modification of cellulose acetate dense films as materials for acid gas removal," *Macromolecules*, vol. 46, no. 14, pp. 5584–5594, 2013.

[142] M. M. Hossain and M. Gu, "Radiative cooling: Principles, progress, and potentials," *Advanced Science*, vol. 3, no. 7, 1500360, 2016.

[143] E. Simsek, M. J. Williams, J. Hoeniges, K. Zhu, and L. Pilon, "Infrared Radiation Transfer through Semitransparent Windows Supporting Absorbing Droplets," submitted to *Journal of Quantitative Spectroscopy and Radiative Transfer* (under review).

[144] A. D. Rakić, R. Rakić, A. B. Djuriš, J. M. Elazar, and M. L. Majewski, "Optical properties of metallic films for vertical-cavity optoelectronic devices," *Applied Optics*, vol. 37, no. 22, pp. 5271–5283, 1998.

[145] Y. Fu, J. Yang, Y. S. Su, W. Du, and Y. G. Ma, "Daytime passive radiative cooler using porous alumina," *Solar Energy Materials and Solar Cells*, vol. 191, pp. 50–54, 2019.

[146] J. Mandal, S. Mandal, J. Brewer, A. Ramachandran, and A. Pattabhi Raman, "Radiative Cooling and Thermoregulation in the Earth's Glow," Available: http://arxiv.org/abs/2006.11931 (Accessed: Nov. 18, 2021).

[147] E. Rephaeli, A. Raman, and S. Fan, “Ultrabroadband photonic structures to achieve high-performance daytime radiative cooling,” *Nano Letters*, vol. 13, no. 4, pp. 1457–1461. 2013.

[148] R. Sathyamurthy, S. A. El-Agouz, P. K. Nagarajan, J. Subramani, T. Arunkumar, D. Mageshbabu, B. Madhu, R, Bharathwaaj, N. Prakash, “A Review of integrating solar collectors to solar still,” *Renewable and Sustainable Energy Reviews*, vol. 77, pp. 1069–1097, 2017.

[149] “Gelest Inc.,” https://www.gelest.com/product/SIT8173.0/ (accessed Dec. 12, 2020).

[150] S. Bell, “Measurement Good Practice Guide - A Beginner’s Guide to Uncertainty of Measurement,” *Measurement*, vol. 20, no. 11, pp. 1–33, 1999, [Online]. Available: http://opensigle.inist.fr/handle/10068/697460.